Title

Computational Models of Modulated Gamma Oscillations and Activity-Dependent Graded Inhibition in the Olfactory Bulb

Author

Berry, Joseph Kendall

Publication Date

2023

Peer reviewed|Thesis/dissertation

Computational Models of Modulated Gamma Oscillations and Activity-Dependent Graded Inhibition in the Olfactory Bulb

By

J. KENDALL BERRY

DISSERTATION

Submitted in partial satisfaction of the requirements for the degree of

DOCTOR OF PHILOSOPHY

in

Physics

in the

OFFICE OF GRADUATE STUDIES

of the

UNIVERSITY OF CALIFORNIA

DAVIS

Approved:

Daniel L. Cox, Chair

Mark S. Goldman

Timothy J. Lewis

Committee in Charge

2023

Abstract of the Dissertation

Computational Models of Modulated Gamma Oscillations and Activity-Dependent Graded Inhibition in the Olfactory Bulb

by

J. Kendall Berry

Doctor of Philosophy

in

Physics

University of California, Davis

2023

Oscillations in olfactory bulb activity are modulated by neurodegenerative disease pathology. Particularly, Alzheimer's disease pathology has been found to strengthen the gamma-band oscillatory activity that arises from the interface between mitral and granule cells. Using two different computational models of the olfactory bulb network, this work investigates the effect of synaptic damage on olfactory bulb gamma oscillations and explores various mechanisms involved in gamma oscillation generation. The first model treats the olfactory bulb as a set of coupled nonlinear oscillators and propagates synaptic weight degradation locally and globally. Gamma oscillations are enhanced at moderate levels of dam-

age, followed by a loss of oscillatory activity predictable by linearized analysis. The second set of simulations uses the large-scale mechanistic model presented by Kersen, Tavoni, and Balasubramanian, implementing Izhikevich dynamical equations. This work adds synapse-specific graded inhibition to the mitral cells, resulting in activity-dependent inhibition critically involving granule cell NMDA current, similar to recent experimental findings. The modified model also implements tonic inhibition to the granule cell population, which reduces granule cell firing and increases mitral cell spike participation and network synchrony. The present iterations of this model do not yield robust gamma oscillations. However, the same model framework could feasibly achieve gamma activity via an entrainment mechanism by using resonant mitral cells with subthreshold oscillations. Finally, the last chapter proposes an extension of the model that implements inhibition-dependent backpropagation of mitral cell action potentials. Previous work theorized that such a mechanism could underlie the increased gamma power and decreased gamma frequency which is observed after modest application of GABA antagonist, an experimental result not yet captured by computational modeling. Thus this work aims to provide critical elements and potentially fruitful directions in the continued investigations of the generation and perturbation of olfactory bulb gamma oscillations.

Contents

List of Figures

List of Tables

Acknowledgements

I have been greatly blessed to be surrounded by many good people throughout my PhD. Enormous thanks goes to my wonderful advisor, Daniel; his sincere care for the goals and welfare of his students is so apparent. I am grateful to have had the opportunity to know and work with such a genuinely good person. It's been an honor, Daniel, thank you!

Mark Goldman and Tim Lewis, for their generous gifts of time, feedback, and good advice over the years. I am lucky to have such wonderful professors on my committee, thank you both!

Dina Zhabinskaya, Rajiv Singh, Angela Sharma, and Lenna Crabbe-Charlesworth, for helping me navigate TA assignments, funding, and other administrative items, especially as I began to face new health challenges. You helped make this feasible, thank you!

Mark and Cheryl Davey, my parents-in-law, for their support and for welcoming me into their home while I worked on my dissertation. Some of the most critical work was accomplished in the space they provided. You are amazing, thank you!

My parents, Brent and Laurlyn Berry, for more than I can write here. Your belief in me has been unshakeable, and it's been a source of strength my whole life. I love you!

My daughter, Ava, for being the best motivation for finishing my degree. You are a source of joy to us, and I love you!

Katie, my love, who has been a true partner through every challenge and joy since our

marriage. This dissertation exists largely because of your constant love and support. My Katie, I love you.

Jesus Christ, whose teachings and companionship give me peace and strength in good times and difficult. 2 Nephi 4:20; Psalm 23.

And finally, all my loved ones and friends; the numerous little ways they support and uplift me add up to an incredible sum. I am immensely blessed to know you all.

Chapter 1

Introduction

This work implements two different models of olfactory bulb oscillations with the goal of investigating modulations of oscillatory activity brought about by disease pathology. Computational models help us to better understand mechanisms behind neural activity, and when simulations and experimental studies inform each other, we get a fuller picture of how the brain functions[1]. Various neurological illnesses, including schizophrenia, clinical depression, Alzheimer's disease (AD), and Parkinson's disease (PD) have been simulated in various regions of the brain[2]. The olfactory bulb is a particularly intriguing area for this purpose due to its involvement in early stages of neurodegenerative diseases[3–5] and the measurable effects pathology has on animal models of disease-impacted olfactory bulb activity[6–9].

1.1 The Olfactory Bulb

The olfactory bulb (OB) is the first site for processing odor information before projecting it to other regions of the brain[10, 11]. Olfactory sensory neurons bind odorant molecules, sending their signals directly to bundles of dendrites called glomeruli in the most superficial layer of the olfactory bulb[12]. These dendrites belong to periglomerular cells, external

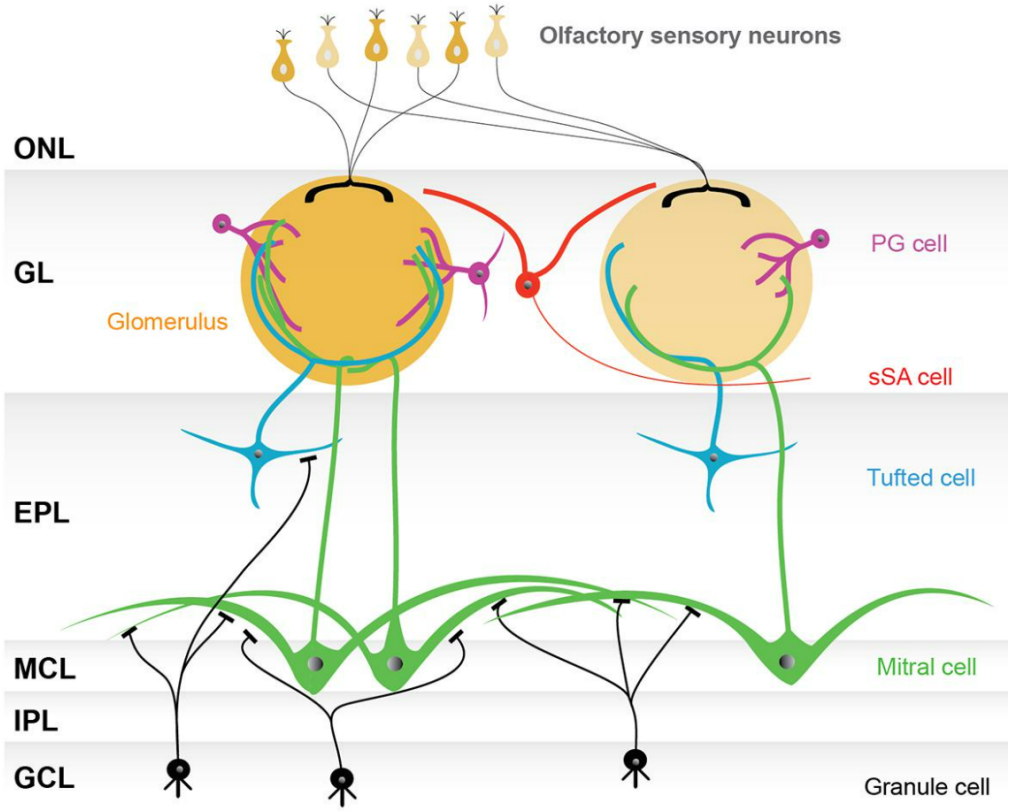

Figure 1.1: **Olfactory Bulb Layers and Neurons.** Figure reproduced from [10]. ONL: Olfactory nerve layer, GL: Glomerular layer, EPL: External plexiform layer, MCL: Mitral cell layer, IPL: Internal plexiform layer, GCL: Granule cell layer, PG: Periglomerular, sSA: Superficial short-axon. Short-axon cells appear in other layers as well, including in the EPL. External tufted cells are not pictured. Note that granule cells are axonless, so the contacts with mitral and tufted cells are dendrodendritic.

tufted cells, superficial short-axon cells, and the primary projection neurons of the OB, mitral cells (MCs) and tufted cells (TCs)[10] (see Fig. 1.1 from [10]). The MCs and TCs also have secondary dendrites that extend into the external plexiform layer (EPL) where they primarily make reciprocal dendrodendritic synapses with granule cell dendrites[13, 14], although they also may interact in lesser-understood ways with EPL short-axon cells[15] (similar morphologically to short-axon cells in the glomerular layer in Fig. 1.1, but in the EPL). The work here focuses on the interactions between the most prevalent OB neurons,

MCs and granule cells (GCs), although recent studies suggest the importance of tufted cells to OB oscillations[16].

The dendrodendritic contacts between MCs and GCs rely on AMPA and NMDA receptors in GCs and GABA receptors in MCs[10]. GABA receptors bind the molecule that gives the channel its name, gamma-aminobutyric acid (GABA), and precipitate inhibitory current by the influx of chlorine ions[17]. Both AMPA and NMDA receptors are excitatory channels that are activated by glutamate[13], but AMPA channels are faster acting[18]. NMDA channels have slower dynamics for opening and closing, in part due to a more complicated activation process[19]. The binding of glutamate is not sufficient alone to open NMDA channels; the membrane potential of the post-synaptic neuron also needs to be sufficiently high in order to remove a magnesium block. This two-part mechanism is believed to play an important role in GC-driven inhibition of MCs[20]. In summary, when a MC spikes, the action potential backpropagates down the lateral dendrites, releasing glutamate and activating AMPA and NMDA receptors on GC dendrites[21, 22] (see Fig. 1.2). Excited GCs release GABA-mediated inhibition back onto MC secondary dendrites in a graded manner, even in the absence of somatic GC spikes[13, 14, 21, 22].

The reciprocal synapses between GCs and MCs are widely believed to be the source of gamma-band (35 - 80 Hz) oscillatory activity in the OB[14, 23, 24] (but see also [15]). Gamma oscillations are associated with odor discrimination[25], some learning tasks[25], and exploration[26, 27], and recent evidence suggests that gamma oscillations also carry odor identity information[28]. MC-GC interactions are also probably behind the lesser-understood OB beta oscillations[29] (15 - 30 Hz), which also play a role in learning[30, 31], as well as odor sensitization[32]. The last type of oscillatory activity in the olfactory bulb, the theta-band (2 - 12 Hz), is driven by respiration[26] and coordinates activity within the OB[33], likely helping to synchronize MC activity for the generation of gamma and beta

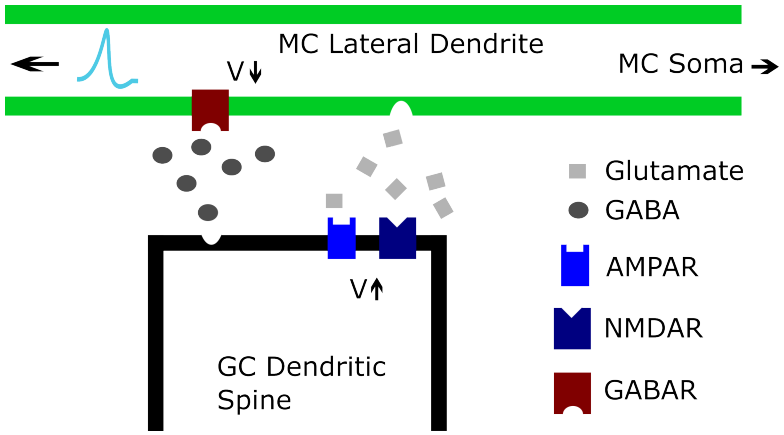

Figure 1.2: **Dendrodendritic Synapse Between Mitral and Granule Cells.** As the action potential backpropagates along the MC lateral dendrite, it triggers the release of glutamate which activates AMPA and NMDA receptors (AMPARs and NMDARs, respectively) on the GC dendritic spine, exciting the GC. GC dendritic spines release GABA in a graded manner (independent of GC spiking), binding to GABA receptors (GABARs) on the MC lateral dendrite and inhibiting the MC.

oscillations[24].

The work presented here focuses on gamma oscillations due to indications that AD pathology modulates the gamma band in particular[6, 7]. Disease pathology is present in the OB in early stages of AD[34–40], making OB oscillatory activity a potential early biomarker for AD, as it has already been shown to be for PD[41]. The change in OB gamma oscillatory activity found in mouse models of AD[6, 7] bore a striking resemblance to results from Lepousez and Lledo, where application of GABA antagonist led to increased gamma power and decreased gamma frequency[27]. The mechanism behind these modifications of the OB gamma rhythm are yet to be understood.

1.2 Computational Models of the Olfactory Bulb

Computational work explores a wide variety of olfactory bulb function[42]. Odor information processing and representation is a large area of study, with focuses including glomerular layer computations[43], information streams using biophysical models[44], connectivity and decorrelation of activity patterns[45], learning and odor discrimination[46], and analytical approaches to odor encoding[47]. One group recently developed a neuromorphic network based on the olfactory bulb to implement odor learning and identification with input from chemosensors[48, 49].

Oscillations in the OB network are another big focus for modeling efforts, and the one most relevant to the work here. Models of OB oscillatory activity rely primarily on two general mechanisms of neural oscillation generation. In the pyramidal interneuron gamma (PING) theory, periodic inhibition gates firing of the excitatory (or pyramidal) neurons[50]. In the case of the olfactory bulb, inhibition from GCs would establish the windows of allowed MC firing[51]. The other class of theory is entrainment, with naturally rhythmic MC firing (often established by subthreshold oscillations[52]) synchronized by weak correlated inhibition[53]. Some models have used ideas from both theories, for example using sub-threshold oscillations to help synchronize MC firing but still relying on a PING-like mechanism to set the network frequency[54]. One model generates gamma oscillations by an entrainment mechanism and beta by a PING mechanism[55], while another uses PING for both[51]. Each of these models has helped extend our understanding of oscillatory activity in the OB and in the brain generally.

1.3 Preview of the Thesis

Here, I work with two different models of OB oscillations. The simplicity of the first model (based on [56]) allows a semi-analytical approach to investigating the effects of propagating synaptic damage on oscillatory activity (Chapter 2). The second model (based on [45]) is more mechanistically and biophysically grounded and thus enables the implementation of key features of OB oscillations, especially synapse-specific graded inhibition (Chapter 3).

Based on indications that AD and PD pathologies weaken synaptic connections[57–59], Chapter 2 takes a semi-analytical approach to investigating the effect of synaptic weight on oscillatory activity in a simplified rate-based model of the olfactory bulb based on [56]. Results show increased gamma power with moderately reduced weight between model MC and GC units. This increased power is due to the nonlinear transformation of the increased internal MC state to its output state in this model. When connection weight is further decreased, there is a Hopf bifurcation, and sustained oscillatory activity disappears.

In Chapter 3, using a large-scale mechanistic model from [45], I incorporate features of OB function thought to be important to gamma oscillation generation. Namely, tonic inhibition is implemented to reduce GC excitability and firing, and graded inhibition based on synapse-specific GC NMDA current is delivered to the MCs[14, 55, 60, 61]. The graded method yields MC activity-dependent inhibition, similar to experimental findings[20, 62]. Suggestions for achieving robust gamma oscillations with these features are discussed, with emphasis on incorporating resonance into the MC model[53] to achieve network entrainment[52, 55]. Further ideas are presented in Chapter 4 for reproducing Lepousez and Lledo's result of stronger gamma power and decreased gamma frequency in the presence of GABA antagonist[27] by implementing a simplified form of inhibition-dependent propagation of action potentials along MC lateral dendrites[63]. Realistically modeling the modulation of OB oscillations

will lead to greater understanding of not only the mechanisms behind oscillatory activity generation, but also of how disease pathology affects neural circuitry.

Chapter 2

Increased oscillatory power in a computational model of the olfactory bulb due to synaptic degeneration

This chapter appears as an article published in Physics Review E *in collaboration with Daniel Cox*[64].

2.1 Introduction

The olfactory system, and in particular the olfactory bulb (OB), is implicated in early stages of a number of neurodegenerative diseases, including two of the most prevalent, Alzheimer's disease (AD) and Parkinson's disease (PD)[3–5]. In both AD and PD, olfactory deficits occur years before diagnosis and often before other symptoms[5, 37, 65–69]. Furthermore, the OB is a site of early pathology in both diseases[34–40], with resulting aberrant neural activity[6–9, 70, 71]. We hope that computationally modeling olfactory bulb activity in disease-like conditions can help to further shed light on mechanisms of dysfunction, identify markers

of disease, and bring attention to the opportunity the OB presents for earlier diagnosis of neurodegenerative illnesses.

The OB is the first processing area for incoming odor information[72], but exactly how it is represented is an ongoing question for which there are various theories, mainly revolving around combinatorics of principal neuron activity[47, 73–75]. Oscillations in neural activity in the bulb may also play a part in encoding odor identity, and are likely important to odor recognition or information transfer, or both[26]. Neural networks can exhibit a variety of dynamical behaviors[76]; the push-pull nature of the excitatory-inhibitory interactions of the OB make it an interesting example of a nonlinear oscillator[77]. In addition, studying the robustness of the system's oscillations has relevance to the neurodegenerative diseases mentioned above.

The oscillatory behavior of the OB in the gamma range (40-80 Hz) is driven by reciprocal synaptic interactions between the dendrites of excitatory mitral cells and inhibitory granule cells[12, 26] (also called dendrodendritic synapses[21]). That is, mitral cells excite granule cells which in turn inhibit the mitral cells, leading to gamma band oscillatory activity. Other frequencies of oscillations are present in the bulb as well, namely theta (2-12 Hz) and beta (15-30 Hz). The precise manner in which PD or AD impacts these oscillations and other OB functions is still a matter of investigation[4, 5], although studies have found perturbations in this oscillatory activity in animal OBs in the presence of both PD-like pathology[9, 78] and AD-like pathology[6–8, 71, 79].

More generally, the effects of PD and AD pathology on neurons is a very active area of study, with various alterations of neuron function resulting from overexpression or injection of pathological protein (see [80, 81] for reviews of PD pathology, see [82–84] for reviews of AD pathology). Synaptic dysfunction is one effect for which there is evidence in both AD[57, 85] and PD[58, 86–88], with studies finding (for example) decreased spine density[7, 70, 89],

decreased synaptic proteins[7, 8], reduced vesicle release[90], increased synaptic junction distance[8], and decreased synaptic transmission[91].

Computational studies of the effects of AD on neural networks have focused largely on the hippocampus and cortical areas, especially effects on memory formation and storage (see [92] for review). In PD, most computational models simulate various effects of dopamine loss in the basal ganglia network, exploring changes in network output and oscillatory activity, as well as effects of deep brain stimulation therapy (see [93, 94] for reviews). Importantly, we are not aware of any works that examine the impact of neurodegenerative damage on a computational model of the olfactory bulb.

Many excellent and insightful computational models of the OB exist[42], focusing on various aspects of the olfactory system, such as generating oscillatory behavior[54, 56, 95], glomerular layer computations[43], and odor computations and representation[47, 96].

In the present study, we implemented the Li-Hopfield model[56], a rate based model with units representing small populations of neurons. The model replicates gamma band oscillatory activity found in the OB (see [56] compared to electroencephalogram (EEG) studies[97] and micro-electrode recordings of extra-cellular potential, also called local field potentials[27]). The oscillations are produced solely via interaction between model mitral cell (MC) units and granule cell (GC) units, as supported by findings that dendrodendritic interactions between MCs and GCs alone were sufficient for gamma band oscillatory activity[14, 27]. While the model excludes certain aspects of the OB network (such as beta oscillations[29]), it captures some key behaviors, and its simplicity enables semi-analytical and numerical treatments that are not accessible in more complex models.

The original Li-Hopfield work only implemented a 1D connection architecture; here, we expand the model to various sizes and 2D connection structures. We found that the 1D and 2D networks operate similarly, but in different regimes. Importantly, on the scale of

the original Li-Hopfield model, we found that for some types of damage, 2D networks show a significant enhancement of gamma oscillatory power at moderate levels of damage to the connections between MCs and GCs. Analysis of the model network's behavior shows that this results from an increased excitability of the MC population due to a reduction of inhibition, with the nonlinearity of the activation function being essential. The balance of excitation and inhibition is important for robustness of oscillatory activity. As a result, we would expect to see an increase in oscillatory power at moderate levels of damage to the reciprocal connections between excitatory and inhibitory cells in these types of oscillatory networks.

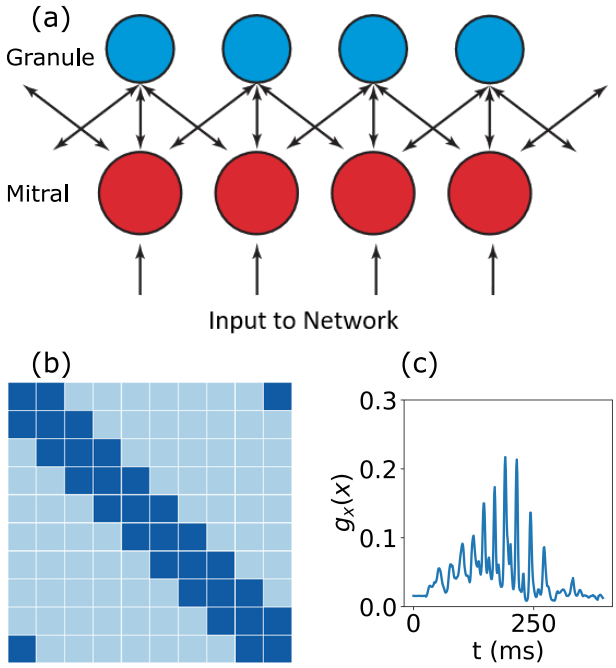

Figure 2.1: **Li-Hopfield Model.** (a) Mitral cell units receive odor input and excite the granule cell units, which in turn inhibit the mitral cell layer. The connections between mitral and granule cell units define a 1D ring structure. The networks implemented here have 20 units (mitral plus granule), 40 units, and 100 units. (b) Example weight matrix defining a 1D periodic network. Light blue entries are zero (no connection), dark blue signifies positive non-zero entries (established connection). (c) Example of mitral cell output ($g_x(x_i)$) over the course of a single inhale-exhale cycle. The inhalation peaks at 205 ms, at which point the exhale begins. Parameters for the model are found in Table 2.1. Each mitral or granule cell unit should be considered as representing a particular population of mitral cells.

For the remainder of this paper, we first detail the governing equations of the Li-Hopfield model and describe how the model is modified for larger sizes and 2D connection structure. We then lay out the method of delivering damage to the network and explain how oscillatory activity in the network is characterized. The resulting increase in oscillatory activity and underlying mechanisms are explored, with observations about the differences between 1D and 2D networks. Finally, we discuss the relevance to experimental studies, the limitations, and the future directions of the work presented here.

2.2 Methods

Li-Hopfield Model

The Li-Hopfield model describes the internal state (representative of membrane potential) and output state (or cell activity, representative of firing rate) of mitral and granule cells over an inhale-exhale cycle. Each MC and GC model unit represents a subset or small population of MCs or GCs, with the weight matrices H_0 and W_0 representing the dendrodendritic synaptic connections between MCs and GCs. For simplicity, MC-MC and GC-GC interactions are not considered here since synaptic interactions in the region giving rise to gamma oscillations are predominantly reciprocal MC-GC synapses[12, 14, 27].

The model is governed by the following set of equations,

$$\dot{\mathbf{x}} = -H_0\ \mathbf{g_y}(\mathbf{y}) + \mathbf{I_b} + \mathbf{I}_{\text{odor}}(t) - \alpha\mathbf{x}, \tag{2.1}$$

$$\dot{\mathbf{y}} = W_0\ \mathbf{g_x}(\mathbf{x}) + \mathbf{I_c} - \alpha\mathbf{y}, \tag{2.2}$$

where $\mathbf{x}$ and $\mathbf{y}$ are vectors containing the internal state of each MC unit and each GC

Table 2.1: The parameters for the model are as given by Li and Hopfield[56, 98]. The model is evaluated at time steps representing 1 ms and runs for 395 ms. Thus all times t below are in ms.

Parameter	Value
$I_{b,i}$	0.243
$I_{c,i}$	0.1
α	0.15
$g_y(y_i)$	$\begin{cases} 2.86 + 2.86\tanh(\frac{y_i-1}{2.86}) & \text{if } y_i < 1 \\ 2.86 + .286\tanh(\frac{y_i-1}{.286}) & \text{if } y_i \geq 1 \end{cases}$
$g_x(x_i)$	$\begin{cases} 1.43 + 1.43\tanh(\frac{x_i-1}{1.43}) & \text{if } x_i < 1 \\ 1.43 + .143\tanh(\frac{x_i-1}{.143}) & \text{if } x_i \geq 1 \end{cases}$
$I_{\text{odor},i}$	$\begin{cases} 0 & \text{if } t < 25 \\ 0.00429(t-25) & \text{if } 25 \leq t < 205 \\ 0.00429(t-25)e^{-0.03(t-205)} & \text{if } t \geq 205 \end{cases}$

unit, respectively. The functions $\mathbf{g_x}(\mathbf{x})$ and $\mathbf{g_y}(\mathbf{y})$ are sigmoidal activation functions[56] that translate internal state into output state, $\mathbf{I_b}$ is tonic uniform background excitatory input to the mitral cells, $\mathbf{I_c}$ is tonic uniform excitatory centrifugal input to the granule cells, and α is the decay constant, which is taken to be the same for mitral and granule cells in this model. Random noise is added to $\mathbf{I_b}$ and $\mathbf{I_c}$ in the form given in the original Li and Hopfield paper[56]. $\mathbf{I}_{\text{odor}}$ is excitation from the odor input, which rises linearly with inhale and falls exponentially with exhale. In principle, $\mathbf{I}_{\text{odor}}$ could have different levels of input for each mitral cell. In the simulations here, we define it to be uniform for simplicity and because damage should affect all odors. The exact functions and values for the parameters can be found in Table 2.1, and are as given in [56, 98]. H_0 and W_0 are the matrices that define the connections from granule to mitral cells (inhibitory, as indicated by the negative sign) and from mitral cells to granule cells (excitatory), respectively.

The weight matrices H_0 and W_0 dictate the connective structure of the network. The

original Li-Hopfield model contained 10 MC units and 10 GC units, connected in mitral-granule pairs, with each pair connecting to neighboring pairs on a 1D ring (Fig. 2.1(a)(b)). For the work here, the network was adapted to include larger numbers of MCs and GCs. This was accomplished by initializing a matrix of the desired size with entries of the same order magnitude as the original connection matrices, and then updating the non-zero entries randomly until the desired behavior was achieved. Because the interface between the dendrites of the MCs and GCs, the external plexiform layer, lies on the surface of an ellipsoid, matrices were constructed with 2D architecture for each size in the same way (Fig. 2.2). Therefore, the model was implemented in six different architectures: 20 cells (mitral plus granule), 40 cells, and 100 cells in 1D and 2D. It should be noted that W_0 in the original Li-Hopfield model included extra connections that make the architecture not truly 1D. These connections have been retained for the 1D 20 cell network, but are not present in any of the other 1D network structures. The specific matrices for each size can be found on the Github repository (see Code Accessibility).

Damage

In our work here, we focus on damage delivered to the weight matrices H_0 and W_0 (although damaging other network components was also explored, see Appendix A). This was partly informed by the numerous studies that point to synaptic dysfunction as one salient effect of neurodegenerative pathology[7, 8, 58, 86–88, 90]. Additionally, this aligns with the scope of the Li-Hopfield model, which focuses on the gamma oscillations that arise from the excitatory-inhibitory interactions between MCs and GCs.

We measure damage to the network by δ, the fraction of weight removed. In the case of

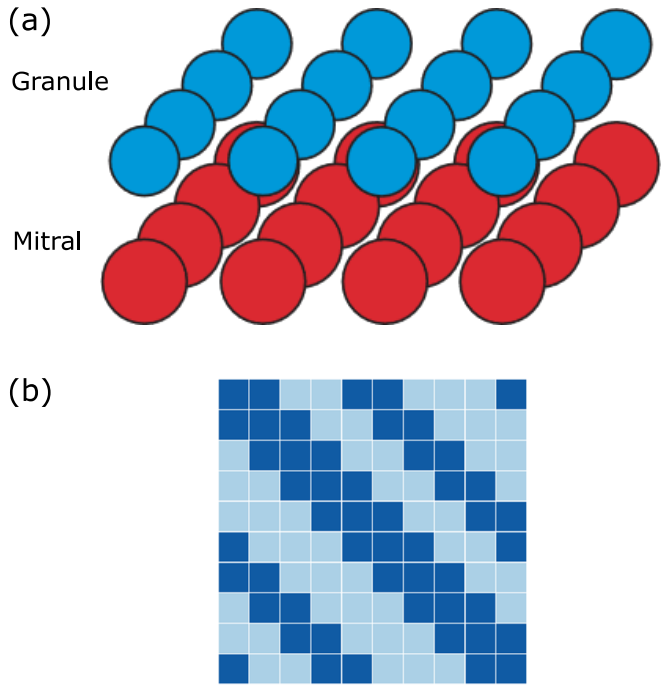

Figure 2.2: **2D Model.** (a) The connections between mitral and granule cell units are largely the same as in 1D, but extend in two directions. (b) Example of a weight matrix structure defining a 2D periodic network structure. Light blue entries are zero (no synaptic connection), dark blue signifies positive non-zero entries (established synaptic connection). Each MC unit connects to its GC pair, as well as four other GC units. GCs connect to MC units following the same pattern.

W_0 for example,

$$\delta = 1 - \frac{\sum_{ij} W_{\text{Damaged},ij}}{\sum_{ij} W_{0,ij}}, \tag{2.3}$$

where W_0 is the undamaged matrix and W_{Damaged} is the damaged matrix.

In a given trial, damage is delivered to either H_0 (the synaptic connections from granule to mitral cells), or to W_0 (the synaptic connection from mitral to granule cells). The damage to the selected part of the network is increased, the network runs at that damage level, and the activity is recorded. The damage is propagated in one of three ways: Flat Damage (FD), Columnar Damage (CD), or Seeded Damage (SD).

For FD, the damage is delivered to every element of the selected matrix equally. This

amounts to simply scaling the chosen quantity uniformly. For example, if FD was applied to H_0, each element of H_0 would be reduced by the same fraction of its original value on each damage step. This continues until the matrix is reduced to zero (see Fig. 2.3(a)). FD thus represents a global progression of pathology.

For CD, the damage is delivered to a specific matrix column (representing synaptic transmission from a particular unit), ramped up until that element is reduced to zero, and then that procedure is repeated successively on adjacent elements until the maximum damage level is reached (see Fig. 2.3(b)). For example, if CD was delivered to H_0, damage would be delivered incrementally to a single column until it was reduced to zero. The same process would then begin on the column to the right, and this process is continued until half of the columns are removed (Fig. 2.3 (b)). This is representative of a very local pathological spread.

SD is a hybrid of FD and CD. Damage is first delivered to a single column, and on the next damage step, damage is delivered to that column again, as well as to neighboring elements. For example, if SD was enacted on H_0 in a 1D network, it would begin on one column, say column 6. On the subsequent damage step, the damage would then be delivered to columns 5, 6, and 7. This spreading continues with each damage level until the matrix is reduced to zero (Fig. 2.3(c)). SD thus represents a pathology that begins locally but becomes more global as damage spreads.

Characterizing Network Oscillatory Activity

The average oscillatory power, P_{avg}, is calculated by first high-pass filtering the mitral cell activity above 15 Hz to ignore theta band (2-12 Hz) activity, which was beyond the scope of the present study. Next, the power spectrum ($\mathbf{P}(f)$) is calculated for each mitral cell from

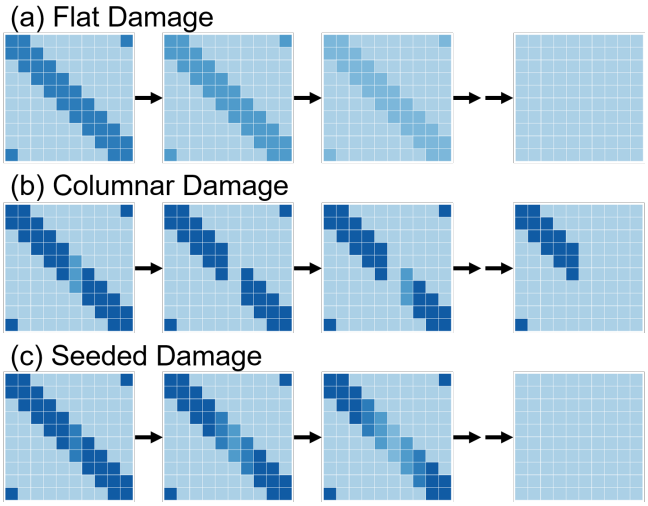

Figure 2.3: **Schematic of Damage Propagation Strategies.** (a) Example of FD delivered to H_0 or W_0 in the 1D 20 unit network. (b) Example of CD delivered to H_0 or W_0 in the 1D 20 unit network. Damage begins in a single column (in this case, column 6). For CD, only up to half the matrix weight is removed because in most cases, the network activity was already greatly disrupted by that point. (c) Example of seeded damage delivered to H_0 or W_0 in the 1D 20 unit network. Damage begins in a single column (in this case, column 6).

125 ms to 250 ms using Scipy's periodogram function[99]. This time window captures the oscillatory behavior during the most active part of the cycle (see Fig. 2.1(c)) while ignoring the spurious signals that can arise at higher levels of damage that are not actually due to gamma band oscillatory activity (see Fig. A.8 in Appendix A, also in [100]). The power spectrum is then integrated over all frequencies, f, for each cell (see Figures A.5, A.6, A.8, and A.9 in Appendix A[100] for example power spectra) and averaged over the mitral cell population (N) to get P_{avg},

$$P_{\text{avg}} = \frac{1}{N}\sum_{i=1}^{N}\int_{0}^{\infty} P_i(f)df. \tag{2.4}$$

Each quantity is averaged over five trials with differently seeded noise. For CD and SD, the trial is then repeated using each cell as the starting point and the values are averaged again over all starting cells.

Code Accessibility

The simulations are run in Python using Scipy's solve_ivp function[99] on Ubuntu 18.04, and all code/software described in the paper is freely available online at `https://github.com/jkberry07/OB_PD_Model`.

2.3 Results

Damage to W_0 and H_0

The effect of damage on average oscillatory power depends on the damage scheme. FD and SD to H_0 or W_0 in 2D networks results in increases in P_{avg} at intermediate levels of damage (Fig. 2.4(a)), but CD rarely shows an increase in P_{avg} (Fig. A.2 in Appendix A). Thus, an increase of oscillatory power requires global progression of damage to some degree. While this rise in P_{avg} is ubiquitous among 2D networks with FD and SD, P_{avg} decreases monotonically for most 1D cases (see Fig. 2.4(b)). For the work shown here, damage was only delivered to either H_0 or W_0, but delivering damage to both has a similar effect of increased oscillations at intermediate levels of damage (see Fig. A.4 in Appendix A) and relies on the same principles presented hereafter.

The increase in oscillatory power in 2D networks results from larger MC activity amplitude (as opposed to, say, recruitment of previously inactive units). Fig. 2.5 shows an example cell from the 2D 100 cell network at no damage and at the level of flat damage corresponding to the maximum P_{avg}. The increase in amplitude shown is seen for all active cells in 2D networks receiving FD. Similar effects are seen for SD, though the following treatment will be done for FD for simplicity.

The question is then why does the output state amplitude increase? To understand this,

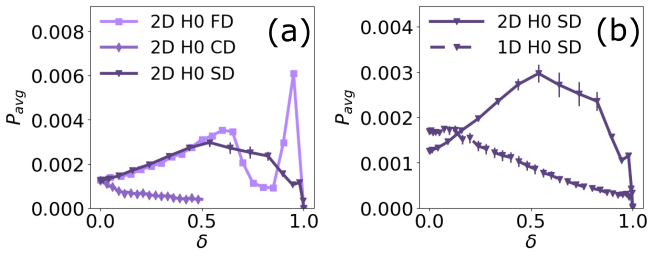

Figure 2.4: **Effect on Oscillatory Power.** (a) Average oscillatory power (P_{avg}) for FD, CD, and SD delivered to H_0 in the 2D 100 cell network plotted against damage as a fraction of total synaptic weight removed (damage level, δ). (b) P_{avg} for SD delivered to H_0 in the 1D and 2D 100 cell networks. FD and SD to H_0 or W_0 result in a rise in P_{avg} for the 2D network, while CD to the 2D network and any kind of damage to the 1D network do not in general (see Figures A.1 through A.3 in Appendix A for P_{avg} for each network and damage type). The sharp peak in P_{avg} for FD to H_0 at $\delta = 0.95$ is due to a sharp rise and drop in MC unit output states rather than to oscillatory activity, as illustrated by Fig. A.6 in Appendix A. Example cell activity at various δ and associated power spectra can be found in Figures A.8 and A.9 (also in [100]).

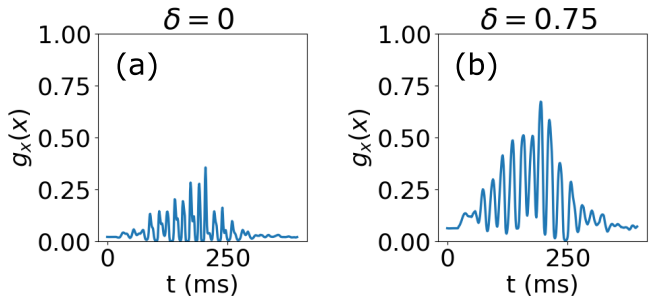

Figure 2.5: **Cell Activity Compared at Different Damage Levels.** (a) Output state of mitral cell number 35 in the 2D 100 cell network with no damage. (b) Output state of mitral cell number 35 in the 2D 100 cell network with FD to W_0 at damage level 0.75 ($W_{\text{Damaged}} = 0.25W_0$). This was the damage level at which average oscillatory power was maximized.

we look at the internal state $\mathbf{x}$ of the MC units. The increase in output state amplitude is not due to increased amplitude of internal state oscillations. Rather, it is because of increased average internal state. As a simple measure of internal state amplitude, we inspect the largest peak and the lowest trough between 180 ms and 220 ms (the time window over which when output state oscillations are the greatest) for active units (defined as units that had

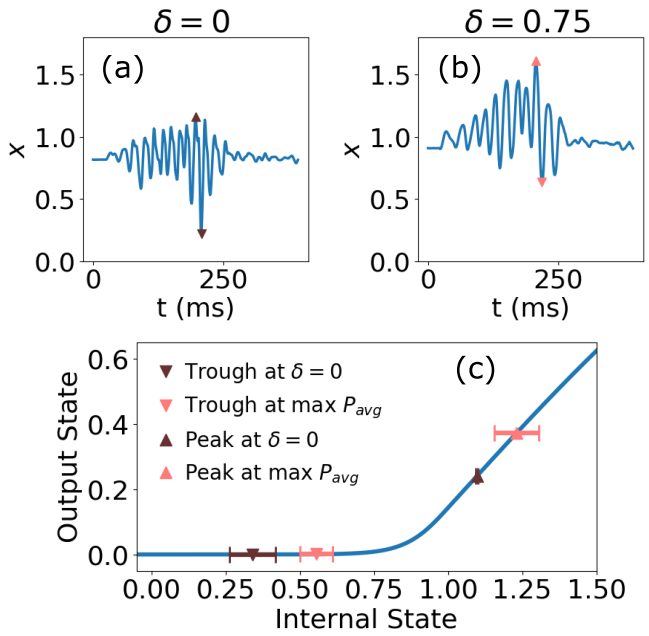

Figure 2.6: **Increase in Average Internal State Results in Increased Amplitude in Output State.** (a) Internal state of mitral cell number 35 in the 2D 100 cell network with no damage. (b) Internal state of mitral cell number 35 in the 2D 100 cell network with FD to W_0 at damage level 0.75 ($W_{\text{Damaged}} = 0.25W_0$). This was the damage level at which average oscillatory power was maximized for FD to W_0. (c) Activation function $g_x(x)$, with dark brown marking the average minimum trough and average maximum peak for 2D networks at $\delta = 0$, and light pink marking the same but at the damage level corresponding to the maximum P_{avg}.

an individual oscillatory power greater than 0.001). When the null damage case is compared to the damage level at which P_{avg} is maximized, the distance from peak to trough is similar (0.7562 ± 0.0808 for $\delta = 0$ and 0.6765 ± 0.1300 for δ at which P_{avg} is maximized). The difference is in the increase in the average internal state and how that translates into output state. Though both the minimum trough and the maximum peak increase, only the increase in maximum peak has an effect on the output state because the trough still lies below the threshold of the activation function (see Fig. 2.6). This illustrates that the nonlinearity is essential for the increase in P_{avg} to manifest.

The average internal state increase results from damaging W_0 or H_0, which lowers the overall inhibition to the MC layer, either directly (in the case of H_0) or by reducing excitation to the GC layer (in the case of W_0). The dependence on H_0 and W_0 is explored further in a simplified semi-analytic approach in the supplement[100].

In the Li-Hopfield work, to gain understanding of the full numerical solution, an adiabatic approximation is made in which the oscillations are modeled as variations around a fixed point. This linearized analysis can explain the drop in P_{avg} that follows the rise. Here, we summarize the analysis done by Li-Hopfield; for a more detailed treatment, see the original work[56]. Keeping the full network, we treat $\mathbf{x}$ and $\mathbf{y}$ as deviations from the fixed points, and the governing equations become:

$$\dot{\mathbf{x}} = -H_0 G'_y(\mathbf{y_0})\mathbf{y} - \alpha\mathbf{x}, \tag{2.5}$$

$$\dot{\mathbf{y}} = W_0 G'_x(\mathbf{x_0})\mathbf{x} - \alpha\mathbf{y}, \tag{2.6}$$

where $G'_y(\mathbf{y_0})$ and $G'_x(\mathbf{x_0})$ are diagonal matrices resulting from the linearized approximation of $g_y(y)$ and $g_x(x)$. Further manipulation yields:

$$\ddot{\mathbf{x}} + 2\alpha\dot{\mathbf{x}} + (A + \alpha^2)\mathbf{x} = 0, \tag{2.7}$$

where

$$A = H_0 G'_y(\mathbf{y_0}) W_0 G'_x(\mathbf{x_0}). \tag{2.8}$$

The analytical solution is $\mathbf{x} = \mathbf{x}_k \exp -(\alpha \pm i\sqrt{\lambda_k})t$, where $\mathbf{x}_k$ is the k^{th} eigenvector of A and λ_k is the k^{th} eigenvalue. The eigenvalues of A predict the presence of oscillatory behavior. If

$$Re[i\sqrt{\lambda_k}] > \alpha \tag{2.9}$$

is satisfied, oscillations are present, with the eigenvalue that results in the value highest above α dominating[56]. If no eigenvalue satisfies the condition, oscillations die away quickly.

As W_0 or H_0 decrease with damage, the eigenvalues of the matrix A also decrease. Once the dominant eigenvalue falls below the threshold set by the decay rate, the network behaves like a damped oscillator and P_{avg} drops dramatically. Though this is derived from an approximation, it faithfully predicts the sudden reduction in P_{avg} (see Fig. 2.7).

This can also be demonstrated with a phase diagram, plotting a MC unit internal state against a GC unit internal state (similar to [77, 101]). To illustrate the network's behavior in this way, the odor input was modeled as constant in time. Just before the eigenvalue falls below the threshold, the network activity follows a limit cycle (see Fig. 2.7(c)). However, once it drops below threshold, a bifurcation occurs and network activity approaches a fixed point (see Fig. 2.7(d)).

1D Networks

Network connection matrices of all types were constructed to give roughly equivalent starting oscillatory powers with the same average synaptic weights values. Because the 2D networks were of necessity less sparse than the 1D networks, this meant that the total synaptic weight in the 2D networks was greater than for the 1D networks. Under these conditions, we observe the increase in oscillatory power in FD trials only in 2D networks (for example, Fig. 2.4). However, if the null-damage matrices in 1D networks instead have a similar total weight rather than the same average weight, the behavior is largely the same, just on a smaller scale.

As an example, we deliver FD to W_0 in a 1D network, but begin with W_0 thrice its typical value. With more weight in the network, the initial average internal state is reduced,

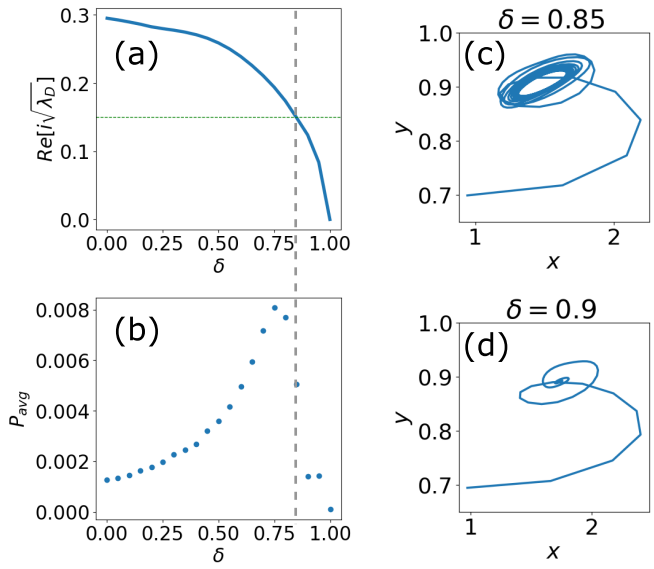

Figure 2.7: (a) The real part of the square root of the dominant eigenvalue ($Re[i\sqrt{\lambda_D}]$) plotted against damage for the 2D 100 cell network with FD to W_0. According to the linearized analysis, when $Re[i\sqrt{\lambda_D}]$ falls below the decay rate, marked as a horizontal dotted green line, oscillations are dampened. (b) Average oscillatory power (P_{avg}) plotted against damage for the 2D 100 cell network with FD to W_0. The steep drop off in P_{avg} corresponds to the damage level at which $Re[i\sqrt{\lambda_D}]$ falls below the decay rate, as illustrated by the vertical dashed line. (c) Phase plot, with mitral cell internal state (x, mitral cell number 35) on the x-axis, and granule cell internal state (y, granule cell number 35) plotted on the y axis, at the damage level immediately before oscillations are quenched. The damage was FD to W_0 in the 2D 100 cell network. The activity settles into a limit cycle, demonstrating oscillatory behavior. (d) Same as (c), but at the following damage level. The activity decays to a fixed point. For the plots in (c) and (d) only, an odor input that is constant in time was used.

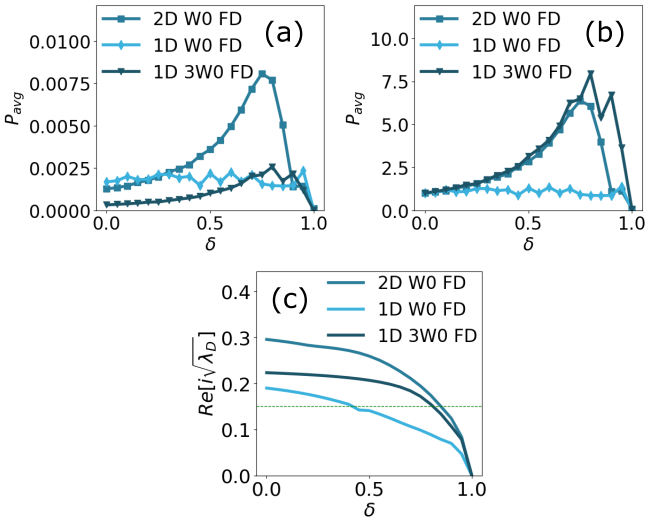

Figure 2.8: (a) Average oscillatory power (P_{avg}) for FD delivered to W_0 in the 2D 100 cell network, the 1D 100 cell network, and the modified 1D 100 cell network. The modified network starts the damage trial with $W_{0,\text{modified}} = 3W_{0,\text{unmodified}}$. The modified network shows a rise in P_{avg}, similar in shape to the 2D network. (b) Same as in A, but with P_{avg} normalized with respect to its initial value in each case, illustrating more clearly the similarity in behavior between the modified 1D and the 2D networks. (c) The real part of i times the square root of the dominant eigenvalue ($Re[\text{i}\sqrt{\lambda_D}]$) plotted against δ for FD delivered to W_0 in the 2D 100 cell network, the 1D 100 cell network, and the modified 1D 100 cell network. The dominant eigenvalue of the modified network still starts below that of the 2D network, but it stays above threshold until a similar level of damage.

and P_{avg} begins at a lower value. As damage is applied and the network approaches its null condition (at $\delta = 2/3$ because W_0 is tripled), P_{avg} increases. This creates a trajectory of behavior with damage that closely resembles that of the 2D network (Fig. 2.8(a)(b)).

This is illustrated also by the behavior of the leading eigenvalue, which indicates the presence of oscillations (as seen in Fig. 2.7). With a larger weight matrix, the leading eigenvalue of the matrix A starts at a larger value, and its trajectory is similar to that of the 2D networks. The unmodified 1D network's leading eigenvalue begins about 2/3 along the trajectory of the modified and so crosses threshold at a lower level of damage (see Fig. 2.8(c)).

These results demonstrate that the primary difference between the 1D and 2D networks is that they operate in different regimes: the maximum activity state the 2D networks can sustain is greater than that of the 1D networks. Thus, at the initial oscillation size in this model, the 2D networks are below their maximum oscillatory power, while the 1D networks are already at near maximum. The mechanism underlying this difference in maximum activity is beyond the scope of this paper, but it could be due to a greater capacity for cooperative effects resulting from the greater level of connectivity in the 2D networks.

2.4 Discussion

Seeded Damage

The linearized analysis here is carried out for Flat Damage, but Seeded Damage, which spreads outward from a starting unit, shows a similar increase in oscillatory power at moderate levels of damage and relies on the same mechanisms. That we found similar behavior for SD is important as it better represents a potential method of pathology progression. In PD, for example, misfolded α-synuclein spreads from cell to cell before neuron death[102, 103] in what many believe is a prion-like manner[104–106], although the precise mechanism and the level of damage in the donor cell before transmission is still an active area of investigation[107, 108]. Similarly, evidence suggests prion-like spread of AD pathology as well, of both Aβ[109, 110] and tau[111–113].

Relation to Aberrant Olfactory Bulb Activity in Animal Models of Disease

Our model's mechanism for the increase in gamma band oscillatory power is the increase in MC activity. This could be representative of higher firing rates of participating MCs, or of recruitment of less active MCs within the population represented by the active units (as previously inactive units rarely activate in our model, though they theoretically could). The increase in MC activity is due to a reduction of inhibition, either by decreasing GC excitation from the MCs (damage to W_0, which could represent less AMPA receptor activation in GCs) or by decreasing inhibition of MCs by GCs (damage to H_0, which could represent less GABA receptor activation in MCs by GABA receptor loss or reduced GABA transmission from GCs). Either damaging W_0 or H_0 (or both) could be consistent with loss of dendrodendritic synapses. Generally, our model implies that reduced GABA transmission leads to increased gamma oscillations, a result relevant to several experimental studies.

W. Li *et al.* and Chen *et al.* measured OB activity in mice expressing amyloid precursor protein and presenilin 1 (APP/PS1) and found significant increases in gamma band power associated with synaptic deficits[6, 7]. Both groups found that treatment with a GABA agonist decreased the heightened gamma power, suggesting that increases in the gamma band may have been due to a decrease in GABA-induced inhibition to the MCs. W. Li *et al.* also measured increased MC firing rates, although measurements of cell activity were done on OB slices rather than *in vivo*[7]. Note that by including PS1, these two studies may be more specifically relevant to familial AD rather than to sporadic AD[114], and it is not clear that the effects seen were due to Aβ alone. Other studies have also found increased gamma power in OBs of transgenic AD mice models[8, 71], with S. Li *et al.* working with expression of p-tau (P301S mice) rather than APP. While they also found an increase in

gamma power and impaired synaptic function, MC firing rates were decreased rather than elevated, suggesting other mechanisms at play. Note also that because AD-like pathology was induced by gene expression in all of these studies[6–8, 71], it is more relevant to the FD modeled here rather than to SD.

The observations of these studies closely relate to work by Lepousez and Lledo[27], who found that GABA antagonist increased oscillations in the gamma band and GABA agonist had the opposite effect. However, they found that MC firing rates were not significantly affected by GABA antagonist (except possibly for increased excitation of MCs that were initially less active), instead showing that the power increase was likely due to increased MC synchronization. Additionally, they found an important reliance on NMDA channels in GCs, which could be relevant to PD since NMDA receptors may be among the targets of pathological α-synuclein[86]. Our model is limited in this regard by a lack of explicit NMDA activity and a clear mechanism for varying synchrony.

While the research mentioned above found increases in gamma oscillations, it should also be noted that some studies have found decreases in OB oscillations in the presence of Aβ. Hernández-Soto *et al.* applied Aβ by injection and measured activity *in vivo* in rat OBs an hour after application[79], and Alvarado-Martínez *et al.* measuring cell activity in mouse and rat OB slices *in vitro* after bath application of Aβ[115]. Both found overall decreases in OB activity.

To our knowledge, few studies have measured olfactory bulb neural activity in the presence of PD-like pathology. Kulkarni *et al.* recorded local field potentials in mice olfactory bulbs after injection of α-synuclein pre-formed fibrils directly into the OB. They measured a significant increase in oscillatory power in the beta band (15-30 Hz) following incubation periods ranging from 1-3 months. Zhang *et al.* modeled PD pathology in mice by reducing the population of dopaminergic neurons in the substantia nigra in mice[78]. They measured

an increase in the spontaneous oscillatory power of all bands, theta (2-12 Hz), beta (15-35 Hz), and gamma (36-95 Hz). The full extent of the mechanisms underlying the observations in both of these studies is outside the scope of this model. Dopaminergic input to the OB from the substantia nigra was not modeled here, although it could be possible that the net effect of reducing that input is less inhibition to the MC population. As for the first study, beta oscillations in particular require centrifugal input and rely on channels not modeled here (although the same interactions modeled here are also critically involved, see [29, 60]). The Li-Hopfield model includes centrifugal input to the GCs in only a superficial way, and greater detail is required to reproduce beta oscillations in the OB.

Of note, thus far, experimental studies have shown differences between OB activity in PD-like pathology compared to AD-like pathology. Though modeling these differences lies outside the scope of the present model, if the disease-specific alterations in oscillatory power in the olfactory bulb prove robust, it provides a potential tool for differentiation in early diagnosis of neurodegenerative disease.

Conclusions and Future Directions

Despite the limitations of the model presented here, we believe it is nevertheless relevant to investigating the effects of neurodegenerative damage on oscillatory activity in the olfactory bulb. The balance between inhibitory and excitatory activity between the MC and GC populations is essential to gamma oscillations and depends on multiple mechanisms and principles[27]. Here, we highlight one principle, which is that as long as inhibition is great enough, marginal decreases in inhibitory action will increase gamma oscillations due to the nonlinear nature of the neural activity[116]. Because it's unlikely that a biological network would begin close to the regime of maximum oscillatory power (and thus close to the drop off

seen in Fig. 2.7), we would expect to see this effect with moderate damage to the inhibition.

The model here spotlights one mechanism that may be in play, and serves as a proof of concept that computational modelling can help give insight into OB dysfunction. More detailed models of the OB network and activity are needed to explore other mechanisms and effects of neurodegenerative damage. For example, working with a model based on work by Osinski *et al.*[51] or David *et al.*[55] may offer insight into the modulation of beta oscillations found by Kulkarni et. al[9]. And a model similar to that by Li and Cleland[117] may help investigate effects of cholinergic perturbation in AD, as reviewed by Doty[5].

The prevalence of olfactory dysfunction in neurodegenerative disease presents both an opportunity and a challenge; it is a common early symptom[3–5], yet its applicability in diagnosis is limited by the broadness of its presence. Thus it is important to continue the study of the mechanisms and behavior of OB oscillations in the presence of neurodegenerative damage since, as discussed above, aberrant OB oscillatory activity may show a point of differentiation between PD and AD pathology. Additionally, recent progress in non-invasive measurement of human olfactory bulb activity[118] brings this area of research closer to clinical relevance. For example, Iravani *et al.* used surface electrodes to measure electroencephalogram (EEG) activity originating from the olfactory bulb in human patients, specifically in the gamma range[118]. As these techniques are developed, understanding the aberrant OB activity in neurodegenerative diseases could be a powerful tool for realizing earlier diagnosis of these illnesses.

Chapter 3

Graded inhibition in a large-scale mechanistic model of the olfactory bulb network

3.1 Introduction

Both Alzheimer's disease (AD) and Parkinson's disease (PD) pathology have measurable effects on oscillatory activity in the olfactory bulb (OB)[6–9, 59]. Given the involvement of the OB in early stages of these diseases[3–5], as well as recent advancements in measuring human OB activity non-invasively[118], there are compelling reasons for further investigating and modeling the oscillations of the OB. Greater insight into OB oscillation perturbations in the presence of pathology could in turn lead to greater understanding of disease mechanisms and potentially to tools for earlier diagnosis of disease.

Some studies of the effects of Alzheimer's disease on OB oscillatory activity[6, 7] have highlighted the particular importance of gamma oscillations (40-80 Hz). Gamma oscillations in the olfactory bulb arise from the interaction between mitral cell (MC) and granule cell

(GC) dendrites[12, 21, 26]. External input stimulates MC firing which excites the GCs, and the GCs inhibit the MCs, even in the absence of GC spikes[14, 20], leading to gamma oscillations. Alzheimer's disease studies found that these gamma oscillations were strengthened in the presence of pathology[6, 7], highlighting the relevance of particular results from an *in vivo* experiment by Lepousez and Lledo[27]. They found increased oscillatory power in the gamma band with application of GABAergic antagonist, implying that AD pathology may reduce the effectiveness of GABA transmission. This increase in oscillatory power was accompanied by a reduction in the dominant gamma frequency. Many models of OB oscillations exist which have expanded our understanding of oscillatory activity in the OB, as reviewed in Chapter 1. However, to my knowledge, no biophysical model has been able to reproduce increased gamma power and decreased gamma frequency when inhibitory conductance is reduced, as found by Lepousez and Lledo. This implies that crucial details of the mechanisms underlying gamma oscillations in the OB are yet to be determined.

With the goal of investigating those mechanisms, I work with the model developed by Kersen, Tavoni, and Balasubramanian[45]. It is a large-scale, mechanistic model of single-compartment neurons that reproduced both gamma oscillations and beta oscillations (14-30 Hz) in the olfactory bulb. The network connectivity is generated based on cell and dendritic density pulled from imaging data, and the generation process required only slight adjustment to track each synapse location (important for future work, see Ch. 4). Their work with the model was focused on the impact of their network generation method on connectivity patterns, odor decorrelation, cortical feedback and oscillations, in addition to some modeling of GC neurogenesis[45]. Although it produced oscillatory activity, the mechanism of oscillation generation in their model was not explored.

I work with and modify their model to capture various aspects of OB activity during gamma oscillations, including low GC spiking[119, 120], physiological levels of MC firing

rates[27, 121], and graded inhibition[13, 21, 22]. The implementation of graded MC inhibition results in activity-dependent MC inhibition, a feature of the OB explored in [62]. While I find gamma oscillations with lower GC firing (via a tonic GC inhibitory channel), the oscillations in the simulations using graded MC inhibition are in the high-theta to low beta range. Robust gamma oscillations in this model framework could feasibly be produced via entrainment[52, 55] by adjusting the mitral cell dynamical equations for resonant spiking activity[122]. In this way, the model could use tonic GC inhibition and graded MC inhibition to simultaneously achieve activity-dependent MC inhibition and gamma oscillatory activity with physiological levels of MC and GC spiking.

3.2 The Kersen, Tavoni, and Balasubramanian Model of the Olfactory Bulb

Here, I summarize the network generation process, dynamical and synaptic equations, and limitations of this framework, focusing on the elements most relevant to this work. For more details about the workings of their original model, see [45].

3.2.1 Network Generation

The olfactory bulb space is defined as a layered cylinder with the number of glomeruli determined by the cylinder's cross-sectional area and glomerular density calculated from data[45, 123–125]. The glomerular projections are set at random x-y locations and assigned 15-25 mitral cells each. The mitral cells are distributed around the x-y location of their associated glomerulus with lateral dendritic radii assigned randomly based on experimental measurements in [126]. Granule cell dendritic trees are modeled as cones that project into

the external plexiform layer (EPL) of the OB, where they overlap with the areas defined by the MC lateral dendritic radii. The overlap between a GC cone and a MC dendritic area is used to calculate the probability of forming a dendrodendritic synapse based on GC spine density and MC radius-dependent dendritic density[45, 127, 128] (see Fig. 3.1). GCs are generated one by one until the ratio of GCs to MCs is 15:1, in the work here resulting in a network of 1793 MCs and 26895 GCs, which is half the size of the network in [45].

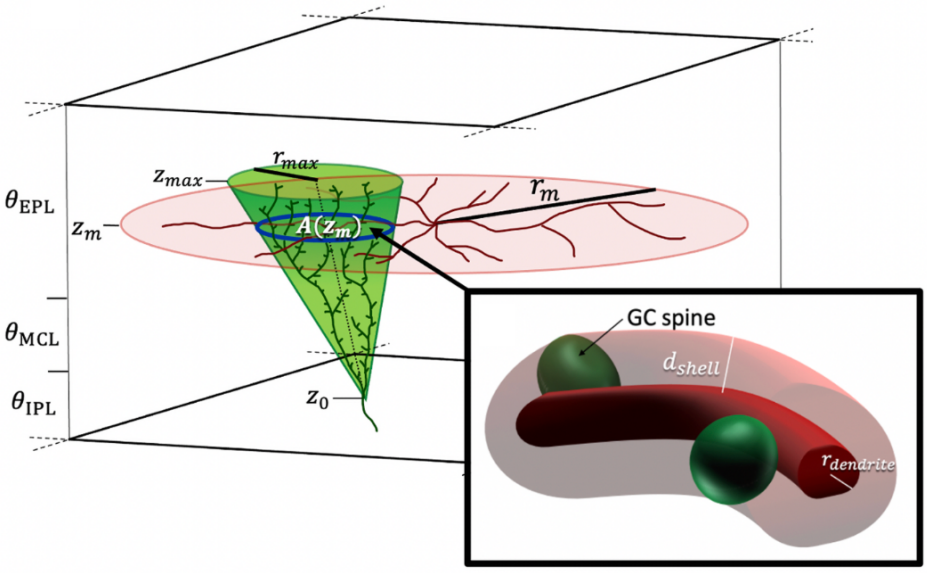

Figure 3.1: **Model Diagram.** Figure from [45], illustrating the MC radius and the GC cone extending into the EPL. Synapse probability was calculated based on the overlapping dendritic areas as well as the GC spine density (lower right). These dendritic geometries are used only for generating the network connectivity and determining synapse locations, as the cells are modeled as single compartments.

3.2.2 Dynamics and Synaptic Equations

The cellular dynamics are described by the Izhikevich equations, which have been shown to reproduce a wide variety of observed neuron firing patterns[122, 129]. Each cell is a single compartment, two variable quadratic integrate and fire model, following the Izhikevich

Table 3.1: Parameters for the Izhikevich equations, from [45].

Parameter	Mitral Cell	Granule Cell
v_r	-58 mV	-71 mV
v_t	-49 mV	-39 mV
v_c	30 mV	25 mV
C	191 pF	48 pF
k	2.5 nS/mV	0.067 nS/mV
a	0.02 ms^{-1}	0.01 ms^{-1}
b	12 nS	-0.133 nS
c	-70 mV	-75 mV
d	13 pA	2 pA

formulation:

$$C\frac{dv}{dt} = k(v - v_r)(v - v_t) - u + I_{syn} \tag{3.1}$$

$$\frac{du}{dt} = a(b(v - v_r) - u) \tag{3.2}$$

$$\text{If } v \geq v_c, \text{then} \begin{cases} v \longleftarrow c \\ u \longleftarrow u + d \end{cases} \tag{3.3}$$

where C is the membrane conductance, v is the membrane potential, v_r is the resting potential, v_t is the threshold potential, u is the recovery current, and I_{syn} is the sum of synaptic currents[45]. The variables $k,\ a,\ b,\ c$, and d are free parameters, same as in [45], chosen to reflect MC and GC firing from [53, 126, 130] (see Table 3.1 for values).

Each MC is modeled as having 100 synaptic connections to its glomerulus, each synapse receiving Poisson input through an AMPA channel and an NMDA channel with a time-

varying rate of the form:

$$r(t) = \frac{r_{max}}{2} + \frac{r_{max}}{4}(sin(2\pi ft - \phi) + 1) \tag{3.4}$$

[45], where f is 6 Hz, representing the frequency of sniff-driven glomerular input. A mean phase is drawn from a uniform distribution from 0 to 2π for each glomerulus, then ϕ is drawn from a Gaussian distribution with mean equal to the corresponding glomerulus phase and a standard deviation of $\pi/4$, based on [131]. The maximum rate r_{max} was drawn from a Gaussian with mean μ_r between 2-3 Hz for glomeruli activated by the odor and between 0-0.25 for all other glomeruli (with standard deviation of $\mu_r/10$). In the original model, 20% of glomeruli were activated by an odor, but here I activate all glomeruli to simulate broad activation of the olfactory bulb and vary μ_r to observe its effects on the power spectrum and on MC and GC firing (Section 3.3.2 and 3.3.3).

MCs receive inhibitory input from the GCs through GABA channels, and GCs receive excitatory input from the MCs through AMPA and NMDA channels. The AMPA current through a synapse is of the form:

$$I_{AMPA}(t) = s_{AMPA}(t)g_{AMPA}(V(t) - E_e) \tag{3.5}$$

where $s(t)$ represents the fraction of open channels, g_{AMPA} is the conductance, $V(t)$ is the membrane potential, and $E_e = 0$ mV is the reversal potential for excitatory channels[45]. Values for synaptic parameters are given in Table 3.2 and are as in [45]. The current for GABA channels on MCs includes an additional term to account for degradation of the

inhibitory signal as it propagates from the lateral dendrite to the soma[132],

$$I_{GABA}(t) = s_{GABA}(t) g_{GABA}(V(t) - E_i) exp(-L/\lambda) \tag{3.6}$$

where $E_i = -70$ mV is the reversal potential for inhibitory currents, L is the distance from the synapse to the MC soma, and λ is the length constant[45]. The NMDA current has the form[133]

$$I_{NMDA}(t) = s_{NMDA}(t) g_{NMDA}(V(t) - E_e) B(V) \tag{3.7}$$

$$B(V) = \frac{1}{1 + \frac{[Mg^{2+}] exp(-0.062V(t))}{3.57}} \tag{3.8}$$

where B(V) describes the voltage dependence of the magnesium block, with $[Mg^{2+}] = 1$ mM[134].

When a MC or GC fires, the release of neurotransmitter is represented by updating the gating variables, $s(t)$, for the AMPA or GABA channels of the receiving cells as

$$s(t) \longleftarrow s(t) + W(1 - s(t)) \tag{3.9}$$

where $W = 0.5$. For AMPA and GABA channels, $s(t)$ follows a simple decay[135],

$$\frac{ds}{dt} = -\frac{s}{\tau} \tag{3.10}$$

where the decay constant τ depends on the type of channel. The gating variable for NMDA

channels takes the rise time into account by involving a second variable, n,

$$\frac{ds_{NMDA}}{dt} = -\frac{s_{NMDA}}{\tau_{NMDA_{decay}}} + \alpha n(1 - s_{NMDA}) \tag{3.11}$$

$$\frac{dn}{dt} = -\frac{n}{\tau_{NMDA_{rise}}} \tag{3.12}$$

with n being updated when a connected MC fires, in the same way as $s_{AMPA}(t)$ and $s_{GABA}(t)$ ([45]).

In the OB, GCs also release GABA in a graded manner[13, 21, 22] independent of somatic spiking[14, 21]. This is particularly important in light of observations that GCs rarely spike[119]. In the original model presented in [45], spike-independent inhibition is implemented by updating $s_{GABA}(t)$ for MCs connected to GCs activated by a spiking MC. That is, when a MC spikes, the AMPA and NMDA gating variables of connected GCs are updated as previously stated, and the GABA gating variables for MCs connected to those GCs are updated as

$$s_{GABA}(t) \longleftarrow s_{GABA}(t) + \kappa W(1 - s_{GABA}(t)) \tag{3.13}$$

where $\kappa = 0.006$. In the work that follows, I vary the factor κ and then implement alternate methods of spike-independent inhibition, i.e., graded inhibition.

Power spectra are computed from the local field potential (LFP), which is modeled as

$$\phi(\mathbf{r}_e, t) = \sum_j \frac{I_{AMPA_j}(t) + I_{NMDA_j}(t) + I_{GABA_j}(t)}{4\pi\sigma|\mathbf{r}_e - \mathbf{r}_j|} \tag{3.14}$$

[45, 136, 137] where I_j is the current through the jth synapse, $\sigma = 1/300$ $(\Omega$ cm$)^{-1}$ is the exctracellular conductivity, $\mathbf{r}_j$ is the position of the jth synapse, and $\mathbf{r}_e$ is the electrode position, placed in the center of the x-y plane and halfway down the EPL layer.

Table 3.2: Synaptic parameters, as in [45]. AMPA and NMDA parameters for MC inputs were chosen to match [138] and thus differ from those for the GCs.

Parameter	Mitral Cell	Granule Cell
g_{AMPA}	6.7 nS	0.73 nS
g_{NMDA}	12 nS	0.84 nS
g^{*}_{GABA}	0.13 nS	N/A
$\kappa^{*\dagger}$	0.006	N/A
τ_{AMPA}	14.3 ms	5.5 ms
$\tau_{NMDA_{rise}}$	13 ms	10 ms
$\tau_{NMDA_{decay}}$	70 ms	80 ms
$\tau^{\ddagger}_{GABA}$	18 ms	N/A
λ	675 μm	N/A
α	0.03 ms^{-1}	0.1 ms^{-1}

* Varied in Section 3.3
† Not used in graded inhibition experiments
‡ Not used in Section 3.3.2

3.2.3 Model Limitations

The model as described above yields oscillatory activity in the beta band (see Fig. 3.2(a)), although not as dominantly as in [45] where they used a larger network size. Because beta oscillations are associated with higher GC excitability[29, 51, 55, 60], gamma oscillations in the original model are obtained by "inactivating" a portion of the GC population[45]. That is, the network was regenerated but with a GC to MC ratio of 5:1 instead of 15:1 (Fig. 3.2(b)). Ideally though, a model network would be able to generate gamma oscillations with the full complement of cells.

Additionally, experiments *in vivo* (on anesthetized animals) and *in vitro* have shown that GCs spike infrequently[61, 119, 139]. In the original model, more than 76% of GCs spiked on average ($76.17 \pm 0.76\%$), whereas one experimental study was able to evoke somatic spiking

in only about a third of GCs[119].

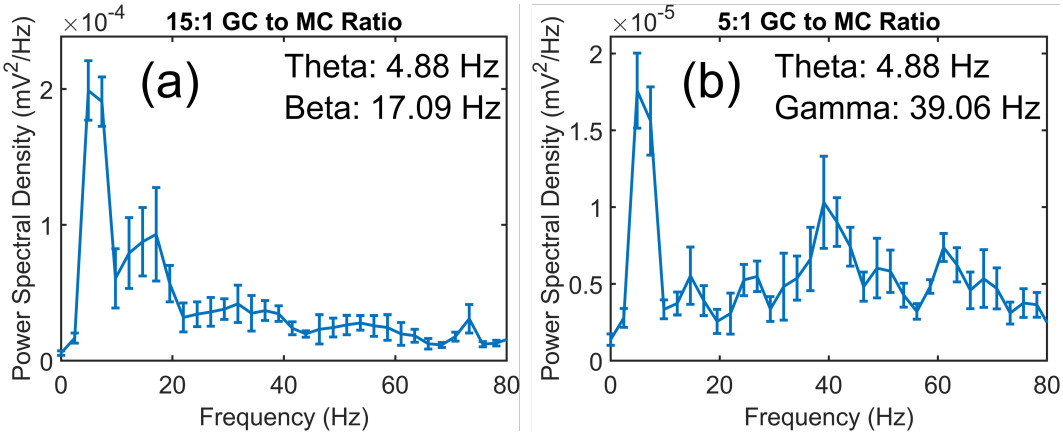

Figure 3.2: **Oscillatory Activity in the Base Model.** The original model produces (a) beta oscillations with the default 15:1 granule to mitral ratio. (b) When the ratio is reduced to 5:1, the model generates gamma oscillations.

If GC spiking is to be reduced, the form and magnitude of spike-independent inhibition to the MCs needs to be adjusted. I vary the factor κ in the results that follow, but this method in the base model depends only on the connectivity of the GCs and not at all on their state. Experiments show that the GCs release GABA in a graded manner[13, 22] dependent on local dendritic Ca^{2+} concentration independent of somatic action potentials[20, 21].

Mitral cell spiking in the base model is also significantly lower than experimentally recorded in both spontaneous and odor-evoked conditions. In the model as described, the average MC firing rate was 6.73 ± 0.18 Hz with $71.67 \pm 0.60\%$ not firing at all. However, several experimental studies find average spontaneous MC firing rates in the 20-30 Hz range *in vivo*[27, 121], although a more recent study found a distribution of MC firing rates that skewed lower[140]. Even in the absence of odor input, though, spontaneous MC participation is high, with two-thirds or more of the population exhibiting spikes[121, 140].

The goals of the changes to the model therefore are to achieve gamma oscillations with (1) the full complement of GCs, (2) low GC spike participation, and (3) average MC spiking

inside the experimentally measured range with low levels of silent MCs. In pursuit of these objectives, I add a tonic inhibitory current targeting the GCs, replace the original method of spike-independent inhibition (Eqn. 3.13) with graded inhibition, and vary the amplitude of input to the MCs and the conductance of the MC GABA channels. While the simultaneous achievement of all three goals was not found here, the pursuit yielded insight into the generation of oscillations in this framework and into activity-dependent lateral inhibition of MCs[62]. Ideas for achieving increased gamma power and decreased gamma frequency with reduced GABA conductance are discussed in Chapter 4.

3.2.4 Code Accessibility

All simulations of this model are run on MATLAB (versions R2019 or R2023) using the forward Euler method with a time step of 0.1 ms, as in [45]. Code for the simulations and plots that follow can be found online at
`https://github.com/jkberry07/KTB_Graded_Inh`.

3.3 Modifications to the Model and Results

3.3.1 Tonic Inhibition to Granule Cells

To reduce GC spiking and excitability, I added a tonic inhibitory current targeting the GCs[141] of the form,

$$I_{tonic} = g_{tonic}(V - E_i) \tag{3.15}$$

where g_{tonic} is varied in the experiments that follow, and $E_i = -70$ mV as before. This current excludes the gating variable, and thus the channel is always open. In experiments

using this tonic inhibition, its contribution to the LFP was computed as

$$\phi_{tonic} = \sum_n \frac{I_{tonic_n}(t)}{4\pi\sigma|\mathbf{r}_e - \mathbf{r}_n|} \tag{3.16}$$

where I_{tonic_n} is the tonic inhibitory current through the nth GC, $\mathbf{r}_n$ is the position of the vertex of the nth GC cone, and σ and $\mathbf{r}_e$ are as before.

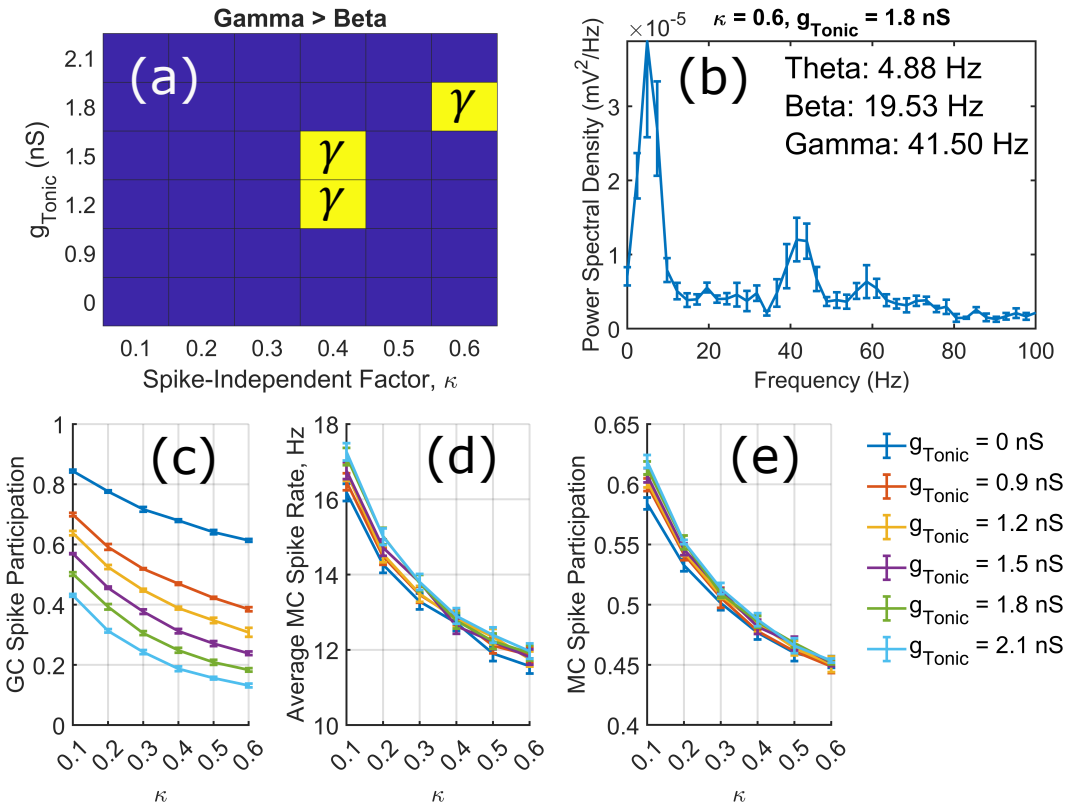

Figure 3.3: **Tonic Inhibition Experiments.** In these experiments, input parameter μ_r was a minimum of 1.75 and a maximum of 2.75 for all MCs (broad activation). (a) Yellow boxes mark points where the peak gamma power was greater than the peak beta power without overlapping error bars. (b) Example power spectrum where gamma was significantly greater than beta, for the point $\kappa = 0.6$, $g_{tonic} = 1.8$ nS. (c) The fraction of GCs that spiked at least once during the last 800 ms of simulated time (the first 200 ms are trimmed to remove initial transients). (d) The average MC firing rate during the last 800 ms of simulated time. (e) The fraction of MCs that did not spike during the last 800 ms of simulated time. All error bars are standard error of the mean.

When the conductance of the tonic inhibition to the GCs is varied with the spike-independent inhibition factor κ, beta oscillations generally dominate over gamma oscillations, as in the base model. Only three parameter regions in the range explored yield gamma oscillatory peaks that are larger than beta peaks without overlapping error bars (Fig. 3.3(a)(b)). In those regions, the fraction of GCs that spike fall within a reasonable range compared to experiment (0.19 - 0.4)[119], but the MC spike rate is too low (11.9 Hz to 12.8 Hz) and the fraction of participating MCs is too low (less than half). For example, for the trials yielding the power spectrum shown in Fig. 3.3(b) ($\kappa = 0.6$, $g_{tonic} = 1.8$ nS), GC spike participation is 0.184 ± 0.006, MC spike rate is 11.9 ± 0.2 Hz, and the fraction of participating MCs is 0.453 ± 0.002. Tonic inhibition is effective at lowering the spiking of GCs (Fig. 3.3(c)), but not at increasing the average MC spike rate or MC participation (Fig. 3.3(d)(e)). Increasing κ increases the effectiveness of the original method of spike-independent inhibition to the MCs, reducing the MC firing rate and participation (Fig. 3.3(d)(e)), leading to a lower fraction of GCs spiking (Fig. 3.3(c)).

3.3.2 Graded Inhibition to Mitral Cells

The form of GC-mediated MC inhibition independent of GC spiking in the original model entirely ignores the state of the GC and its synapses, essentially creating direct MC-MC inhibition. Here, I implement a method of graded inhibition that depends both on the state of the GC as a whole and on the state of the particular synapse in question. This method is inspired by a model from Osinski and Kay[51] where they calculate the probability of GABA release based on calcium concentration in GC dendrites. The calcium current comes through both N-type voltage-dependent calcium channels and NMDA channels. Although the N-type channels play an important role in producing beta oscillations when NMDA

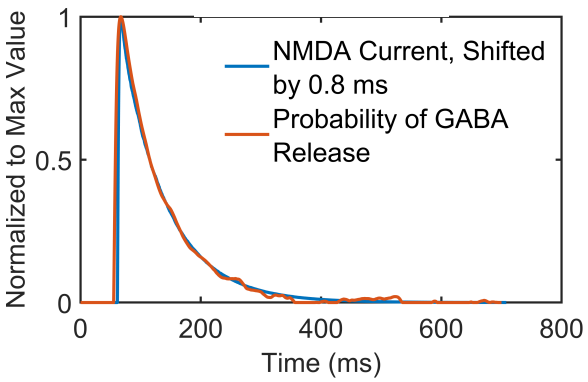

Figure 3.4: **NMDA Current Compared to Probability of GABA Release in the Osinski-Kay Model.** When the NMDA current and probability of GABA release are normalized, it becomes clear that GABA release closely follows and is directly proportional to the NMDA current in the Osinski-Kay model of the OB for both low GC excitability (shown above) and high GC excitability (not shown). The plots presented in this figure are re-scaled versions of the plots in Fig. 3A (middle row) and 3D from [51], with calcium dependent inactivation (CDI) of the N-type channels, which is the default mode of their model.

current is removed from the model, the probability of GABA release from a GC dendrite in the default version of the model is mostly dictated by the NMDA current to that dendrite[51] (see Fig. 3.4). Therefore, I make the GABA release directly proportional to the openness of the NMDA channel at that synapse,

$$s_{GABA_j}(t) = s_{NMDA_j}(t)B(V_n) \tag{3.17}$$

where $B(V_n)$ is the voltage dependence of the magnesium block for the nth GC to which the jth synapse belongs. The gating variable thus requires the same two conditions to be met as the NMDA current at that synapse. That is, the membrane potential of the GABA-releasing GC must be high enough to relieve the magnesium block, and the MC receiving the inhibition must have spiked recently enough that $s_{NMDA_j}(t)$ is still open (Fig. 3.5). This mechanism for graded inhibition has particular relevance to experimental findings that the

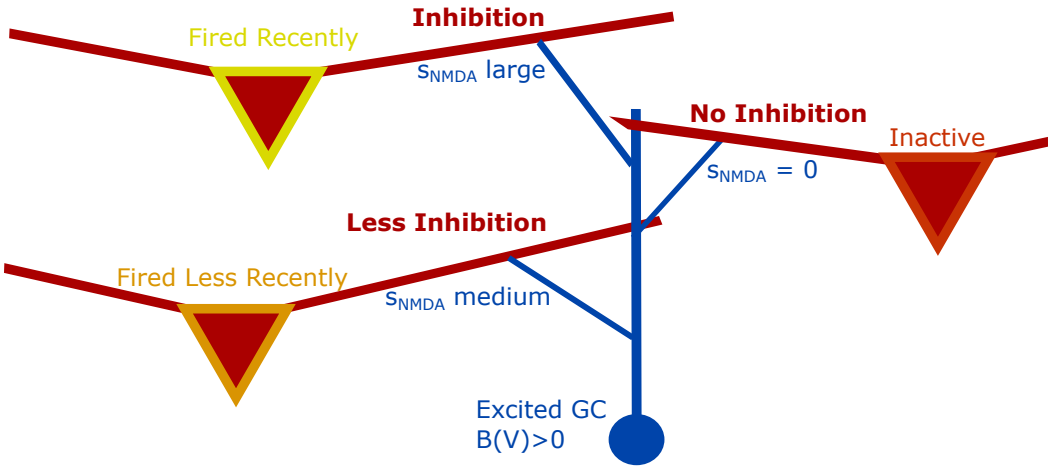

Figure 3.5: **Graded MC Inhibition.** For a GC excited to a membrane potential, V, the level of inhibition it releases onto a given MC depends on the history of that MC's spiking. If the MC spiked recently, then it receives an inhibitory current. If the MC has not spiked, then s_{NMDA} for that synapse is 0 and it receives no graded inhibition. While cells are modeled as single compartments, s_{NMDA} is modeled for each synapse individually.

inhibition received by a MC is activity-dependent[62], with a crucial role played by GC NMDA receptors[20]. It is also distinct from Osinski and Kay because their model tracked the calcium concentration for the GC dendrite as a whole rather than for each synapse[51], and thus the inhibition received by the postsynaptic MC was not activity-dependent.

In the experiments implementing graded inhibition, the MC GABA conductance is varied, along with the GC tonic inhibitory conductance and the minimum value of the MC input parameter μ_r (each MC has a μ_r between the minimum value and the minimum plus one; e.g., if $\mu_{r,min} = 2.75$, then μ_r is between 2.75 and 3.75 for each MC in that trial). With only graded MC inhibition, the smallest MC spike participation observed in any trial is 0.9978, reflecting the activity dependence of the inhibition.

GC participation showed an unexpected relationship with MC input and MC GABA conductance (Fig. 3.6(b)). Increasing the MC input and decreasing $g_{GABA,MC}$ predictably increases the average MC firing rate (Fig. 3.6(a)), but surprisingly decreases the fraction

of GCs that fire. However, the average GC firing rate generally stays the same or slightly increases over those same changes (e.g., compare Fig. 3.6(c) and (b), bottom right of the $g_tonic = 0$ color map). So fewer GCs fire, but at a higher rate.

The firing rate of the MCs decreases slightly with increasing tonic inhibitory conductance to the GCs. Because the inhibition is only graded, when a GC fires and then resets (as in equation 3.3), the MC GABA gating variable closes because the voltage of the GC is now too low for $B(V)$ and so the NMDA current to that GC is zero. Therefore, when the GCs fire more, there is less inhibition to the MCs than when the GCs are being excited but not reaching threshold for spiking. Thus while using only graded inhibition is instructive, it is not appropriate for modeling in this context. While the Osinski-Kay model relied on only graded inhibition, they got around this issue by not modeling GC spikes at all[51]. In the next section, I implement MC inhibition mediated by both GC firing and GC NMDA current (graded).

There are no levels of graded inhibition where gamma is significantly greater than beta (see Section 3.3.4).

3.3.3 Graded and Firing Inhibition

The form of graded inhibition above works well for the activity dependence of MC inhibition, but it neglects the inhibition that should be released when a GC does spike. Therefore, here the MC GABA gating variable at the jth synapse has two parts, graded and firing,

$$s_{GABA_j}(t) = s_{GABA_{j,graded}}(t) + s_{GABA_{j,firing}}(t) \tag{3.18}$$

$$s_{GABA_{j,graded}}(t) = s_{NMDA_j}(t)B(V_n) \tag{3.19}$$

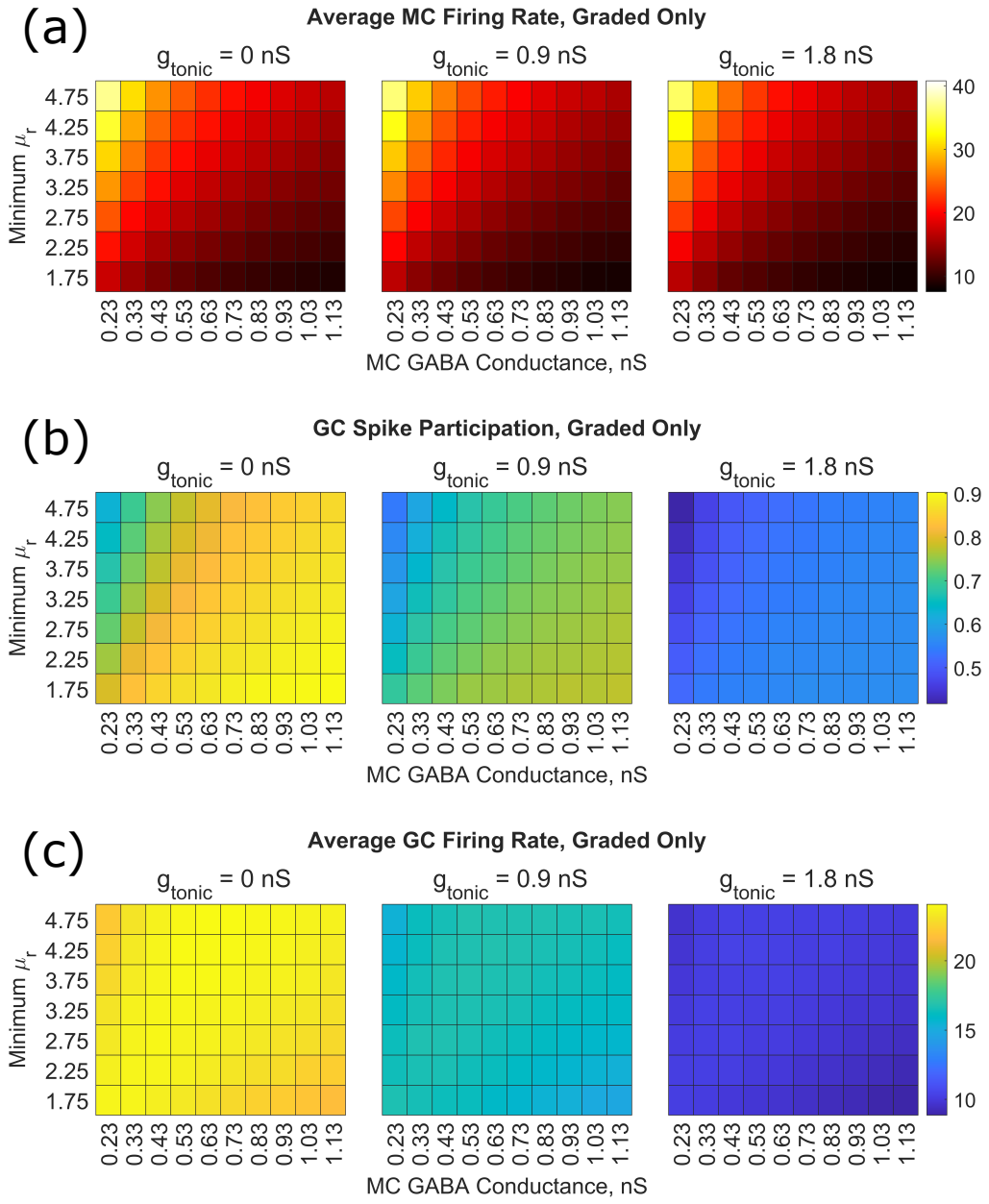

Figure 3.6: **Graded MC Inhibition Experiments, Graded Only.** (a) Average MC firing rate over the last 800 ms of the simulation time, with MC input, MC GABA conductance, and g_{tonic} varied. (b) Fraction of GCs that fired over the last 800 ms of the simulation time. (c) Average GC firing rate over the over the last 800 ms of the simulation time.

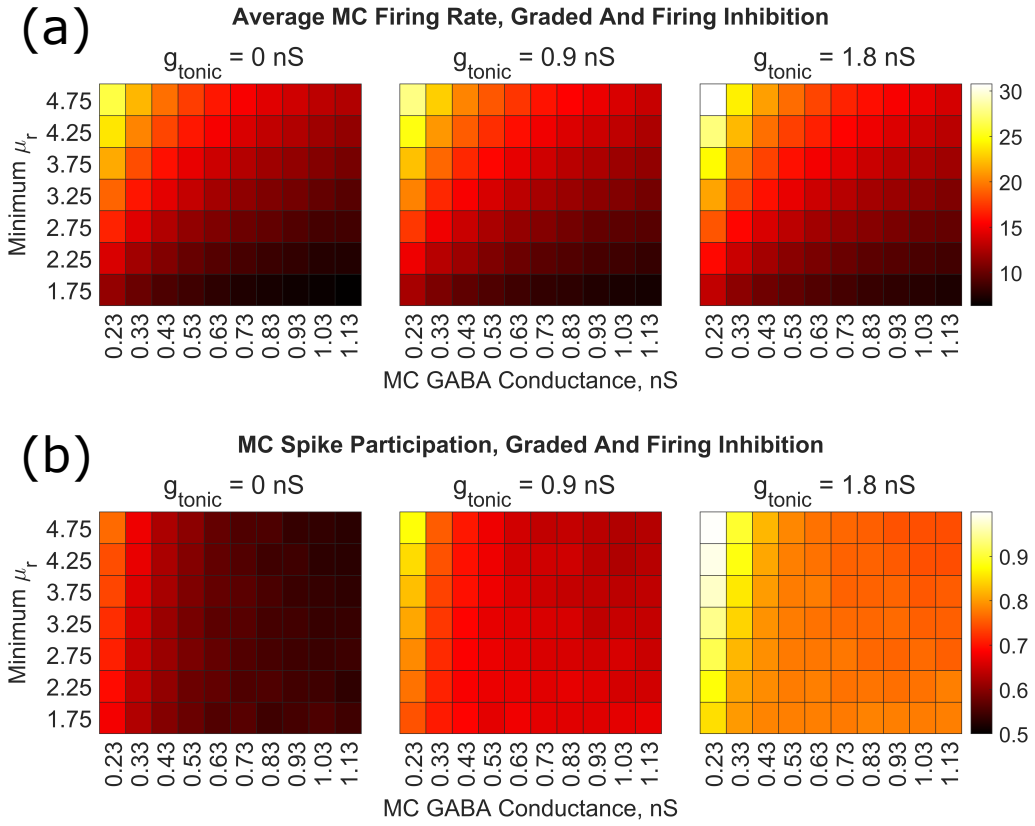

Figure 3.7: **MC Firing Rate and Participation with Graded and Firing MC Inhibition.** (a) Average MC firing rate over the last 800 ms of simulation time. (b) Fraction of the MC population that spiked during the last 800 ms of simulation time.

where the graded portion has the same form as equation 3.17. When the nth GC fires, the GABA gating variables at the jth synapse update as

$$s_{GABA_{j,firing}} \longleftarrow s_{GABA_j} + W(1 - s_{GABA_j}) \tag{3.20}$$

$$s_{GABA_{j,graded}} \longleftarrow 0. \tag{3.21}$$

and $s_{GABA_{j,firing}}(t)$ decays as in equation 3.10. Thus the graded inhibition retains the same dependence as in the previous section, but a GC spike still evokes inhibitory current in all connected MCs.

With both forms of inhibition to the MCs, the average MC firing rate shows the same dependence on MC input and MC GABA conductance as with graded only, but in this case shows greater firing with increased GC tonic inhibitory conductance. The dependence on g_{tonic} is stronger for the MC spike participation, with almost every MC firing at higher inputs and the lowest MC GABA conductance. This demonstrates that with the right parameter choices, the activity-dependence of the MC inhibition can be retained with the reintroduction of GC spike-mediated inhibition. It also suggests that the level of activity-dependence could be tuned by the excitability of the GCs.

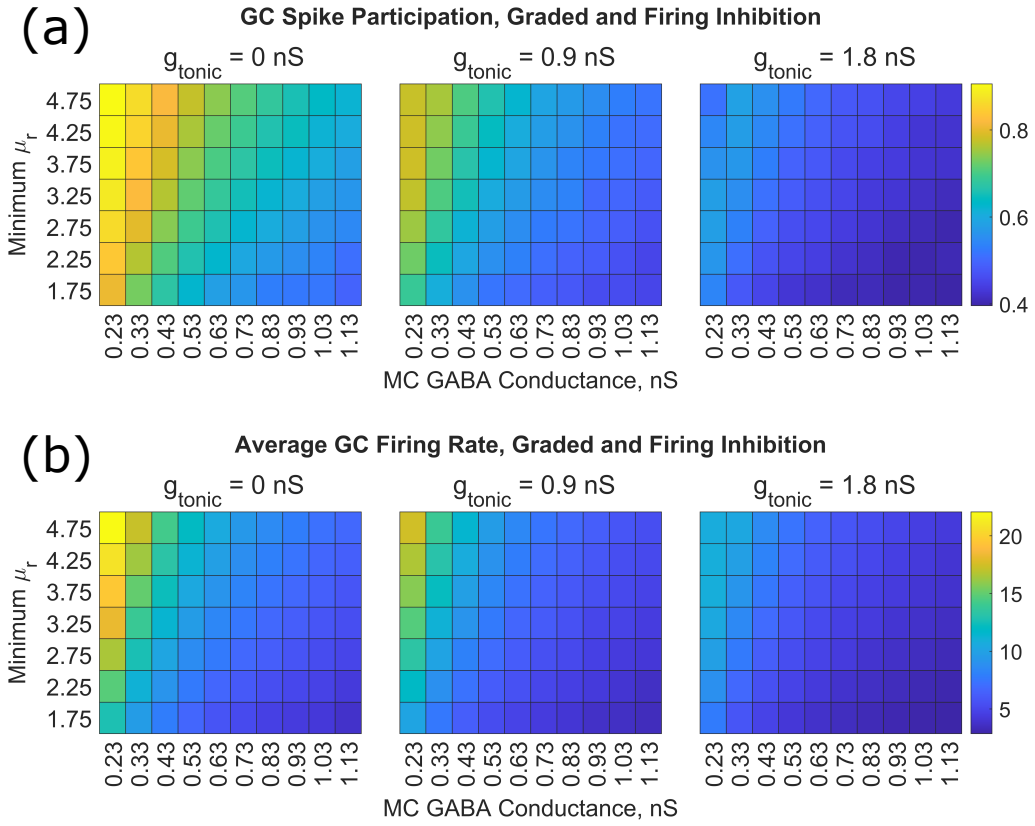

Figure 3.8: **GC Firing Rate and Participation with Graded and Firing MC Inhibition.** (a) Fraction of the GC population that spiked during the last 800 ms of simulation time. (b) Average GC firing rate over the last 800 ms of simulation time.

GC spike participation and firing rate follow similar trends with respect to the MC input

and $g_{GABA,MC}$; the changes in these parameters that lead to greater MC firing lead to greater GC firing and participation. The exception is at the highest level of g_{tonic} with high μ_r where increasing $g_{GABA,MC}$ from 0.23 to 0.33 nS increases the GC participation (Fig. 3.8(a), third panel, upper left), similar to the general trend in the experiments implementing only graded inhibition to the MCs.

3.3.4 Oscillation Results for Graded Inhibition

Gamma oscillations are not significantly larger than beta oscillations for any set of parameters tested here for either form of graded inhibition. The most prominent peak in most simulations using graded and firing inhibition was between 9 and 18 Hz, with another significant peak between 19 and 35 Hz appearing at higher MC GABA conductance and lower MC input (see Fig. 3.9 and Fig. 3.10). Increasing MC GABA conductance and decreasing MC input tended to decrease the frequency of these peaks (Fig. 3.9(a) and (b)) and to increase the peak power (Fig. 3.9(c) and (d) and Fig. 3.10). However, going from MC GABA conductance 1.03 nS to 1.13 nS at the lowest level of MC input, there is a decrease in power for the 19-35 Hz peak, possibly indicating overinhibition of the MCs, especially since the power increases again if μ_r is increased to 2.25 (Fig. 3.9(d), bottom right).

The GC tonic inhibition level has a small effect on the frequency of the spectral peaks (see Appendix, Fig. B.1), but greatly increases the power at higher MC GABA conductance and lower input (see Fig. 3.11). Each change in parameters that leads to higher power (higher MC GABA conductance, lower MC input, higher GC tonic inhibition) also leads to the GC NMDA current having a greater influence on the network dynamics. Lower GC firing because of tonic inhibition means more of the MC inhibition is graded; lower MC input also tends to reduce GC firing (Fig. 3.8), in addition to reducing the number of MCs that are too

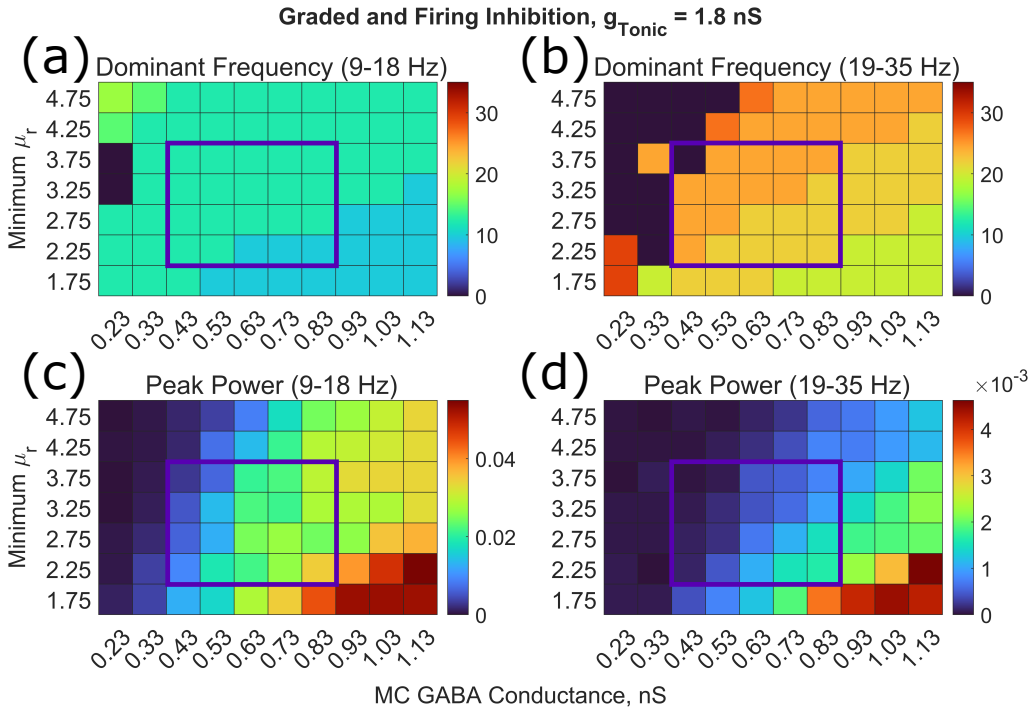

Figure 3.9: **Oscillation Frequency and Power for 9-18 Hz and 19-35 Hz Spectral Peaks with Graded and Firing Inhibition.** (a) Dominant frequency for the 9-18 Hz peak in the power spectrum for $g_{tonic} = 1.8$ nS. (b) Dominant frequency for the 19-35 Hz peak in the power spectrum for $g_{tonic} = 1.8$ nS. (c) Peak power for the 9-18 Hz peak in the power spectrum for $g_{tonic} = 1.8$ nS. (d) Peak power for the 19-35 Hz peak in the power spectrum for $g_{tonic} = 1.8$ nS. Note the different scales for (c) and (d). The purple box shows the region of parameters for which the power spectra are shown in Fig. 3.10.

excitable for synchronization; and larger MC GABA conductance means graded inhibition is stronger. However, MC inhibition from GC firing must be a key part of the prominent 9-18 Hz peak because it did not appear in the graded-only trials (see Appendix B, Fig. B.4).

3.4 Discussion

In the experiments here, simultaneous achievement of the target MC firing levels, GC firing levels, and gamma oscillations is not observed. However, they provide insight into the various

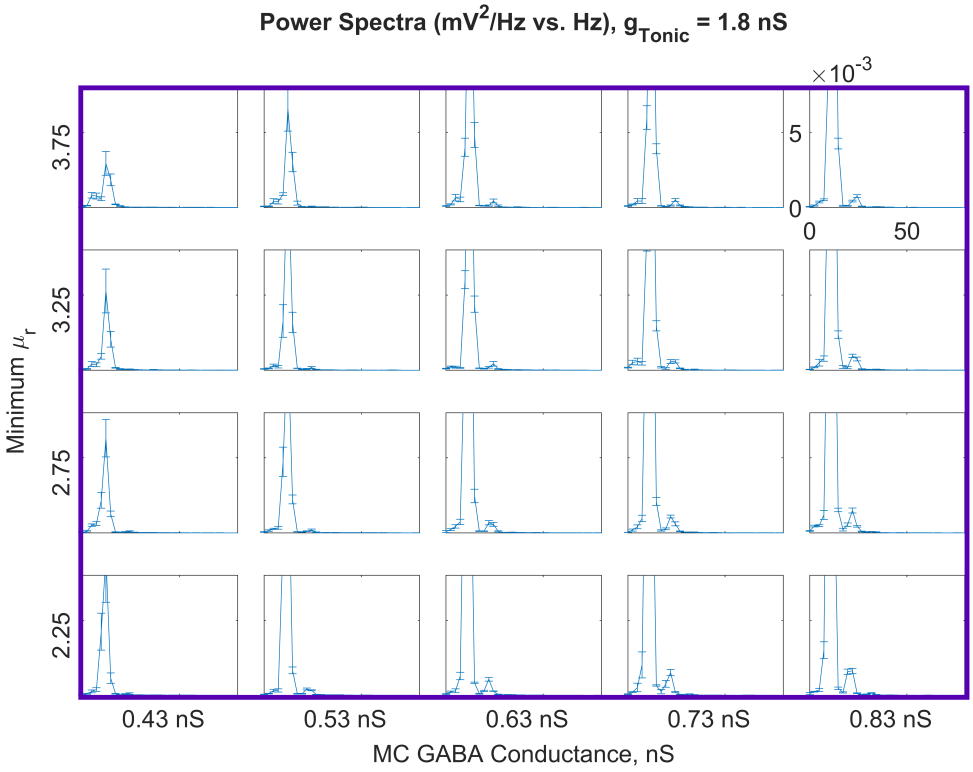

Figure 3.10: **Example Power Spectra with Graded and Firing Inhibition.** Power spectra for $g_{tonic} = 1.8$ nS, arranged by parameter in the same way as the boxed regions in Fig. 3.9.

mechanisms involved.

Tonic inhibition effectively reduces GC participation (Fig. 3.8) and is likely a critical part of the low GC spiking observed in experiment[119, 141]. It also plays an important role in increasing the MC spike participation in the simulations here (Fig. 3.7). Tonic inhibition does not do anything to help generate gamma oscillations in this model, but it does seem to facilitate synchrony in the 12 Hz range (see Fig. 3.9 and Fig. 3.10(a), $g_{tonic} = 1.8$ nS heat maps). The tonic inhibition implemented here is simply a perpetually open channel, essentially a leak current; other experiments have suggested that feedforward inhibition to GCs via short axon cells could be important to GC activity patterns[142] and that tonic inhibition may be unlikely[143]. More sophisticated implementation of inhibition to the GCs

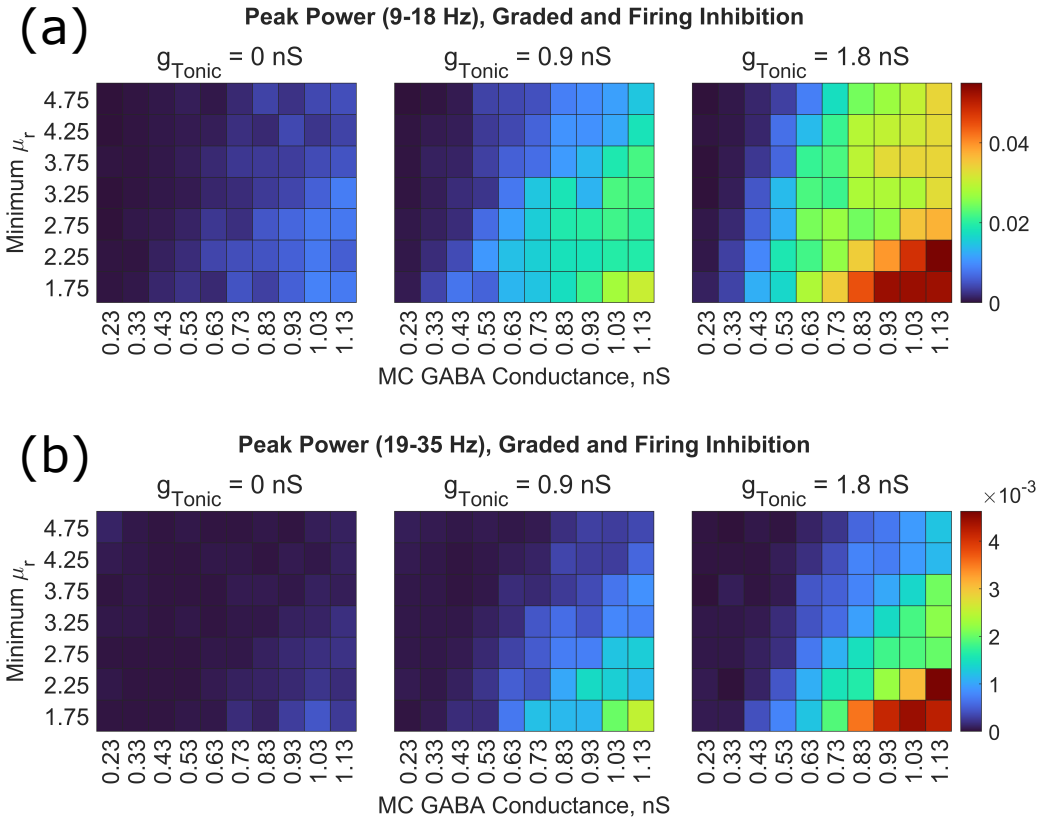

Figure 3.11: **Power for 9-18 Hz and 19-35 Hz Spectral Peaks with Graded and Firing Inhibition, Tonic Inhibition Dependence.** (a) Peak power for the 9-18 Hz peak in the power spectrum for varying levels of tonic GC inhibition. (b) Peak power for the 19-35 Hz peak in the power spectrum for varying levels of tonic GC inhibition.

may be more conducive to gamma generation.

Implementing graded inhibition to the MCs (even combined with typical spike-mediated inhibition) results in greater MC participation with few silent MCs, as observed in experiment[121, 140]. Because graded inhibition here follows the NMDA current at the synapse, it requires simultaneously a sufficiently excited GC as well as recent firing activity from the receiving MC. This naturally makes that portion of the MC inhibition activity-dependent, similar to [62]. Lending further support to this method of graded inhibition, another study[20] found that activation of NMDA channels was a requirement

for GABA release from GC dendritic spines, potentially even in the case of GC somatic spikes. However, localized GABA release also required spine spikes and high voltage activated calcium channels[20]. Instead of explicitly simulating spine spikes and calcium concentration, this could be addressed by making GABA release dependent on NMDA current in a more nuanced way than simply being directly proportional. In light of the low levels of GC somatic spikes observed in experiment[119], the specific form of graded inhibition is likely to be important to gamma oscillations. Low GC firing could also suggest the involvement of other types of inhibitory neurons[15], although regardless of the inhibitory cells involved, NMDA channels play an essential role[27].

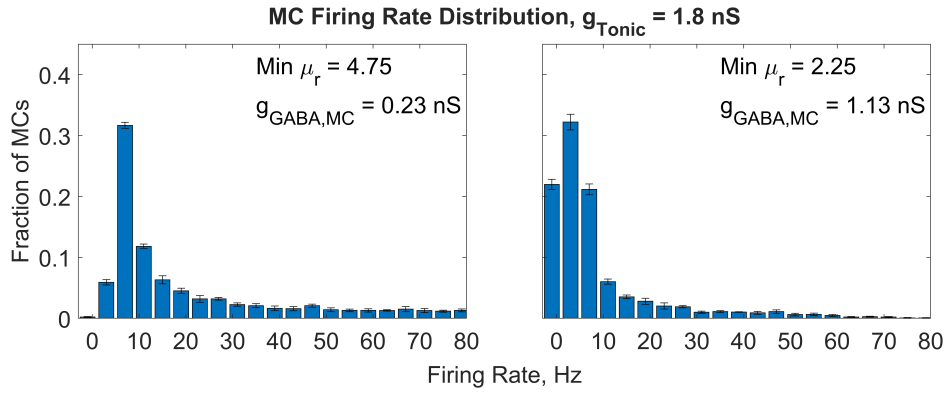

Figure 3.12: **Distribution of MC Firing Rates, Graded and Firing Inhibition.** Distribution of MC firing rates for the trial resulting in the greatest MC participation (left) and for the trial resulting in the largest oscillatory peak (right).

However, none of the simulations using graded inhibition yield gamma-dominant oscillatory activity in this work. Instead, the dominant frequency is in the high theta-low beta range. The mechanism precipitating these oscillations is most effective with high MC GABA conductances and low MC firing rates, i.e., with strong inhibition (see Fig. 3.9(a) and Fig. 3.7(a), lower right). Experimentally recorded gamma oscillations in the OB display higher MC firing rates and MC participation[27], suggesting a parameter region with weaker

inhibition, and so thus is likely achieved by a different mechanism.

One mechanism for gamma generation in the OB explored by [52, 53, 55] uses weak inhibition to synchronize rhythmic MC spikes (entrainment). This idea is supported by experimental findings that average MC firing rhythms align well with the dominant gamma frequency[27, 52], especially during epochs of gamma oscillatory activity[16]. Graded inhibition could be a viable candidate for mediating this weak inhibition. In order to fully implement gamma oscillations via entrainment in this model, however, both the MC model and the network connectivity would likely need adjusting.

MC rhythmicity can be achieved with adjustment of the Izhikevich framework[129], including the addition of sub-threshold oscillations[122] as observed in experiment[24, 144, 145] and included in some computational OB models (e.g., [54, 55, 95]). The distribution of MC firing in the model would also need regulating. The spread of MC firing rates in [27] is from just under 10 Hz to about 45 Hz, and the model here yields a range much larger than that, both in the case of the strongest oscillations (Fig. 3.12, right) and in the case of highest MC participation (Fig. 3.12, left). Introduction of Hebbian-like rules to the network connectivity could be used to update the network, adding GC-MC synapses to overactive MCs and removing synapses from inactive MCs. Recent findings regarding the resonant properties of excitatory tufted cells in the OB may suggest their inclusion in future modeling efforts as well[16].

The present work shows how graded MC inhibition based on GC NMDA current can be implemented and naturally leads to activity-dependent MC inhibition, which is enhanced by simple tonic GC inhibition. While gamma oscillations do not also appear, these techniques can help lead to a more realistic model of OB gamma oscillatory activity.

Chapter 4

Toward Reproducing Perturbations in Olfactory Bulb Gamma Oscillations

4.1 Oscillation Mechanisms

In the previous chapter, future work generating gamma oscillations via entrainment[52, 55] with physiologically relevant levels of MC spiking[62, 140] and GC spiking[119] using graded inhibition is discussed. But could such a mechanism be consistent with increased gamma power and decreased gamma frequency resulting from reduced GABA conductance, as found by Lepousez and Lledo[27], and are there other mechanisms that could work?

An important consideration in answering this question is the specific effect GABA antagonist had on the shape of inhibition received by the MCs. An intermediate level of GABA antagonist (the levels that resulted in increased gamma power and decreased gamma frequency) did not significantly change the amplitude of the inhibition; instead it lengthened the time scale of inhibition, with a slower rise and decay[27] (see Fig. 4.1). Lepousez and Lledo postulated that while reduced GABA conductance weakens individual inhibitory events, more inhibitory events occur, leading to a similar level of inhibition as before the

GABA antagonist[27]. Their theory, along with suggestions for implementation in a computational model, is discussed further in the next section.

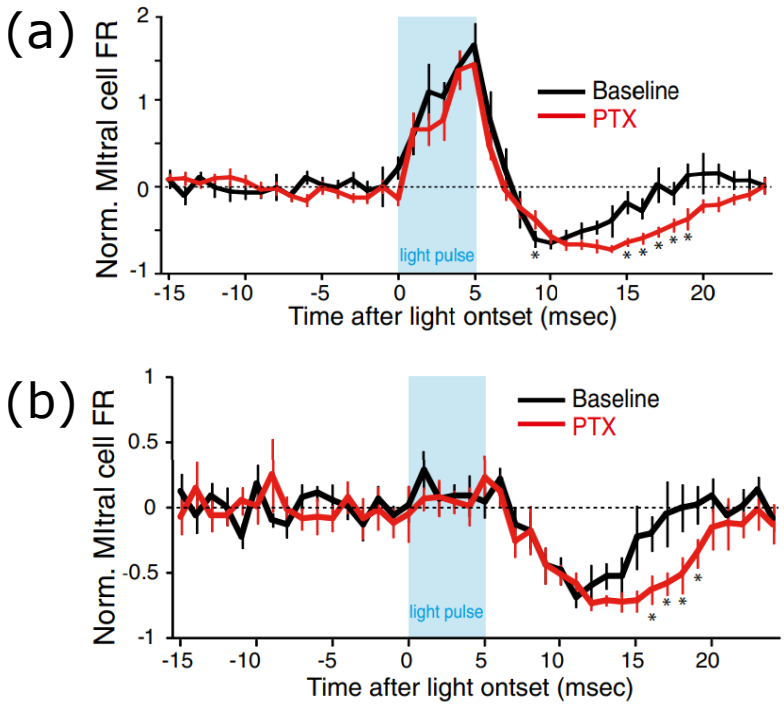

Figure 4.1: **Moderately Reduced GABA Conductance Lengthens Timescale of Mitral Cell Inhibition.** Figure reproduced from [27] (Figure 6F and 6H). (a) Peristimulus plot for optogenetically stimulated MCs, with GABA antagonist pictrotoxin (PTX, red) and without (black), showing the lengthened timescale of inhibition as measured by the change in normalized firing rate. (b) Same as (a), but for MCs that were not directly stimulated by the light pulse. Experiment performed on mouse olfactory bulbs[27].

The entrainment mechanism relies on synchronization of intrinsically rhythmic MC firing[16, 52, 53, 55]. MC spike autocorrelograms from Lepousez and Lledo support this idea with average peak lag time in autocorrelograms corresponding well to the dominant gamma frequency. With application of GABA antagonist, the downward shift in gamma frequency was consistent with the shift in peak lag time, implying that the change in gamma frequency may result from a change in MC autorhythmicity[27]. The OB gamma entrainment

mechanism as presented by David et al. in its most recent iteration[55], though, does not result in a similar change in gamma oscillatory activity. In their model, neither reducing the inhibitory weight nor increasing the GABA time constant had much effect on the frequency or power of gamma oscillations. The frequency instead was dependent on the average MC firing rate and intrinsic MC resonance properties, which did not depend on inhibition[55]. However, Lepousez and Lledo found that GABA antagonist did modulate MC resonance, decreasing the frequency of its natural firing rhythm[27]. Therefore, while the specific form of the entrainment mechanism in [55] is inconsistent, a MC model with resonance that had some dependence on inhibition could work. Additionally, in another implementation of an entrainment mechanism for OB gamma[53], Galán et al. use correlated inhibitory Poisson noise to synchronize rhythmic MC firing, and when the time scale of those inhibitory events was lengthened, the frequency of the power spectrum peak decreased. Therefore, there is evidence for reduced gamma frequency with the kind of inhibition modulation in [27], potentially with an increase in power if it also results in a greater portion of the MCs developing an intrinsic rhythm in the lower gamma range [52].

Another mechanism used as the basis for a number of OB models[51, 54, 95], pyramidal interneuron gamma (PING), could be a possibility. In PING, inhibition gates the firing of the excitatory population[50]. Excitatory neurons only fire once inhibition is sufficiently reduced, which then induces high levels of inhibition again. Therefore, the oscillation frequency is set by the amplitude and timescale of the inhibition[50]. So with decreased inhibitory weight, the time between allowed firing events is also decreased, increasing the oscillation frequency (see Fig. 4.2, from [51]). However, the observed effect of GABA antagonist was an increased inhibitory timescale[27], which would decrease the frequency in a PING framework. If MC resonance were included in the model, and the lower network-imposed frequency was more closely aligned with the MC resonant frequency, it could also lead to increased gamma power.

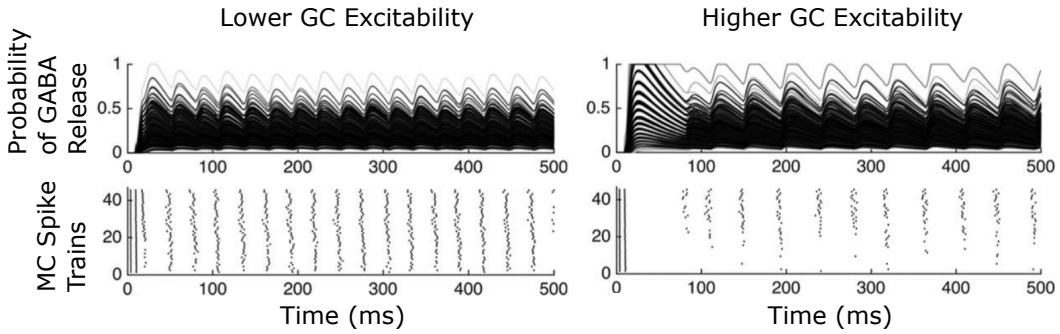

Figure 4.2: **Effect of Inhibition on PING Oscillation Frequency.** Figure adapted from [51] (Figure 4Aii and 4Aiii). Probability of GABA release (top) and MC spike trains (bottom), showing that in a PING mechanism, greater inhibition (higher GC excitability, right) increases the time between synchronized MC firing events, leading to reduced oscillation frequency. See [51] for model details.

Although there are potential routes to reproducing the Lepousez and Lledo findings in both mechanisms, recent work[16] has pointed to entrainment of resonant neurons as the more likely candidate. Burton and Urban found that even during gamma oscillatory activity, the inhibitory currents did not follow the gamma rhythm[16], an argument against a PING mechanism. They did find rhythmic firing, but the synchronicity and resonance was stronger in tufted cells (TCs) than in MCs, suggesting that TCs may be important to gamma generation[16].

As proposed in Chapter 3, the resonant properties of both MCs and TCs could be described with adjustments to the Izhikevich equations used in [45]. Whether graded inhibition would be sufficient to synchronize them requires testing. However, graded inhibition fits neatly into the theory Lepousez and Lledo presented for how reduced inhibitory conductance increases MC synchrony and gamma power, as discussed in Section 4.3.

4.2 Inhibition-Dependent Propagation of Dendrodendritic Synaptic Activation

MC-GC interactions occur via dendrodendritic synapses. Action potentials in MCs backpropagate down lateral dendrites, releasing glutamate at MC-GC synapses along the length of the dendrites[63, 146, 147]. Based on findings that inhibition can block backpropagation of MC action potentials[63], Lepousez and Lledo presented a theory for why moderate levels of GABA antagonist increased gamma power and did not decrease the level of inhibition received by the MCs. They hypothesized that reduced GABA conductance at individual dendrodendritic synapses along MC lateral dendrites allows action potentials to travel further, exciting more GCs and increasing the extent of lateral inhibition[27]. So while each individual inhibitory event is smaller, there are more of them, resulting in a similar level of inhibition but with greater connectivity, potentially leading to increased synchronization of MC firing and gamma power.

Though not explicitly discussed in [27], this theory also suggests a possible explanation for the longer timescale of inhibition, which may underlie the slower MC autorhythmicity and reduced gamma frequency. The period of rhythmic MC firing increased by about 2.5 ms, and the inhibition rise and decay times increased by 2.2 ms and 2.8 ms respectively[27]. Depending on how much further action potentials are able to spread, the time it takes to travel that extra distance could provide an explanation. Studies have measured MC backpropagating action potential conduction velocities between 200 to 440 µm/ms[63, 147]. A time of 2 - 3 ms is an extra 400 - 1320 µm of distance; with MC lateral dendritic lengths up to and potentially exceeding 1000 µm[128], the extra propagation time could plausibly be tied to the lengthened timescale of inhibition, particularly in the lower range of conduction velocities.

4.3 Suggestions for Implementation

Implementing inhibition-dependent propagation of action potentials in a model requires tracking the location of each synapse, something for which the model discussed in Chapter 3 is well-equipped. If a threshold level of cumulative inhibition along a given direction is reached, more distant synapses are not activated. To facilitate this, the area representing the span of MC secondary dendrites could be divided up into sectors, such that inhibition is accumulated along each sector independently (see Fig.4.3).

Graded inhibition is important because the inhibitory events are not fast enough to be evoked by the same action potential they are blocking[63]. In other words, the inhibition needs to already be there. If GABA release only occurred after a GC spike, then blocking propagation would require precise spike timing between MCs and GCs. Because graded inhibition as implemented in Chapter 3 follows the GC NMDA current, it is independent of GC spiking and has a longer timescale[22]. Therefore it is more likely to overlap with MC spikes, facilitating inhibition-dependent propagation.

Conduction velocity could be modeled by activating synapses on a delay based on distance from the spiking MC. For example, if the simulated time step is 0.1 ms and the presumed conduction velocity is 300 µm/ms, only synapses within 30 µm from the MC would be activated on the time step that it spiked. The next time step would activate synapses within the next 30 µm, etc., with the cumulative inhibition being checked for each direction after each time step. This is similar to hard-coded delays implemented in some models of the OB, such as [55].

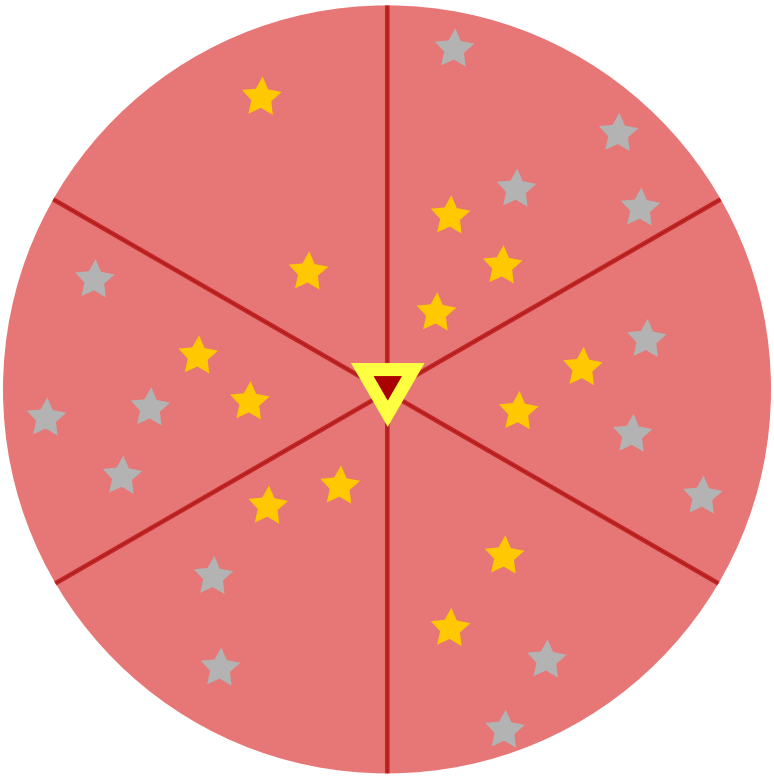

Figure 4.3: **Illustration of Inhibition-Dependent Propagation of Synaptic Activation.** Diagram of an example MC dendritic area, divided into six sectors. Activated synapses: Yellow-orange. Unactivated synapses: Gray. For a MC that has spiked (yellow-outlined triangle), if the cumulative inhibition received at closer synapses reaches a threshold level, more distant synapses in that direction are not activated. Functionally, this means the GCs at those synapses are not excited by the MC spike. Synapses that are more distant but in a different direction can still be activated (e.g., in the top-left sector). Graded inhibition means that propagation could be blocked with fewer synapses in one direction than another. If inhibitory conductance is reduced, it will take more activated synapses to reach the threshold and block further propagation.

4.4 Conclusion

It should be noted that the model in Chapter 3 is not the only model that could serve as a foundation for testing these ideas. For example, using a compartment model of MCs (like in [54]) could very naturally be used for simulating conduction velocities. However, the physiologically-inspired network generation process developed in [45] provides an appealing

framework for the network connectivity and spatial layout of the model. Along with its use of the Izhekevich equations[45, 122] allowing for the simulation of a large population of neurons and the ability to easily incorporate NMDA-based graded inhibition[20] (Chapter 3), the modified model presented here could be a powerful foundation for future work.

While implementation of these ideas would require a great deal of optimization, they represent a clear path toward testing Lepousez and Lledo's theory for the mechanism behind increased gamma power and decreased gamma frequency with a moderate reduction of GABA conductance[27]. Further understanding of the generation and modulation of gamma oscillations in the OB could lead to greater insight into how neural activity is impacted by disease pathology[6, 7, 59] and potentially to development of tools for earlier detection of disease.

Bibliography

[1] X. J. Wang, H. Hu, C. Huang, H. Kennedy, C. T. Li, N. Logothetis, Z. L. Lu, Q. Luo, M. M. Poo, D. Tsao, S. Wu, Z. Wu, X. Zhang, and D. Zhou. Computational neuroscience: a frontier of the 21. *Natl Sci Rev*, 7(9):1418–1422, 2020. ISSN 2053-714X. doi: 10.1093/nsr/nwaa129. URL `https://www.ncbi.nlm.nih.gov/pubmed/34691537`.

[2] Ahmed Moustafa. Computational models of brain and behavior, 2017.

[3] Johannes Attems, Lauren Walker, and Kurt A. Jellinger. Olfactory bulb involvement in neurodegenerative diseases. *Acta Neuropathologica*, 127(4):459–475, 2014. ISSN 1432-0533. doi: 10.1007/s00401-014-1261-7. URL `https://doi.org/10.1007/s00401-014-1261-7`.

[4] I. Ubeda-Bañon, D. Saiz-Sanchez, A. Flores-Cuadrado, E. Rioja-Corroto, M. Gonzalez-Rodriguez, S. Villar-Conde, V. Astillero-Lopez, J. P. Cabello-de la Rosa, M. J. Gallardo-Alcañiz, J. Vaamonde-Gamo, F. Relea-Calatayud, L. Gonzalez-Lopez, A. Mohedano-Moriano, A. Rabano, and A. Martinez-Marcos. The human olfactory system in two proteinopathies: Alzheimer's and parkinson's diseases. *Transl Neurodegener*, 9(1):22, 2020. ISSN 2047-9158. doi: 10.1186/s40035-020-00200-7. URL `https://www.ncbi.nlm.nih.gov/pubmed/32493457`.

[5] R. L. Doty. Olfactory dysfunction in neurodegenerative diseases: is there a common pathological substrate? *Lancet Neurol*, 16(6):478–488, 2017. ISSN 1474-4465. doi: 10.1016/S1474-4422(17)30123-0. URL `https://www.ncbi.nlm.nih.gov/pubmed/28504111`.

[6] Ming Chen, Yunan Chen, Qingwei Huo, Lei Wang, Shuyi Tan, Afzal Misrani, Jinxiang Jiang, Jian Chen, Shiyuan Chen, Jiawei Zhang, Sidra Tabassum, Jichen Wang, Xi Chen, Cheng Long, and Li Yang. Enhancing gabaergic signaling ameliorates aberrant gamma oscillations of olfactory bulb in ad mouse models. *Molecular neurodegeneration*, 16(1):14–14, 2021. ISSN 1750-1326. doi: 10.1186/s13024-021-00434-7. URL `https://www.ncbi.nlm.nih.gov/pmc/articles/PMC7934466/`.

[7] Weiyun Li, Shanshan Li, Lianghua Shen, Junbo Wang, Xuewei Wu, Jing Li, Chunlong Tu, Xuesong Ye, and Shucai Ling. Impairment of dendrodendritic inhibition in the ol-

factory bulb of app/ps1 mice. *Frontiers in Aging Neuroscience*, 11:2, 2019. ISSN 1663-4365. URL https://www.frontiersin.org/article/10.3389/fnagi.2019.00002.

[8] Shanshan Li, Weiyun Li, Xuewei Wu, Jing Li, Jing Yang, Chunlong Tu, Xuesong Ye, and Shucai Ling. Olfactory deficit is associated with mitral cell dysfunction in the olfactory bulb of p301s tau transgenic mice. *Brain Research Bulletin*, 148:34–45, 2019. ISSN 0361-9230. doi: https://doi.org/10.1016/j.brainresbull.2019.03.006. URL https://www.sciencedirect.com/science/article/pii/S0361923018309924.

[9] Aishwarya S. Kulkarni, Maria Del Mar Cortijo, Elizabeth R. Roberts, Tamara L. Suggs, Heather B. Stover, José I. Pena-Bravo, Jennifer A. Steiner, Kelvin C. Luk, Patrik Brundin, and Daniel W. Wesson. Perturbation of in vivo neural activity following α-synuclein seeding in the olfactory bulb. *Journal of Parkinson's disease*, 10(4):1411–1427, 2020. ISSN 1877-718X 1877-7171. doi: 10.3233/JPD-202241. URL https://www.ncbi.nlm.nih.gov/pmc/articles/PMC8018612/.

[10] Shin Nagayama, Ryota Homma, and Fumiaki Imamura. Neuronal organization of olfactory bulb circuits. *Frontiers in Neural Circuits*, 8, 2014. ISSN 1662-5110. doi: 10.3389/fncir.2014.00098. URL https://www.frontiersin.org/articles/10.3389/fncir.2014.00098.

[11] Gordon M Shepherd, WR Chen, and CA Greer. Olfactory bulb. *Sensory Systems II*, page 66, 2004.

[12] Gordon M. Shepherd. *The synaptic organization of the brain*. Oxford University Press, Oxford ; New York, 5th edition, 2004. ISBN 0195159551 (alk. paper) 019515956X (pbk. alk. paper). URL Tableofcontentsonlyhttp://www.loc.gov/catdir/toc/fy043/2003042914.html.

[13] J. S. Isaacson and B. W. Strowbridge. Olfactory reciprocal synapses: dendritic signaling in the cns. *Neuron*, 20(4):749–61, 1998. ISSN 0896-6273. doi: 10.1016/s0896-6273(00)81013-2. URL https://www.ncbi.nlm.nih.gov/pubmed/9581766.

[14] Samuel Lagier, Alan Carleton, and Pierre-Marie Lledo. Interplay between local gabaergic interneurons and relay neurons generates γ oscillations in the rat olfactory bulb. *The Journal of Neuroscience*, 24(18):4382, 2004. doi: 10.1523/JNEUROSCI.5570-03.2004. URL http://www.jneurosci.org/content/24/18/4382.abstract.

[15] S. D. Burton. Inhibitory circuits of the mammalian main olfactory bulb. *J Neurophysiol*, 118(4):2034–2051, 2017. ISSN 1522-1598. doi: 10.1152/jn.00109.2017. URL https://www.ncbi.nlm.nih.gov/pubmed/28724776.

[16] S. D. Burton and N. N. Urban. Cell and circuit origins of fast network oscillations in the mammalian main olfactory bulb. *Elife*, 10, 2021. ISSN 2050-084X. doi: 10.7554/eLife.74213. URL https://www.ncbi.nlm.nih.gov/pubmed/34658333.

[17] Randall C. O'Reilly, Yuko Munakata, Michael J. Frank, Thomas E. Hazy, and Contributors. *Computational Cognitive Neuroscience*. Online Book, 4th Edition, URL: https://CompCogNeuro.org, 2012. URL https://github.com/CompCogNeuro/ed4.

[18] M. C. Angulo, J. Rossier, and E. Audinat. Postsynaptic glutamate receptors and integrative properties of fast-spiking interneurons in the rat neocortex. *J Neurophysiol*, 82(3):1295–302, 1999. ISSN 0022-3077. doi: 10.1152/jn.1999.82.3.1295. URL https://www.ncbi.nlm.nih.gov/pubmed/10482748.

[19] A. M. Thomson. Activity-dependent properties of synaptic transmission at two classes of connections made by rat neocortical pyramidal axons in vitro. *J Physiol*, 502 (Pt 1)(Pt 1):131–47, 1997. ISSN 0022-3751. doi: 10.1111/j.1469-7793.1997.131bl.x. URL https://www.ncbi.nlm.nih.gov/pubmed/9234202.

[20] V. Lage-Rupprecht, L. Zhou, G. Bianchini, S. S. Aghvami, M. Mueller, B. Rózsa, M. Sassoè-Pognetto, and V. Egger. Presynaptic nmdars cooperate with local spikes toward gaba release from the reciprocal olfactory bulb granule cell spine. *Elife*, 9, 2020. ISSN 2050-084X. doi: 10.7554/eLife.63737. URL https://www.ncbi.nlm.nih.gov/pubmed/33252329.

[21] N. E. Schoppa, J. M. Kinzie, Y. Sahara, T. P. Segerson, and G. L. Westbrook. Dendrodendritic inhibition in the olfactory bulb is driven by nmda receptors. *The Journal of neuroscience : the official journal of the Society for Neuroscience*, 18(17):6790–6802, 1998. ISSN 0270-6474 1529-2401. doi: 10.1523/JNEUROSCI.18-17-06790.1998. URL https://www.ncbi.nlm.nih.gov/pmc/articles/PMC6792983/.

[22] J. S. Isaacson. Mechanisms governing dendritic gamma-aminobutyric acid (gaba) release in the rat olfactory bulb. *Proc Natl Acad Sci U S A*, 98(1):337–42, 2001. ISSN 0027-8424. doi: 10.1073/pnas.98.1.337. URL https://www.ncbi.nlm.nih.gov/pubmed/11120892.

[23] Samuel Lagier, Patrizia Panzanelli, Raúl E Russo, Antoine Nissant, Brice Bathellier, Marco Sassoè-Pognetto, Jean-Marc Fritschy, and Pierre-Marie Lledo. Gabaergic inhibition at dendrodendritic synapses tunes γ oscillations in the olfactory bulb. *Proceedings of the National Academy of Sciences*, 104(17):7259–7264, 2007.

[24] N. Fourcaud-Trocmé, V. Briffaud, M. Thévenet, N. Buonviso, and C. Amat. In vivo beta and gamma subthreshold oscillations in rat mitral cells: origin and gating by respiratory dynamics. *J Neurophysiol*, 119(1):274–289, 2018. ISSN 1522-1598. doi: 10.1152/jn.00053.2017. URL https://www.ncbi.nlm.nih.gov/pubmed/29021388.

[25] Jennifer Beshel, Nancy Kopell, and Leslie M Kay. Olfactory bulb gamma oscillations are enhanced with task demands. *Journal of Neuroscience*, 27(31):8358–8365, 2007.

[26] Leslie M. Kay, Jennifer Beshel, Jorge Brea, Claire Martin, Daniel Rojas-Líbano, and Nancy Kopell. Olfactory oscillations: the what, how and what for. *Trends in neurosciences*, 32(4):207–214, 2009. ISSN 0166-2236 1878-108X. doi: 10.1016/j.tins.2008.11.008. URL https://www.ncbi.nlm.nih.gov/pmc/articles/PMC3389991/.

[27] Gabriel Lepousez and Pierre-Marie Lledo. Odor discrimination requires proper olfactory fast oscillations in awake mice. *Neuron*, 80(4):1010–1024, 2013. ISSN 0896-6273. doi: 10.1016/j.neuron.2013.07.025. URL https://doi.org/10.1016/j.neuron.2013.07.025.

[28] Behzad Iravani, Artin Arshamian, Mikael Lundqvist, Leslie M. Kay, Donald A. Wilson, and Johan N. Lundström. Odor identity can be extracted from the reciprocal connectivity between olfactory bulb and piriform cortex in humans. *NeuroImage*, 237:118130, 2021. ISSN 1053-8119. doi: https://doi.org/10.1016/j.neuroimage.2021.118130. URL https://www.sciencedirect.com/science/article/pii/S1053811921004079.

[29] Kevin R. Neville and Lewis B. Haberly. Beta and gamma oscillations in the olfactory system of the urethane-anesthetized rat. *Journal of Neurophysiology*, 90(6):3921–3930, 2003. ISSN 0022-3077. doi: 10.1152/jn.00475.2003. URL https://doi.org/10.1152/jn.00475.2003.

[30] R. Gervais, N. Buonviso, C. Martin, and N. Ravel. What do electrophysiological studies tell us about processing at the olfactory bulb level? *J Physiol Paris*, 101(1-3):40–5, 2007. ISSN 0928-4257. doi: 10.1016/j.jphysparis.2007.10.006. URL https://www.ncbi.nlm.nih.gov/pubmed/18054211.

[31] C. Martin, J. Beshel, and L. M. Kay. An olfacto-hippocampal network is dynamically involved in odor-discrimination learning. *J Neurophysiol*, 98(4):2196–205, 2007. ISSN 0022-3077. doi: 10.1152/jn.00524.2007. URL https://www.ncbi.nlm.nih.gov/pubmed/17699692.

[32] C. A. Lowry and L. M. Kay. Chemical factors determine olfactory system beta oscillations in waking rats. *J Neurophysiol*, 98(1):394–404, 2007. ISSN 0022-3077. doi: 10.1152/jn.00124.2007. URL https://www.ncbi.nlm.nih.gov/pubmed/17442770.

[33] L. M. Kay. Olfactory system oscillations across phyla. *Curr Opin Neurobiol*, 31:141–7, 2015. ISSN 1873-6882. doi: 10.1016/j.conb.2014.10.004. URL https://www.ncbi.nlm.nih.gov/pubmed/25460070.

[34] Kovács, Cairns, and Lantos. β-amyloid deposition and neurofibrillary tangle formation in the olfactory bulb in ageing and alzheimer's disease. *Neuropathology and*

Applied Neurobiology, 25(6):481–491, 1999. ISSN 0305-1846. doi: https://doi.org/10.1046/j.1365-2990.1999.00208.x. URL https://doi.org/10.1046/j.1365-2990.1999.00208.x.

[35] Tibor Kovács, Nigel J. Cairns, and Peter L. Lantos. Olfactory centres in alzheimer's disease: olfactory bulb is involved in early braak's stages. *NeuroReport*, 12(2), 2001. ISSN 0959-4965. URL https://journals.lww.com/neuroreport/Fulltext/2001/02120/Olfactory_centres_in_Alzheimer_s_disease_.21.aspx.

[36] J. Attems and K. A. Jellinger. Olfactory tau pathology in alzheimer disease and mild cognitive impairment. *Clin Neuropathol*, 25(6):265–71, 2006. ISSN 0722-5091 (Print) 0722-5091.

[37] Richard L. Doty. Olfactory dysfunction in parkinson disease. *Nature Reviews Neurology*, 8(6):329–339, 2012. ISSN 1759-4766. doi: 10.1038/nrneurol.2012.80. URL https://doi.org/10.1038/nrneurol.2012.80.

[38] Renpei Sengoku, Yuko Saito, Masako Ikemura, Hiroyuki Hatsuta, Yoshio Sakiyama, Kazutomi Kanemaru, Tomio Arai, Motoji Sawabe, Noriko Tanaka, Hideki Mochizuki, Kiyoharu Inoue, and Shigeo Murayama. Incidence and extent of lewy body-related α-synucleinopathy in aging human olfactory bulb. *Journal of Neuropathology & Experimental Neurology*, 67(11):1072–1083, 2008. ISSN 0022-3069. doi: 10.1097/NEN.0b013e31818b4126. URL https://doi.org/10.1097/NEN.0b013e31818b4126.

[39] Heiko Braak, Kelly Del Tredici, Udo Rüb, Rob A. I. de Vos, Ernst N. H. Jansen Steur, and Eva Braak. Staging of brain pathology related to sporadic parkinson's disease. *Neurobiology of Aging*, 24(2):197–211, 2003. ISSN 0197-4580. doi: https://doi.org/10.1016/S0197-4580(02)00065-9. URL http://www.sciencedirect.com/science/article/pii/S0197458002000659.

[40] Heiko Braak, Estifanos Ghebremedhin, Udo Rüb, Hansjürgen Bratzke, and Kelly Del Tredici. Stages in the development of parkinson's disease-related pathology. *Cell and Tissue Research*, 318(1):121–134, 2004. ISSN 1432-0878. doi: 10.1007/s00441-004-0956-9. URL https://doi.org/10.1007/s00441-004-0956-9.

[41] B. Iravani, A. Arshamian, M. Schaefer, P. Svenningsson, and J. N. Lundström. A non-invasive olfactory bulb measure dissociates parkinson's patients from healthy controls and discloses disease duration. *NPJ Parkinsons Dis*, 7(1):75, 2021. ISSN 2373-8057. doi: 10.1038/s41531-021-00220-8. URL https://www.ncbi.nlm.nih.gov/pubmed/34408159.

[42] Christiane Linster. Computation in the olfactory system. *Computational Models of Brain and Behavior*, pages 185–198, 2017. ISSN 9781119159193. doi: doi:10.1002/

9781119159193.ch1410.1002/9781119159193.ch14. URL https://doi.org/10.1002/9781119159193.ch14.

[43] D. Zavitz, I. A. Youngstrom, A. Borisyuk, and M. Wachowiak. Effect of interglomerular inhibitory networks on olfactory bulb odor representations. *J Neurosci*, 2020. ISSN 1529-2401. doi: 10.1523/JNEUROSCI.0233-20.2020. URL https://www.ncbi.nlm.nih.gov/pubmed/32561671.

[44] F. Cavarretta, S. D. Burton, K. M. Igarashi, G. M. Shepherd, M. L. Hines, and M. Migliore. Parallel odor processing by mitral and middle tufted cells in the olfactory bulb. *Sci Rep*, 8(1):7625, 2018. ISSN 2045-2322. doi: 10.1038/s41598-018-25740-x. URL https://www.ncbi.nlm.nih.gov/pubmed/29769664.

[45] D. E. C. Kersen, G. Tavoni, and V. Balasubramanian. Connectivity and dynamics in the olfactory bulb. *PLoS Comput Biol*, 18(2):e1009856, 2022. ISSN 1553-7358. doi: 10.1371/journal.pcbi.1009856. URL https://www.ncbi.nlm.nih.gov/pubmed/35130267.

[46] W. Adams, J. N. Graham, X. Han, and H. Riecke. Top-down inputs drive neuronal network rewiring and context-enhanced sensory processing in olfaction. *PLoS Comput Biol*, 15(1):e1006611, 2019. ISSN 1553-7358. doi: 10.1371/journal.pcbi.1006611. URL https://www.ncbi.nlm.nih.gov/pubmed/30668563.

[47] Daniel R. Kepple, Hamza Giaffar, Dmitry Rinberg, and Alexei A. Koulakov. Deconstructing odorant identity via primacy in dual networks. *Neural Computation*, 31(4):710–737, 2019. ISSN 0899-7667. doi: 10.1162/neco_a_01175. URL https://doi.org/10.1162/neco_a_01175.

[48] T. A. Cleland and A. Borthakur. A systematic framework for olfactory bulb signal transformations. *Front Comput Neurosci*, 14:579143, 2020. ISSN 1662-5188. doi: 10.3389/fncom.2020.579143. URL https://www.ncbi.nlm.nih.gov/pubmed/33071767.

[49] Nabil Imam and Thomas A. Cleland. Rapid online learning and robust recall in a neuromorphic olfactory circuit. *Nature Machine Intelligence*, 2(3):181–191, 2020. ISSN 2522-5839. doi: 10.1038/s42256-020-0159-4. URL https://doi.org/10.1038/s42256-020-0159-4.

[50] M. A. Whittington, R. D. Traub, N. Kopell, B. Ermentrout, and E. H. Buhl. Inhibition-based rhythms: experimental and mathematical observations on network dynamics. *Int J Psychophysiol*, 38(3):315–36, 2000. ISSN 0167-8760. doi: 10.1016/s0167-8760(00)00173-2. URL https://www.ncbi.nlm.nih.gov/pubmed/11102670.

[51] B. L. Osinski and L. M. Kay. Granule cell excitability regulates gamma and beta oscillations in a model of the olfactory bulb dendrodendritic microcircuit. *J Neurophysiol*, 116(2):522–39, 2016. ISSN 1522-1598. doi: 10.1152/jn.00988.2015. URL https://www.ncbi.nlm.nih.gov/pubmed/27121582.

[52] F. O. David, E. Hugues, T. Cenier, N. Fourcaud-Trocmé, and N. Buonviso. Specific entrainment of mitral cells during gamma oscillation in the rat olfactory bulb. *PLoS Comput Biol*, 5(10):e1000551, 2009. ISSN 1553-7358. doi: 10.1371/journal.pcbi.1000551. URL https://www.ncbi.nlm.nih.gov/pubmed/19876377.

[53] R. F. Galán, N. Fourcaud-Trocmé, G. B. Ermentrout, and N. N. Urban. Correlation-induced synchronization of oscillations in olfactory bulb neurons. *J Neurosci*, 26 (14):3646–55, 2006. ISSN 1529-2401. doi: 10.1523/JNEUROSCI.4605-05.2006. URL https://www.ncbi.nlm.nih.gov/pubmed/16597718.

[54] G. Li and T. A. Cleland. A coupled-oscillator model of olfactory bulb gamma oscillations. *PLoS Comput Biol*, 13(11):e1005760, 2017. ISSN 1553-734X (Print) 1553-734x. doi: 10.1371/journal.pcbi.1005760.

[55] F. David, E. Courtiol, N. Buonviso, and N. Fourcaud-Trocmé. Competing mechanisms of gamma and beta oscillations in the olfactory bulb based on multimodal inhibition of mitral cells over a respiratory cycle. *eNeuro*, 2(6), 2015. ISSN 2373-2822. doi: 10.1523/ENEURO.0018-15.2015. URL https://www.ncbi.nlm.nih.gov/pubmed/26665163.

[56] Z. Li and J. J. Hopfield. Modeling the olfactory bulb and its neural oscillatory processings. *Biol Cybern*, 61(5):379–92, 1989. ISSN 0340-1200. doi: 10.1007/BF00200803. URL https://www.ncbi.nlm.nih.gov/pubmed/2551392.

[57] Martí Colom-Cadena, Tara Spires-Jones, Henrik Zetterberg, Kaj Blennow, Anthony Caggiano, Steven T. DeKosky, Howard Fillit, John E. Harrison, Lon S. Schneider, Phillip Scheltens, Willem de Haan, Michael Grundman, Christopher H. van Dyck, Nicholas J. Izzo, Susan M. Catalano, and Group the Synaptic Health Endpoints Working. The clinical promise of biomarkers of synapse damage or loss in alzheimer's disease. *Alzheimer's Research & Therapy*, 12(1):21, 2020. ISSN 1758-9193. doi: 10.1186/s13195-020-00588-4. URL https://doi.org/10.1186/s13195-020-00588-4.

[58] Laura Calo, Michal Wegrzynowicz, Jessica Santivañez-Perez, and Maria Grazia Spillantini. Synaptic failure and α-synuclein. *Movement Disorders*, 31(2):169–177, 2016. ISSN 0885-3185. doi: 10.1002/mds.26479. URL https://doi.org/10.1002/mds.26479.

[59] A. S. Kulkarni, M. R. Burns, P. Brundin, and D. W. Wesson. Linking α-synuclein-induced synaptopathy and neural network dysfunction in early parkinson's disease. *Brain Commun*, 4(4):fcac165, 2022. ISSN 2632-1297. doi: 10.1093/braincomms/fcac165. URL https://www.ncbi.nlm.nih.gov/pubmed/35822101.

[60] B. L. Osinski, A. Kim, W. Xiao, N. M. Mehta, and L. M. Kay. Pharmacological manipulation of the olfactory bulb modulates beta oscillations: testing model predictions. *J Neurophysiol*, 120(3):1090–1106, 2018. ISSN 1522-1598. doi: 10.1152/jn.00090.2018. URL https://www.ncbi.nlm.nih.gov/pubmed/29847235.

[61] J. Cang and J. S. Isaacson. In vivo whole-cell recording of odor-evoked synaptic transmission in the rat olfactory bulb. *J Neurosci*, 23(10):4108–16, 2003. ISSN 1529-2401. doi: 10.1523/JNEUROSCI.23-10-04108.2003. URL https://www.ncbi.nlm.nih.gov/pubmed/12764098.

[62] A. C. Arevian, V. Kapoor, and N. N. Urban. Activity-dependent gating of lateral inhibition in the mouse olfactory bulb. *Nat Neurosci*, 11(1):80–7, 2008. ISSN 1097-6256. doi: 10.1038/nn2030. URL https://www.ncbi.nlm.nih.gov/pubmed/18084286.

[63] W. Xiong and W. R. Chen. Dynamic gating of spike propagation in the mitral cell lateral dendrites. *Neuron*, 34(1):115–26, 2002. ISSN 0896-6273. doi: 10.1016/s0896-6273(02)00628-1. URL https://www.ncbi.nlm.nih.gov/pubmed/11931746.

[64] J. K. Berry and D. Cox. Increased oscillatory power in a computational model of the olfactory bulb due to synaptic degeneration. *Phys Rev E*, 104(2-1):024405, 2021. ISSN 2470-0053. doi: 10.1103/PhysRevE.104.024405. URL https://www.ncbi.nlm.nih.gov/pubmed/34525666.

[65] D. P. Devanand, Seonjoo Lee, Jennifer Manly, Howard Andrews, Nicole Schupf, Richard L. Doty, Yaakov Stern, Laura B. Zahodne, Elan D. Louis, and Richard Mayeux. Olfactory deficits predict cognitive decline and alzheimer dementia in an urban community. *Neurology*, 84(2):182–189, 2015. ISSN 1526-632X 0028-3878. doi: 10.1212/WNL.0000000000001132. URL https://www.ncbi.nlm.nih.gov/pmc/articles/PMC4336090/.

[66] Marie-Elyse Lafaille-Magnan, Judes Poirier, Pierre Etienne, Jennifer Tremblay-Mercier, Joanne Frenette, Pedro Rosa-Neto, John C. S. Breitner, and Prevent-Ad Research Group. Odor identification as a biomarker of preclinical ad in older adults at risk. *Neurology*, 89(4):327–335, 2017. ISSN 1526-632X 0028-3878. doi: 10.1212/WNL.0000000000004159. URL https://www.ncbi.nlm.nih.gov/pmc/articles/PMC5574678/.

[67] Mirthe M. Ponsen, Diederick Stoffers, Jan Booij, Berthe L. F. van Eck-Smit, Erik Ch Wolters, and Henk W. Berendse. Idiopathic hyposmia as a preclinical sign of parkinson's disease. *Annals of Neurology*, 56(2):173–181, 2004. ISSN 0364-5134. doi: 10.1002/ana.20160. URL https://doi.org/10.1002/ana.20160.

[68] Michaela E. Johnson, Liza Bergkvist, Gabriela Mercado, Lucas Stetzik, Lindsay Meyerdirk, Emily Wolfrum, Zachary Madaj, Patrik Brundin, and Daniel W. Wesson. Deficits in olfactory sensitivity in a mouse model of parkinson's disease revealed by plethysmography of odor-evoked sniffing. *Scientific Reports*, 10(1):9242, 2020. ISSN 2045-2322. doi: 10.1038/s41598-020-66201-8. URL https://doi.org/10.1038/s41598-020-66201-8.

[69] G. Webster Ross, Helen Petrovitch, Robert D. Abbott, Caroline M. Tanner, Jordan Popper, Kamal Masaki, Lenore Launer, and Lon R. White. Association of olfactory dysfunction with risk for future parkinson's disease. *Annals of Neurology*, 63(2): 167–173, 2008. ISSN 0364-5134. doi: 10.1002/ana.21291. URL <GotoISI>://WOS:000253691500011.

[70] Johanna Neuner, Saak V. Ovsepian, Mario Dorostkar, Severin Filser, Aayush Gupta, Stylianos Michalakis, Martin Biel, and Jochen Herms. Pathological α-synuclein impairs adult-born granule cell development and functional integration in the olfactory bulb. *Nature Communications*, 5(1):3915, 2014. ISSN 2041-1723. doi: 10.1038/ncomms4915. URL https://doi.org/10.1038/ncomms4915.

[71] Daniel W. Wesson, Anne H. Borkowski, Gary E. Landreth, Ralph A. Nixon, Efrat Levy, and Donald A. Wilson. Sensory network dysfunction, behavioral impairments, and their reversibility in an alzheimer's β-amyloidosis mouse model. *The Journal of Neuroscience*, 31(44):15962, 2011. doi: 10.1523/JNEUROSCI.2085-11.2011. URL http://www.jneurosci.org/content/31/44/15962.abstract.

[72] Kensaku Mori, Hiroshi Nagao, and Yoshihiro Yoshihara. The olfactory bulb: Coding and processing of odor molecule information. *Science*, 286(5440):711, 1999. doi: 10.1126/science.286.5440.711. URL http://science.sciencemag.org/content/286/5440/711.abstract.

[73] Bettina Malnic, Junzo Hirono, Takaaki Sato, and Linda B. Buck. Combinatorial receptor codes for odors. *Cell*, 96(5):713–723, 1999. ISSN 0092-8674. doi: 10.1016/S0092-8674(00)80581-4. URL https://doi.org/10.1016/S0092-8674(00)80581-4.

[74] Christopher D. Wilson, Gabriela O. Serrano, Alexei A. Koulakov, and Dmitry Rinberg. A primacy code for odor identity. *Nature Communications*, 8(1):1477, 2017. ISSN 2041-1723. doi: 10.1038/s41467-017-01432-4. URL https://doi.org/10.1038/s41467-017-01432-4.

[75] Jörn Niessing and Rainer W. Friedrich. Olfactory pattern classification by discrete neuronal network states. *Nature*, 465(7294):47–52, 2010. ISSN 1476-4687. doi: 10.1038/nature08961. URL https://doi.org/10.1038/nature08961.

[76] Paul Miller. Dynamical systems, attractors, and neural circuits. *F1000Research*, 5: F1000 Faculty Rev–992, 2016. ISSN 2046-1402. doi: 10.12688/f1000research.7698.1. URL https://www.ncbi.nlm.nih.gov/pmc/articles/PMC4930057/.

[77] P. Erdi, T. Gröbler, G. Barna, and K. Kaski. Dynamics of the olfactory bulb: bifurcations, learning, and memory. *Biol Cybern*, 69(1):57–66, 1993. ISSN 0340-1200 (Print) 0340-1200. doi: 10.1007/bf00201408.

[78] Wenfeng Zhang, Changcheng Sun, Yufeng Shao, Zheng Zhou, Yiping Hou, and Anan Li. Partial depletion of dopaminergic neurons in the substantia nigra impairs olfaction and alters neural activity in the olfactory bulb. *Scientific Reports*, 9(1):254, 2019. ISSN 2045-2322. doi: 10.1038/s41598-018-36538-2. URL https://doi.org/10.1038/s41598-018-36538-2.

[79] Rebeca Hernández-Soto, Keila Dara Rojas-García, and Fernando Peña-Ortega. Sudden intrabulbar amyloid increase simultaneously disrupts olfactory bulb oscillations and odor detection. *Neural Plasticity*, 2019:3424906, 2019. ISSN 2090-5904. doi: 10.1155/2019/3424906. URL https://doi.org/10.1155/2019/3424906.

[80] J. Burré, M. Sharma, and T. C. Südhof. Cell biology and pathophysiology of α-synuclein. *Cold Spring Harb Perspect Med*, 8(3), 2018. ISSN 2157-1422. doi: 10.1101/cshperspect.a024091.

[81] Yvette C. Wong and Dimitri Krainc. α-synuclein toxicity in neurodegeneration: mechanism and therapeutic strategies. *Nature Medicine*, 23(2):1–13, 2017. ISSN 1546-170X. doi: 10.1038/nm.4269. URL https://doi.org/10.1038/nm.4269.

[82] Michael A. DeTure and Dennis W. Dickson. The neuropathological diagnosis of alzheimer's disease. *Molecular Neurodegeneration*, 14(1):32, 2019. ISSN 1750-1326. doi: 10.1186/s13024-019-0333-5. URL https://doi.org/10.1186/s13024-019-0333-5.

[83] Justin M. Long and David M. Holtzman. Alzheimer disease: An update on pathobiology and treatment strategies. *Cell*, 179(2):312–339, 2019. ISSN 0092-8674. doi: https://doi.org/10.1016/j.cell.2019.09.001. URL https://www.sciencedirect.com/science/article/pii/S0092867419310074.

[84] George S. Bloom. Amyloid-β and tau: The trigger and bullet in alzheimer disease pathogenesis. *JAMA Neurology*, 71(4):505–508, 2014. ISSN 2168-6149. doi: 10.1001/jamaneurol.2013.5847. URL https://doi.org/10.1001/jamaneurol.2013.5847.

[85] Tara L. Spires-Jones and Bradley T. Hyman. The intersection of amyloid beta and tau at synapses in alzheimer's disease. *Neuron*, 82(4):756–771, 2014. ISSN 1097-4199 0896-6273. doi: 10.1016/j.neuron.2014.05.004. URL https://www.ncbi.nlm.nih.gov/pmc/articles/PMC4135182/.

[86] Valentina Durante, Antonio de Iure, Vittorio Loffredo, Nishant Vaikath, Maria De Risi, Silvia Paciotti, Ana Quiroga-Varela, Davide Chiasserini, Manuela Mellone, Petra Mazzocchetti, Valeria Calabrese, Federica Campanelli, Alessandro Mechelli, Massimiliano Di Filippo, Veronica Ghiglieri, Barbara Picconi, Omar M. El-Agnaf, Elvira De Leonibus, Fabrizio Gardoni, Alessandro Tozzi, and Paolo Calabresi. Alpha-synuclein targets glun2a nmda receptor subunit causing striatal synaptic dysfunction and visuospatial memory alteration. *Brain*, 142(5):1365–1385, 2019. ISSN 0006-8950. doi: 10.1093/brain/awz065. URL https://doi.org/10.1093/brain/awz065.

[87] Laura A. Volpicelli-Daley, Kelvin C. Luk, Tapan P. Patel, Selcuk A. Tanik, Dawn M. Riddle, Anna Stieber, David F. Meaney, John Q. Trojanowski, and Virginia M. Y. Lee. Exogenous α-synuclein fibrils induce lewy body pathology leading to synaptic dysfunction and neuron death. *Neuron*, 72(1):57–71, 2011. ISSN 1097-4199 0896-6273. doi: 10.1016/j.neuron.2011.08.033. URL https://pubmed.ncbi.nlm.nih.gov/21982369.

[88] Walter J. Schulz-Schaeffer. Is cell death primary or secondary in the pathophysiology of idiopathic parkinson's disease? *Biomolecules*, 5(3):1467–1479, 2015. ISSN 2218-273X. doi: 10.3390/biom5031467. URL https://www.ncbi.nlm.nih.gov/pmc/articles/PMC4598759/.

[89] Sonja Blumenstock, Eva F. Rodrigues, Finn Peters, Lidia Blazquez-Llorca, Felix Schmidt, Armin Giese, and Jochen Herms. Seeding and transgenic overexpression of alpha-synuclein triggers dendritic spine pathology in the neocortex. *EMBO molecular medicine*, 9(5):716–731, 2017. ISSN 1757-4684 1757-4676. doi: 10.15252/emmm.201607305. URL https://www.ncbi.nlm.nih.gov/pmc/articles/PMC5412764/.

[90] Lujia Zhou, Joseph McInnes, Keimpe Wierda, Matthew Holt, Abigail G. Herrmann, Rosemary J. Jackson, Yu-Chun Wang, Jef Swerts, Jelle Beyens, Katarzyna Miskiewicz, Sven Vilain, Ilse Dewachter, Diederik Moechars, Bart De Strooper, Tara L. Spires-Jones, Joris De Wit, and Patrik Verstreken. Tau association with synaptic vesicles causes presynaptic dysfunction. *Nature communications*, 8:15295–15295, 2017. ISSN 2041-1723. doi: 10.1038/ncomms15295. URL https://www.ncbi.nlm.nih.gov/pmc/articles/PMC5437271/.

[91] Venu M. Nemani, Wei Lu, Victoria Berge, Ken Nakamura, Bibiana Onoa, Michael K. Lee, Farrukh A. Chaudhry, Roger A. Nicoll, and Robert H. Edwards. Increased expression of α-synuclein reduces neurotransmitter release by inhibiting synaptic vesicle reclustering after endocytosis. *Neuron*, 65(1):66–79, 2010. ISSN 0896-6273. doi: 10.1016/j.neuron.2009.12.023. URL https://doi.org/10.1016/j.neuron.2009.12.023.

[92] Mubashir Hassan, Qamar Abbas, Sung-Yum Seo, Saba Shahzadi, Hany Al Ashwal, Nazar Zaki, Zeeshan Iqbal, and Ahmed A. Moustafa. Computational modeling and biomarker studies of pharmacological treatment of alzheimer's disease (review). *Molecular medicine reports*, 18(1):639–655, 2018. ISSN 1791-3004 1791-2997. doi: 10.3892/mmr.2018.9044. URL https://www.ncbi.nlm.nih.gov/pmc/articles/PMC6059694/.

[93] Mark D. Humphries, Jose Angel Obeso, and Jakob Kisbye Dreyer. Insights into parkinson's disease from computational models of the basal ganglia. *Journal of neurology, neurosurgery, and psychiatry*, 89(11):1181–1188, 2018. ISSN 1468-330X 0022-3050. doi: 10.1136/jnnp-2017-315922. URL https://www.ncbi.nlm.nih.gov/pmc/articles/PMC6124639/.

[94] Ying Yu, Xiaomin Wang, Qishao Wang, and Qingyun Wang. A review of computational modeling and deep brain stimulation: applications to parkinson's disease. *Applied mathematics and mechanics*, pages 1–22, 2020. ISSN 1573-2754 0253-4827. doi: 10.1007/s10483-020-2689-9. URL https://www.ncbi.nlm.nih.gov/pmc/articles/PMC7672165/.

[95] J. N. Brea, L. M. Kay, and N. J. Kopell. Biophysical model for gamma rhythms in the olfactory bulb via subthreshold oscillations. *Proc Natl Acad Sci U S A*, 106 (51):21954–9, 2009. ISSN 1091-6490. doi: 10.1073/pnas.0910964106. URL https://www.ncbi.nlm.nih.gov/pubmed/19996171.

[96] M. Migliore, F. Cavarretta, A. Marasco, E. Tulumello, M. L. Hines, and G. M. Shepherd. Synaptic clusters function as odor operators in the olfactory bulb. *Proc Natl Acad Sci U S A*, 112(27):8499–504, 2015. ISSN 1091-6490. doi: 10.1073/pnas.1502513112. URL https://www.ncbi.nlm.nih.gov/pubmed/26100895.

[97] Walter J. Freeman. Spatial properties of an eeg event in the olfactory bulb and cortex. *Electroencephalography and Clinical Neurophysiology*, 44(5):586–605, 1978. ISSN 0013-4694. doi: https://doi.org/10.1016/0013-4694(78)90126-8. URL http://www.sciencedirect.com/science/article/pii/0013469478901268.

[98] Zhaoping Li. *A model of the olfactory bulb and beyond*. Dissertation, California Institute of Technology, 1990. URL https://resolver.caltech.edu/CaltechTHESIS:02192014-080819270.

[99] P. Virtanen, R. Gommers, T. E. Oliphant, M. Haberland, T. Reddy, D. Cournapeau, E. Burovski, P. Peterson, W. Weckesser, J. Bright, S. J. van der Walt, M. Brett, J. Wilson, K. J. Millman, N. Mayorov, A. R. J. Nelson, E. Jones, R. Kern, E. Larson, C. J. Carey, I. Polat, Y. Feng, E. W. Moore, J. VanderPlas, D. Laxalde, J. Perktold, R. Cimrman, I. Henriksen, E. A. Quintero, C. R. Harris, A. M.

Archibald, A. H. Ribeiro, F. Pedregosa, P. van Mulbregt, and SciPy 1.0 Contributors. Scipy 1.0: fundamental algorithms for scientific computing in python. *Nat Methods*, 17(3):261–272, 2020. ISSN 1548-7105. doi: 10.1038/s41592-019-0686-2. URL https://www.ncbi.nlm.nih.gov/pubmed/32015543.

[100] See supplemental material at [url will be inserted by publisher] for full parameters and additional figures.

[101] I. Aradi, G. Barna, P. Érdi, and T. Grobler. Chaos and learning in the olfactory bulb. *International Journal of Intelligent Systems*, 10(1):89–117, 1995. ISSN 0884-8173. doi: https://doi.org/10.1002/int.4550100108. URL https://doi.org/10.1002/int.4550100108.

[102] Paula Desplats, He-Jin Lee, Eun-Jin Bae, Christina Patrick, Edward Rockenstein, Leslie Crews, Brian Spencer, Eliezer Masliah, and Seung-Jae Lee. Inclusion formation and neuronal cell death through neuron-to-neuron transmission of alpha-synuclein. *Proceedings of the National Academy of Sciences of the United States of America*, 106 (31):13010–13015, 2009. ISSN 1091-6490 0027-8424. doi: 10.1073/pnas.0903691106. URL https://www.ncbi.nlm.nih.gov/pmc/articles/PMC2722313/.

[103] Isabel Ubeda-Bañon, Daniel Saiz-Sanchez, Carlos de la Rosa-Prieto, and Alino Martinez-Marcos. α-synuclein in the olfactory system in parkinson's disease: role of neural connections on spreading pathology. *Brain Structure and Function*, 219(5): 1513–1526, 2014. ISSN 1863-2661. doi: 10.1007/s00429-013-0651-2. URL https://doi.org/10.1007/s00429-013-0651-2.

[104] Nolwen L. Rey, Jennifer A. Steiner, Nazia Maroof, Kelvin C. Luk, Zachary Madaj, John Q. Trojanowski, Virginia M. Y. Lee, and Patrik Brundin. Widespread transneuronal propagation of α-synucleinopathy triggered in olfactory bulb mimics prodromal parkinson's disease. *The Journal of experimental medicine*, 213(9):1759–1778, 2016. ISSN 1540-9538 0022-1007. doi: 10.1084/jem.20160368. URL https://www.ncbi.nlm.nih.gov/pmc/articles/PMC4995088/.

[105] Nolwen L. Rey, Sonia George, Jennifer A. Steiner, Zachary Madaj, Kelvin C. Luk, John Q. Trojanowski, Virginia M. Y. Lee, and Patrik Brundin. Spread of aggregates after olfactory bulb injection of α-synuclein fibrils is associated with early neuronal loss and is reduced long term. *Acta neuropathologica*, 135(1):65–83, 2018. ISSN 1432-0533 0001-6322. doi: 10.1007/s00401-017-1792-9. URL https://www.ncbi.nlm.nih.gov/pmc/articles/PMC5756266/.

[106] Ayami Okuzumi, Masaru Kurosawa, Taku Hatano, Masashi Takanashi, Shuuko Nojiri, Takeshi Fukuhara, Tomoyuki Yamanaka, Haruko Miyazaki, Saki Yoshinaga, Yoshiaki Furukawa, Tomomi Shimogori, Nobutaka Hattori, and Nobuyuki Nukina.

Rapid dissemination of alpha-synuclein seeds through neural circuits in an in-vivo prion-like seeding experiment. *Acta Neuropathologica Communications*, 6(1):96, 2018. ISSN 2051-5960. doi: 10.1186/s40478-018-0587-0. URL https://doi.org/10.1186/s40478-018-0587-0.

[107] Francesca Longhena, Gaia Faustini, Cristina Missale, Marina Pizzi, PierFranco Spano, and Arianna Bellucci. The contribution of α-synuclein spreading to parkinson's disease synaptopathy. *Neural plasticity*, 2017:5012129–5012129, 2017. ISSN 1687-5443 2090-5904. doi: 10.1155/2017/5012129. URL https://www.ncbi.nlm.nih.gov/pmc/articles/PMC5241463/.

[108] Hyun Kyung Chung, Hoang-Anh Ho, Dayana Pérez-Acuña, and Seung-Jae Lee. Modeling α-synuclein propagation with preformed fibril injections. *Journal of movement disorders*, 12(3):139–151, 2019. ISSN 2005-940X 2093-4939. doi: 10.14802/jmd.19046. URL https://www.ncbi.nlm.nih.gov/pmc/articles/PMC6763716/.

[109] J. Stöhr, J. C. Watts, Z. L. Mensinger, A. Oehler, S. K. Grillo, S. J. DeArmond, S. B. Prusiner, and K. Giles. Purified and synthetic alzheimer's amyloid beta (aβ) prions. *Proc Natl Acad Sci U S A*, 109(27):11025–30, 2012. ISSN 0027-8424 (Print) 0027-8424. doi: 10.1073/pnas.1206555109.

[110] J. C. Watts, C. Condello, J. Stöhr, A. Oehler, J. Lee, S. J. DeArmond, L. Lannfelt, M. Ingelsson, K. Giles, and S. B. Prusiner. Serial propagation of distinct strains of aβ prions from alzheimer's disease patients. *Proc Natl Acad Sci U S A*, 111(28):10323–8, 2014. ISSN 0027-8424 (Print) 0027-8424. doi: 10.1073/pnas.1408900111.

[111] Justin M. Nussbaum, Matthew E. Seward, and George S. Bloom. Alzheimer disease: a tale of two prions. *Prion*, 7(1):14–19, 2013. ISSN 1933-690X 1933-6896. doi: 10.4161/pri.22118. URL https://www.ncbi.nlm.nih.gov/pmc/articles/PMC3609044/.

[112] I. C. Stancu, B. Vasconcelos, L. Ris, P. Wang, A. Villers, E. Peeraer, A. Buist, D. Terwel, P. Baatsen, T. Oyelami, N. Pierrot, C. Casteels, G. Bormans, P. Kienlen-Campard, J. N. Octave, D. Moechars, and I. Dewachter. Templated misfolding of tau by prion-like seeding along neuronal connections impairs neuronal network function and associated behavioral outcomes in tau transgenic mice. *Acta Neuropathol*, 129(6):875–94, 2015. ISSN 0001-6322 (Print) 0001-6322. doi: 10.1007/s00401-015-1413-4.

[113] Jacob W. Vogel, Yasser Iturria-Medina, Olof T. Strandberg, Ruben Smith, Elizabeth Levitis, Alan C. Evans, Oskar Hansson, Michael Weiner, Paul Aisen, Ronald Petersen, Clifford R. Jack, William Jagust, John Q. Trojanowki, Arthur W. Toga, Laurel Beckett, Robert C. Green, Andrew J. Saykin, John Morris, Leslie M. Shaw, Enchi Liu, Tom Montine, Ronald G. Thomas, Michael Donohue, Sarah Walter, Devon Gessert, Tamie Sather, Gus Jiminez, Danielle Harvey, Matthew Bernstein, Nick Fox,

Paul Thompson, Norbert Schuff, Charles DeCarli, Bret Borowski, Jeff Gunter, Matt Senjem, Prashanthi Vemuri, David Jones, Kejal Kantarci, Chad Ward, Robert A. Koeppe, Norm Foster, Eric M. Reiman, Kewei Chen, Chet Mathis, Susan Landau, Nigel J. Cairns, Erin Householder, Lisa Taylor Reinwald, Virginia Lee, Magdalena Korecka, Michal Figurski, Karen Crawford, Scott Neu, Tatiana M. Foroud, Steven Potkin, Li Shen, Faber Kelley, Sungeun Kim, Kwangsik Nho, Zaven Kachaturian, Richard Frank, Peter J. Snyder, Susan Molchan, Jeffrey Kaye, Joseph Quinn, Betty Lind, Raina Carter, Sara Dolen, Lon S. Schneider, Sonia Pawluczyk, Mauricio Beccera, Liberty Teodoro, Bryan M. Spann, James Brewer, Helen Vanderswag, Adam Fleisher, Judith L. Heidebrink, Joanne L. Lord, Sara S. Mason, Colleen S. Albers, David Knopman, Kris Johnson, Rachelle S. Doody, Javier Villanueva Meyer, Munir Chowdhury, Susan Rountree, Mimi Dang, Yaakov Stern, Lawrence S. Honig, Karen L. Bell, Beau Ances, John C. Morris, Maria Carroll, Sue Leon, Mark A. Mintun, Stacy Schneider, Angela OliverNg, Randall Griffith, David Clark, et al. Spread of pathological tau proteins through communicating neurons in human alzheimer's disease. *Nature Communications*, 11(1):2612, 2020. ISSN 2041-1723. doi: 10.1038/s41467-020-15701-2. URL `https://doi.org/10.1038/s41467-020-15701-2`.

[114] 3rd Kelleher, Raymond J. and Jie Shen. Presenilin-1 mutations and alzheimer's disease. *Proceedings of the National Academy of Sciences of the United States of America*, 114 (4):629–631, 2017. ISSN 1091-6490 0027-8424. doi: 10.1073/pnas.1619574114. URL `https://www.ncbi.nlm.nih.gov/pmc/articles/PMC5278466/`.

[115] Reynaldo Alvarado-Martínez, Karla Salgado-Puga, and Fernando Peña-Ortega. Amyloid beta inhibits olfactory bulb activity and the ability to smell. *PloS one*, 8(9): e75745–e75745, 2013. ISSN 1932-6203. doi: 10.1371/journal.pone.0075745. URL `https://www.ncbi.nlm.nih.gov/pmc/articles/PMC3784413/`.

[116] L. F. Abbott and P. Dayan. *Theoretical Neuroscience: Computational and Mathematical Modeling of Neural Systems*. Computational Neuroscience Series. MIT Press, 2005. ISBN 9780262311427. URL `https://books.google.com/books?id=Wi4MEAAAQBAJ`.

[117] Guoshi Li and Thomas A. Cleland. A two-layer biophysical model of cholinergic neuromodulation in olfactory bulb. *The Journal of Neuroscience*, 33(7):3037, 2013. doi: 10.1523/JNEUROSCI.2831-12.2013. URL `http://www.jneurosci.org/content/33/7/3037.abstract`.

[118] B. Iravani, A. Arshamian, K. Ohla, D.A. Wilson, and M. Lundström. Non-invasive recording from the human olfactory bulb. *Nature Communications*, 11:648, 2020. ISSN 1529-2401. doi: 10.1038/s41467-020-14520-90. URL `https://www.nature.com/articles/s41467-020-14520-9`.

[119] M. Mueller and V. Egger. Dendritic integration in olfactory bulb granule cells upon simultaneous multispine activation: Low thresholds for nonlocal spiking activity. *PLoS Biol*, 18(9):e3000873, 2020. ISSN 1545-7885. doi: 10.1371/journal.pbio.3000873. URL https://www.ncbi.nlm.nih.gov/pubmed/32966273.

[120] B. N. Cazakoff, B. Y. Lau, K. L. Crump, H. S. Demmer, and S. D. Shea. Broadly tuned and respiration-independent inhibition in the olfactory bulb of awake mice. *Nat Neurosci*, 17(4):569–76, 2014. ISSN 1546-1726. doi: 10.1038/nn.3669. URL https://www.ncbi.nlm.nih.gov/pubmed/24584050.

[121] D. Rinberg, A. Koulakov, and A. Gelperin. Sparse odor coding in awake behaving mice. *J Neurosci*, 26(34):8857–65, 2006. ISSN 1529-2401. doi: 10.1523/JNEUROSCI.0884-06.2006. URL https://www.ncbi.nlm.nih.gov/pubmed/16928875.

[122] Eugene M. Izhikevich. *Dynamical systems in neuroscience : the geometry of excitability and bursting*. Computational neuroscience. MIT Press, Cambridge, Mass., 2007. ISBN 0262090430 (alk. paper) 9780262090438 (alk. paper).

[123] M. B. Richard, S. R. Taylor, and C. A. Greer. Age-induced disruption of selective olfactory bulb synaptic circuits. *Proc Natl Acad Sci U S A*, 107(35):15613–8, 2010. ISSN 1091-6490. doi: 10.1073/pnas.1007931107. URL https://www.ncbi.nlm.nih.gov/pubmed/20679234.

[124] J. P. Royet, C. Souchier, F. Jourdan, and H. Ploye. Morphometric study of the glomerular population in the mouse olfactory bulb: numerical density and size distribution along the rostrocaudal axis. *J Comp Neurol*, 270(4):559–68, 1988. ISSN 0021-9967. doi: 10.1002/cne.902700409. URL https://www.ncbi.nlm.nih.gov/pubmed/3372747.

[125] S. L. Pomeroy, A. S. LaMantia, and D. Purves. Postnatal construction of neural circuitry in the mouse olfactory bulb. *J Neurosci*, 10(6):1952–66, 1990. ISSN 0270-6474. doi: 10.1523/JNEUROSCI.10-06-01952.1990. URL https://www.ncbi.nlm.nih.gov/pubmed/2355260.

[126] S. D. Burton and N. N. Urban. Greater excitability and firing irregularity of tufted cells underlies distinct afferent-evoked activity of olfactory bulb mitral and tufted cells. *J Physiol*, 592(10):2097–118, 2014. ISSN 1469-7793. doi: 10.1113/jphysiol.2013.269886. URL https://www.ncbi.nlm.nih.gov/pubmed/24614745.

[127] K. Mori, K. Kishi, and H. Ojima. Distribution of dendrites of mitral, displaced mitral, tufted, and granule cells in the rabbit olfactory bulb. *J Comp Neurol*, 219(3):339–55, 1983. ISSN 0021-9967. doi: 10.1002/cne.902190308. URL https://www.ncbi.nlm.nih.gov/pubmed/6619342.

[128] E. Orona, E. C. Rainer, and J. W. Scott. Dendritic and axonal organization of mitral and tufted cells in the rat olfactory bulb. *J Comp Neurol*, 226(3):346–56, 1984. ISSN 0021-9967. doi: 10.1002/cne.902260305. URL https://www.ncbi.nlm.nih.gov/pubmed/6747027.

[129] E. M. Izhikevich. Simple model of spiking neurons. *IEEE Trans Neural Netw*, 14 (6):1569–72, 2003. ISSN 1045-9227. doi: 10.1109/TNN.2003.820440. URL https://www.ncbi.nlm.nih.gov/pubmed/18244602.

[130] M. A. Geramita, S. D. Burton, and N. N. Urban. Distinct lateral inhibitory circuits drive parallel processing of sensory information in the mammalian olfactory bulb. *Elife*, 5, 2016. ISSN 2050-084X. doi: 10.7554/eLife.16039. URL https://www.ncbi.nlm.nih.gov/pubmed/27351103.

[131] A. K. Dhawale, A. Hagiwara, U. S. Bhalla, V. N. Murthy, and D. F. Albeanu. Non-redundant odor coding by sister mitral cells revealed by light addressable glomeruli in the mouse. *Nat Neurosci*, 13(11):1404–12, 2010. ISSN 1546-1726. doi: 10.1038/nn.2673. URL https://www.ncbi.nlm.nih.gov/pubmed/20953197.

[132] A. B. McIntyre and T. A. Cleland. Biophysical constraints on lateral inhibition in the olfactory bulb. *J Neurophysiol*, 115(6):2937–49, 2016. ISSN 1522-1598. doi: 10.1152/jn.00671.2015. URL https://www.ncbi.nlm.nih.gov/pubmed/27009162.

[133] A Destexhe, Z F Mainen, and Sejnowski T J. *Kinetic Models of Synaptic Transmission*. MIT Press, 1998.

[134] R. Rasmussen, J. O'Donnell, F. Ding, and M. Nedergaard. Interstitial ions: A key regulator of state-dependent neural activity? *Prog Neurobiol*, 193:101802, 2020. ISSN 1873-5118. doi: 10.1016/j.pneurobio.2020.101802. URL https://www.ncbi.nlm.nih.gov/pubmed/32413398.

[135] N. Brunel and X. J. Wang. Effects of neuromodulation in a cortical network model of object working memory dominated by recurrent inhibition. *J Comput Neurosci*, 11(1):63–85, 2001. ISSN 0929-5313. doi: 10.1023/a:1011204814320. URL https://www.ncbi.nlm.nih.gov/pubmed/11524578.

[136] G. R. Holt and C. Koch. Electrical interactions via the extracellular potential near cell bodies. *J Comput Neurosci*, 6(2):169–84, 1999. ISSN 0929-5313. doi: 10.1023/a:1008832702585. URL https://www.ncbi.nlm.nih.gov/pubmed/10333161.

[137] G. T. Einevoll, C. Kayser, N. K. Logothetis, and S. Panzeri. Modelling and analysis of local field potentials for studying the function of cortical circuits. *Nat Rev Neurosci*, 14 (11):770–85, 2013. ISSN 1471-0048. doi: 10.1038/nrn3599. URL https://www.ncbi.nlm.nih.gov/pubmed/24135696.

[138] R. Lethbridge, Q. Hou, C. W. Harley, and Q. Yuan. Olfactory bulb glomerular nmda receptors mediate olfactory nerve potentiation and odor preference learning in the neonate rat. *PLoS One*, 7(4):e35024, 2012. ISSN 1932-6203. doi: 10.1371/journal.pone.0035024. URL https://www.ncbi.nlm.nih.gov/pubmed/22496886.

[139] T. W. Margrie and A. T. Schaefer. Theta oscillation coupled spike latencies yield computational vigour in a mammalian sensory system. *J Physiol*, 546(Pt 2):363–74, 2003. ISSN 0022-3751. doi: 10.1113/jphysiol.2002.031245. URL https://www.ncbi.nlm.nih.gov/pubmed/12527724.

[140] M. Kollo, A. Schmaltz, M. Abdelhamid, I. Fukunaga, and A. T. Schaefer. 'silent' mitral cells dominate odor responses in the olfactory bulb of awake mice. *Nat Neurosci*, 17 (10):1313–5, 2014. ISSN 1546-1726. doi: 10.1038/nn.3768. URL https://www.ncbi.nlm.nih.gov/pubmed/25064849.

[141] C. Labarrera, M. London, and K. Angelo. Tonic inhibition sets the state of excitability in olfactory bulb granule cells. *J Physiol*, 591(7):1841–50, 2013. ISSN 1469-7793. doi: 10.1113/jphysiol.2012.241851. URL https://www.ncbi.nlm.nih.gov/pubmed/23318869.

[142] S. D. Burton and N. N. Urban. Rapid feedforward inhibition and asynchronous excitation regulate granule cell activity in the mammalian main olfactory bulb. *J Neurosci*, 35 (42):14103–22, 2015. ISSN 1529-2401. doi: 10.1523/JNEUROSCI.0746-15.2015. URL https://www.ncbi.nlm.nih.gov/pubmed/26490853.

[143] D. Nunes and T. Kuner. Disinhibition of olfactory bulb granule cells accelerates odour discrimination in mice. *Nat Commun*, 6:8950, 2015. ISSN 2041-1723. doi: 10.1038/ncomms9950. URL https://www.ncbi.nlm.nih.gov/pubmed/26592770.

[144] D. Desmaisons, J. D. Vincent, and P. M. Lledo. Control of action potential timing by intrinsic subthreshold oscillations in olfactory bulb output neurons. *J Neurosci*, 19 (24):10727–37, 1999. ISSN 1529-2401. doi: 10.1523/JNEUROSCI.19-24-10727.1999. URL https://www.ncbi.nlm.nih.gov/pubmed/10594056.

[145] R. Balu, P. Larimer, and B. W. Strowbridge. Phasic stimuli evoke precisely timed spikes in intermittently discharging mitral cells. *J Neurophysiol*, 92(2):743–53, 2004. ISSN 0022-3077. doi: 10.1152/jn.00016.2004. URL https://www.ncbi.nlm.nih.gov/pubmed/15277594.

[146] T. W. Margrie, B. Sakmann, and N. N. Urban. Action potential propagation in mitral cell lateral dendrites is decremental and controls recurrent and lateral inhibition in the mammalian olfactory bulb. *Proc Natl Acad Sci U S A*, 98(1):319–24, 2001. ISSN 0027-8424. doi: 10.1073/pnas.98.1.319. URL https://www.ncbi.nlm.nih.gov/pubmed/11120888.

[147] G. Lowe. Inhibition of backpropagating action potentials in mitral cell secondary dendrites. *J Neurophysiol*, 88(1):64–85, 2002. ISSN 0022-3077. doi: 10.1152/jn.2002.88.1.64. URL `https://www.ncbi.nlm.nih.gov/pubmed/12091533`.

Appendix A

Appendix to Chapter 2

A.1 Average Oscillatory Power for All Cases

A.1.1 Other Components Damaged

Trials were also run with damage delivered to components of the network beside W_0 and H_0, namely to:

- Granule cell layer
- Mitral cell layer
- $\mathbf{I}_{\text{odor}}$, the input to mitral cells from the glomerular layer

Internal damage to the mitral cell layer (MCL) or to the granule cell layer (GCL) is implemented by multiplying the right-hand-side of the differential equation (except for the leak term) for the given cell by some fraction less than one, $(1 - \delta_i)$. For example,

$$\dot{x}_i = (1 - \delta_i)(-\sum_j H_{0,ij}\ g_{y,j}(y_j) + I_{b,i} + I_{\text{odor},i}(t)) - \alpha\ x_i$$

would be damage delivered to the i^{th} mitral cell unit. In this case, δ is calculated as

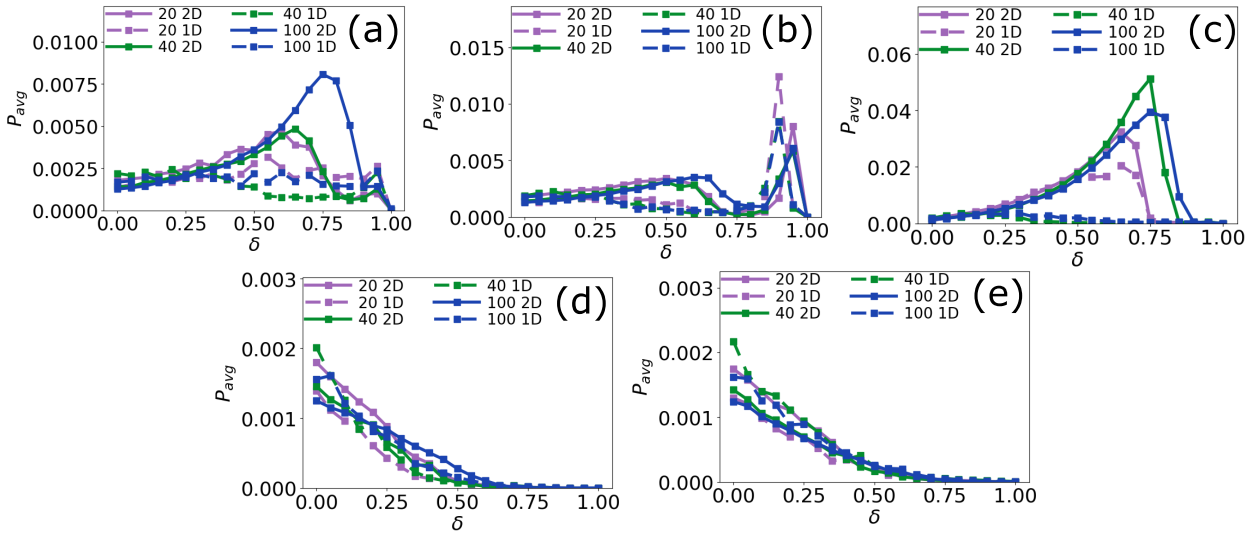

Figure A.1: Average ocillatory power (P_{avg}) for flat damage to W_0 (a), H_0 (b), GCL (c), MCL (d), and OI (e) in every network architecture (20 units 1D, 20 units 2D, 40 units 1D, 40 units 2D, 100 units 1D, and 100 units 2D). Solid lines are 2D networks, dashed lines are 1D networks. Note that the vertical axes do not have the same scale.

$$\delta = \sum_i \frac{\delta_i}{N},$$

where N is the number of mitral cells.

Figures A.1 through A.3 show average oscillatory power with damage for each type of damage to each type of network.

A.1.2 Flat Damage to Both H0 and W0 in the 2D 100 Unit Network

Similar to FD to H_0 or W_0, FD to both resulted in an increase in oscillatory power at intermediate levels of damage (Fig. A.4). Delivering damage to both seems to result in approximately the mean effect of each individually, in terms of the maximum oscillatory power reached and the location of the maximum.

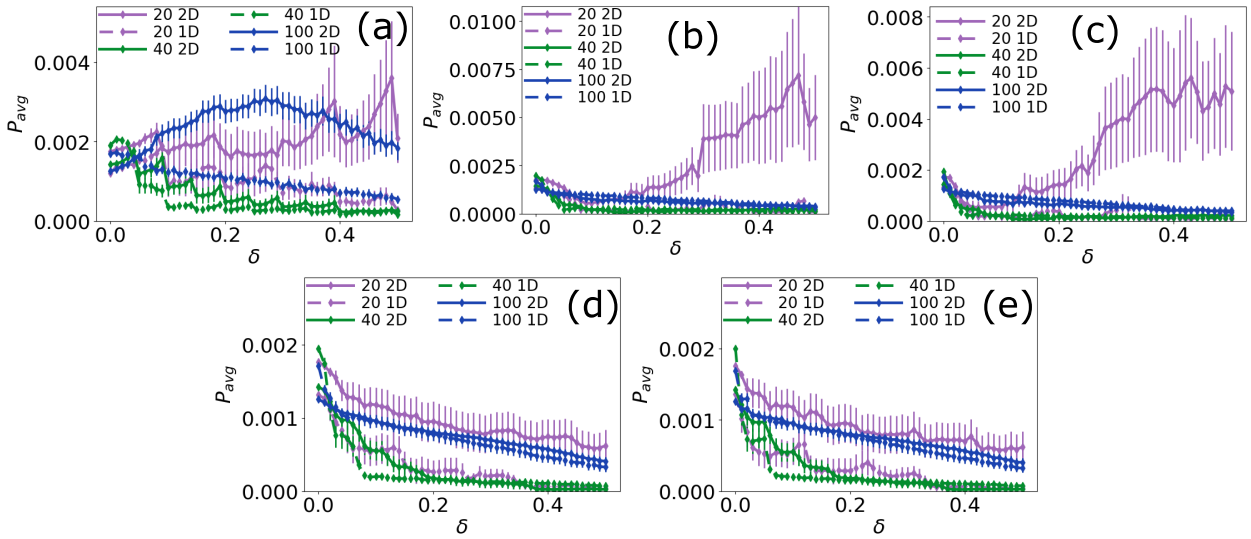

Figure A.2: Average oscillatory power (P_{avg}) for columnar damage to W_0 (a), H_0 (b), GCL (c), MCL (d), and OI (e) in every network architecture (20 units 1D, 20 units 2D, 40 units 1D, 40 units 2D, 100 units 1D, and 100 units 2D). Solid lines are 2D networks, dashed lines are 1D networks. Note that the vertical axes do not have the same scale.

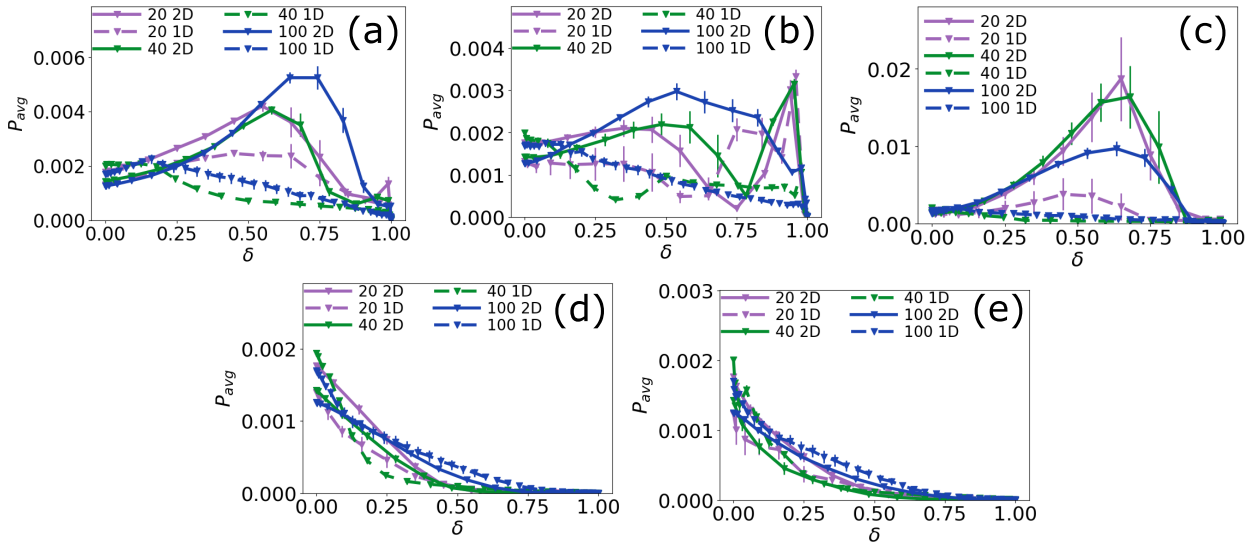

Figure A.3: Average oscillatory power (P_{avg}) for seeded damage to W_0 (a), H_0 (b), GCL (c), MCL (d), and OI (e) in every network architecture (20 units 1D, 20 units 2D, 40 units 1D, 40 units 2D, 100 units 1D, and 100 units 2D). Solid lines are 2D networks, dashed lines are 1D networks. Note that the vertical axes do not have the same scale.

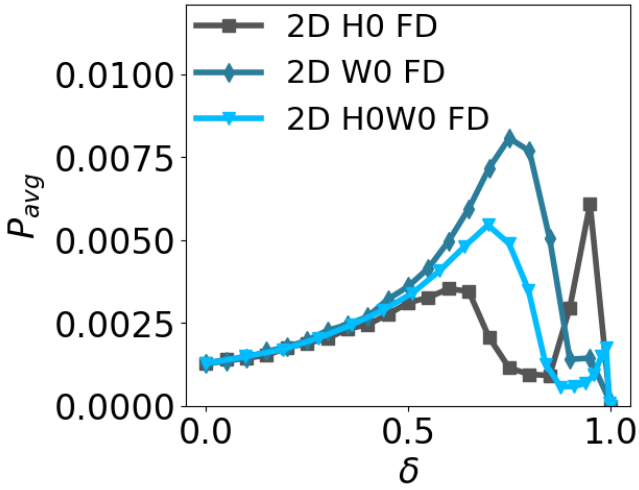

Figure A.4: Average oscillatory power for flat damage to both H_0 and W_0 compared to flat damage to only H_0 and flat damage to only W_0 in the 2D 100 unit network.

For Fig. A.4, δ was measured as,

$$\delta = 1 - \frac{\sum_{ij}[H_{\text{Damaged}} W_{\text{Damaged}}]_{ij}}{\sum_{ij}[H_0 W_0]_{ij}}.$$

Calculating δ this way is equivalent to δ in the main paper for W_0 or H_0, as long as the damage delivered is flat damage. Calculating δ in this manner allows us to compare damage against the same baseline for each target. It is also partly inspired by the linearized analysis summarized in Results, where oscillatory activity was predicted by the matrix,

$$A = H_0 G'_y(\mathbf{y_0}) W_0 G'_x(\mathbf{x_0}),$$

where $G'_y(\mathbf{y_0})$ and $G'_x(\mathbf{x_0})$ are diagonal matrices.

A.2 Addressing Late Peak in Average Power for Flat Damage to H0

Fig. A.5 shows the cell activity and associated power spectra for each unit in the 2D 100 unit network at the damage level corresponding to maximum oscillatory power for flat damage to H_0, demonstrating how oscillatory activity in the network gives rise to P_{avg}. Fig. A.6 is the same, but for the damage level corresponding to the late peak in P_{avg} seen in Fig. 2.4 (and in Fig. A.1(b)) and demonstrates how spurious P_{avg} signals can arise at high levels of flat damage to H_0.

In the case shown in Fig. A.6, most units have a significant signal in their power spectra, but no units show oscillations (compare with Fig. A.5). At high levels of flat damage to H0, the MC unit population reaches higher levels of output state. When odor input decreases, more than half of them drop back down sharply during the time window over which the periodogram is calculated (from 125 to 250 ms). This leads to a large signal in the spectrum and the peak in P_{avg} that is not actually indicative of oscillatory behavior.

A.3 Fixed Point Dependence on H0 and W0

Sections A.3 and A.4 come from supplemental material[100] from [64].

In the Li-Hopfield work, to gain understanding of the full numerical solution, an adiabatic approximation is made in which the oscillations are modeled as variations around a fixed point. Under this simplification, the internal state fixed point is a fair representation of the average internal state. With that assumption, we can explore fixed point dependence on H_0 and W_0. To make the following analysis tractable, we make two simplifications. First, we reduce the network to a single MC unit and a single GC unit. Second, we approximate the

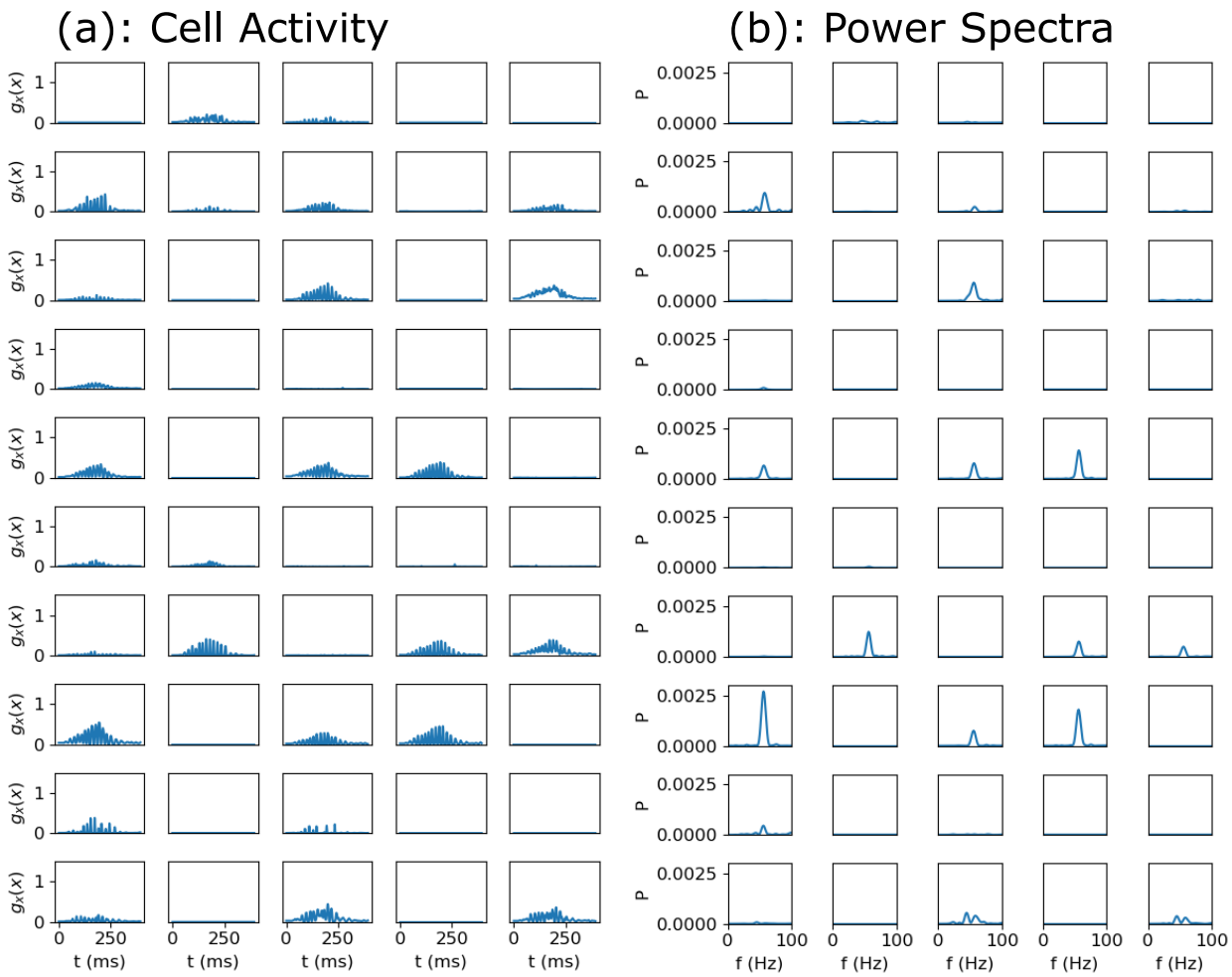

Figure A.5: (a) Each panel shows the activity of a single MC unit in the 2D 100 unit network at the level of flat damage to H_0 corresponding to the greatest amount of oscillatory activity ($\delta = 0.6$). (b) Each panel shows the power spectrum corresponding to each MC unit. This demonstrates oscillatory activity giving rise to P_{avg}.

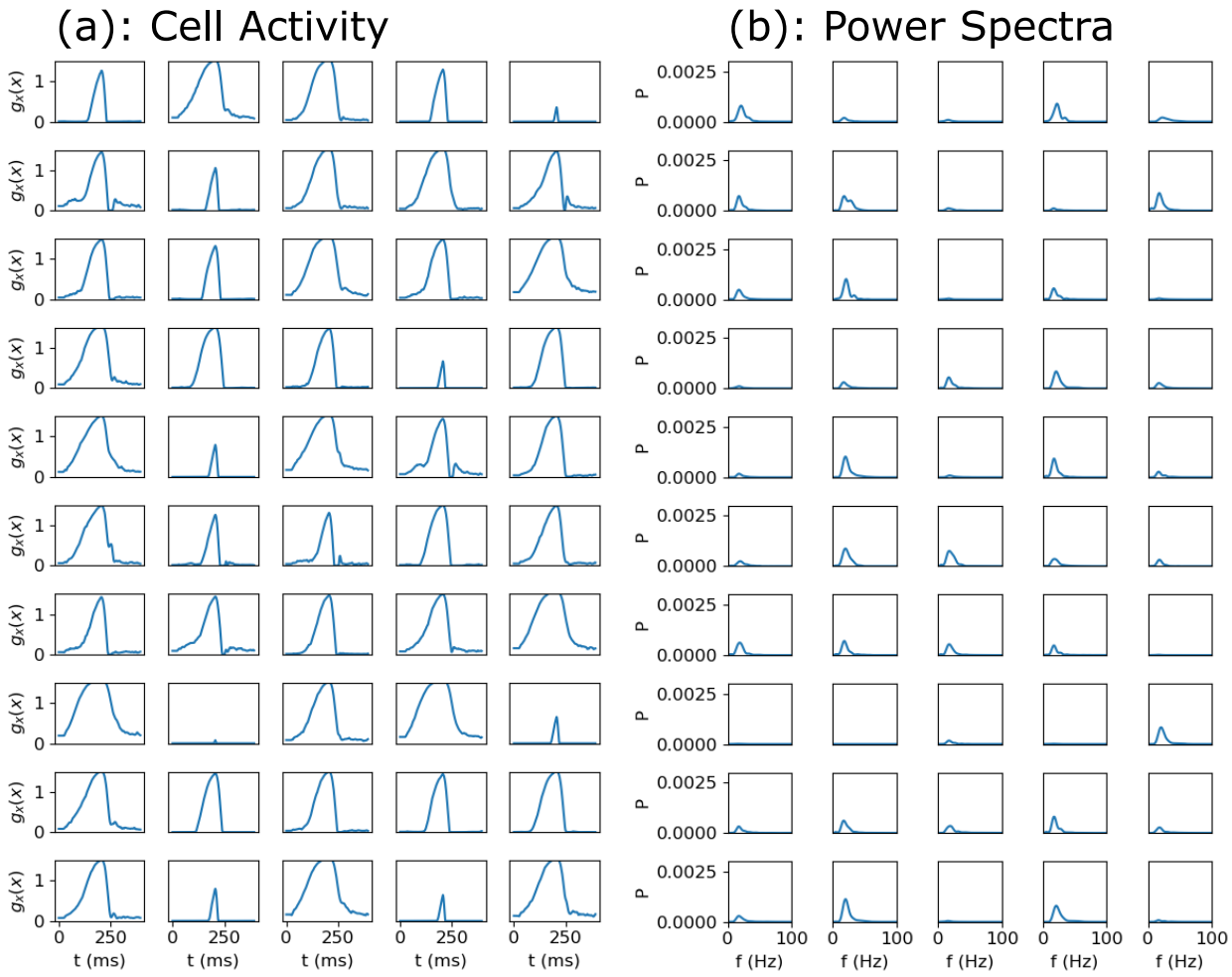

Figure A.6: (a) Each panel shows the activity of a single MC unit in the 2D 100 unit network at the level of flat damage ($\delta = 0.95$) to H_0 corresponding to the sharp peak in P_{avg} seen in Fig. 4(a) in the main text. (b) Each panel shows the power spectrum corresponding to each MC unit. Though most units have a significant signal in their power spectra, no units show oscillations.

activation functions with a first-order Taylor series expansion around the observed average internal state of active units ($x_{\text{avg,obs}}$ and $y_{\text{avg,obs}}$),

$$\begin{aligned} g_y(y) &\approx g_y(y_{\text{avg,obs}}) + g'_y(y_{\text{avg,obs}})(y_0 - y_{\text{avg,obs}}) \\ &= a_y + b_y y_0, \end{aligned} \tag{A.1}$$

$$\begin{aligned} g_x(x) &\approx g_x(x_{\text{avg,obs}}) + g'_x(x_{\text{avg,obs}})(x_0 - x_{\text{avg,obs}}) \\ &= a_x + b_x x_0, \end{aligned} \tag{A.2}$$

where $a_y = -0.6847,\ b_y = 0.9693,\ a_x = -0.2132,\ b_x = 0.8223$ are constants based on the average internal state during trials delivering flat damage to H_0 and W_0. Thus the fixed point equations become

$$0 = -h_0(a_y + b_y y_0) - \alpha x_0 + I_{\text{odor}} + I_b, \tag{A.3}$$

$$0 = w_0(a_x + b_x x_0) - \alpha y_0 + I_c. \tag{A.4}$$

We can now analytically solve for x_0 and differentiate with respect to w_0 and h_0,

$$\frac{\partial x_0}{\partial w_0} = \frac{\alpha h_0 b_x b_y [h_0(I_c b_y/\alpha + a_y) - I_o - \alpha a_x/b_x]}{(h_0 w_0 b_x b_y + \alpha^2)^2}, \tag{A.5}$$

$$\frac{\partial x_0}{\partial h_0} = \frac{-\alpha^2 b_y [w_0(I_o b_x/\alpha + a_x) + I_c + \alpha a_y/by]}{(h_0 w_0 b_x b_y + \alpha^2)^2}. \tag{A.6}$$

For simplicity, I_{odor} is set to a constant value and collected with I_b:

$$I_o = I_b + I_{\text{odor}}(t = 175ms) = 0.99375$$

.

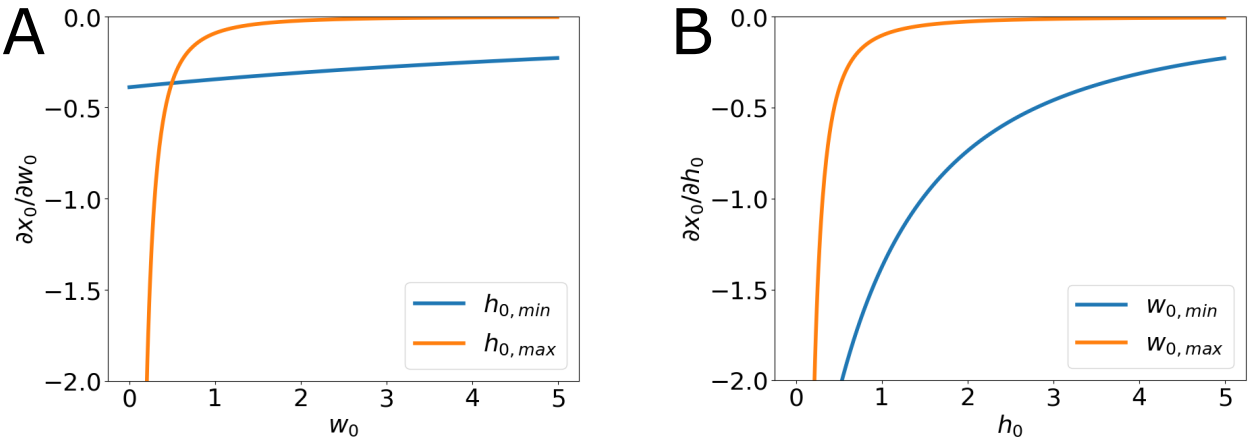

Figure A.7: Fixed Point Dependence on H_0 and W_0. A: The partial derivative of the fixed point with respect to w_0 is plotted against w_0 using the minimum and maximum values of H_0 in the 100 cell 2D network ($H_{0,\min} = 0.0017,\ H_{0,\max} = 2.0606$). B: The partial derivative with respect to h_0 plotted against h_0 using the minimum and maximum values of W_0 in the 100 cell 2D network ($W_{0,\min} = 0.0163,\ W_{0,\max} = 1.6982$).

When plotted (Fig. A.7), it becomes apparent that for all values of h_0 and w_0 within the range used in the work here, the derivatives are negative, meaning that a decrease in W_0 or H_0 increases x_0, as seen in FD to W_0 and H_0.

A.4 Cell Activity with Damage Progression

A.4.1 Evolution of Cell Activity in Seeded Damage to W0 in the 2D 100 Unit Network

Cell activity ($\mathbf{g_x}$) at various levels of seeded damage to W0 in the 2D 100 unit network, with the associated power spectrum are plotted next to each other (Fig. A.8). The inhale peak is at 205 ms. The oscillation amplitude can be seen to grow from $\delta = 0$ to $\delta = 0.8448$, which is reflected clearly in the power spectra. Note that the vertical scale is larger in the last cell activity plot. The sharp fall in activity from about 225 ms to 300 ms can cause an increase

in P_{avg}, but clearly is not actually an example of gamma band oscillatory behavior and is the reason for the shortened time window used for calculating the power spectra for P_{avg}.

As stated in the text, the power spectrum was calculated from the cell activity high-pass filtered above 15 Hz from 125 ms to 250 ms. Some power density was present above 100 Hz, but power density below 100 Hz dominated the contribution to P_{avg}.

A.4.2 Evolution of Cell Activity in Flat Damage to H0 in the 2D 100 Unit Network

Cell activity ($\mathbf{g_x}$) at various levels of flat damage to H_0 in the 1D 100 unit network, with the associated power spectrum are plotted next to each (Fig A.9). The inhale peak is at 205 ms. The cell activity changes little from $\delta = 0$ to $\delta = 0.5$. Note that the vertical scale is larger in the last two plots of cell activity. The sharp rise then drop seen in $\delta = 0.9$ and $\delta = 0.95$ is the cause of the spike in P_{avg} at the highest levels of damage for flat damage to H_0 in the 2D 100 unit network (see Fig. A.9), and is an example of what causes the similar spikes in P_{avg} for flat damage to H0 in all networks (see Fig. A.9 and Fig. 2.4(a) in Chapter 2), and for seeded damage to H0 in the 1D 20 unit, 2D 20 unit, and 2D 40 unit networks (see Fig. A.3(b)).

As stated in the text, the power spectrum was calculated from the cell activity high-pass filtered above 15 Hz from 125 ms to 250 ms. Some power density was present above 100 Hz, but power density below 100 Hz dominated the contribution to P_{avg}.

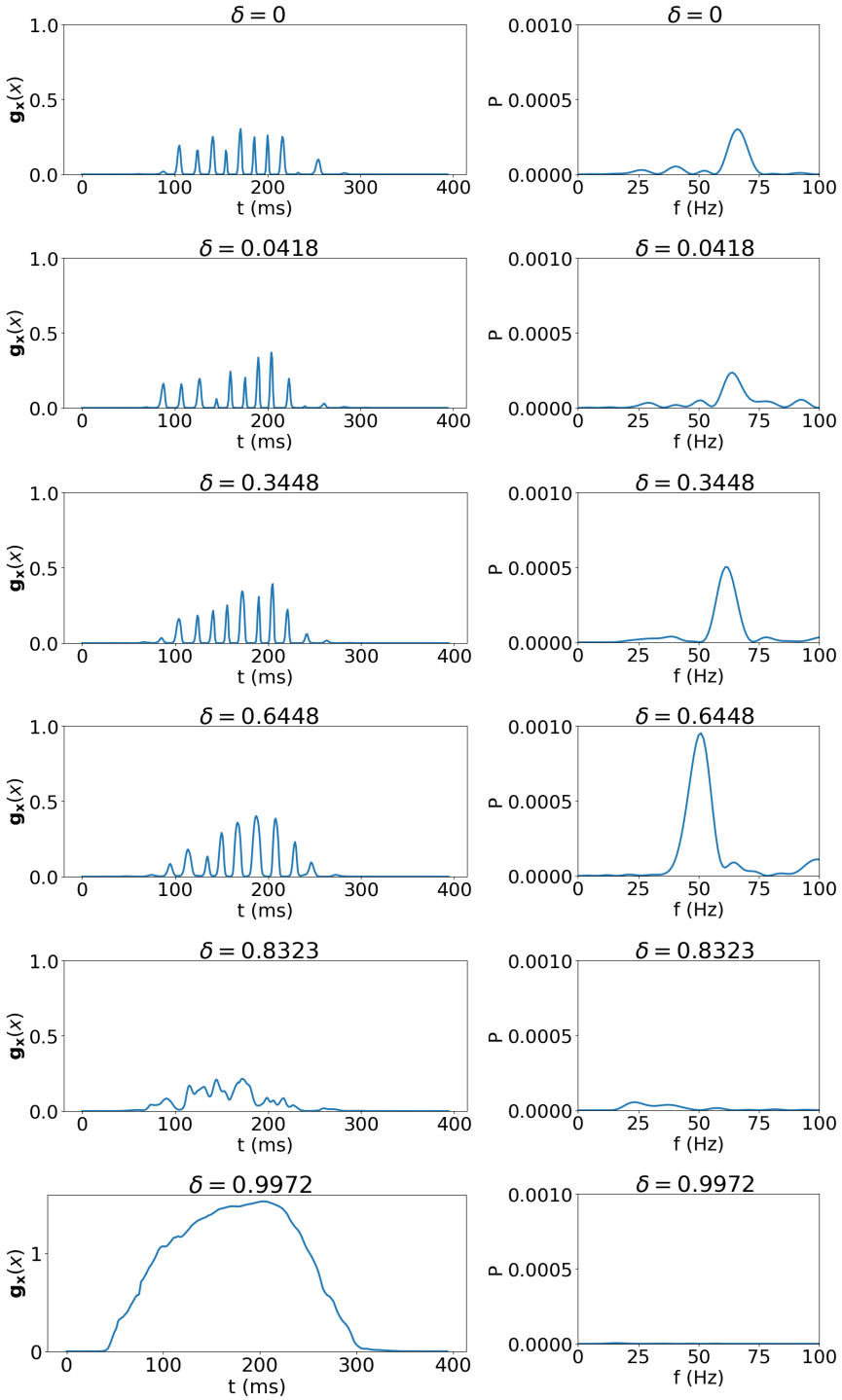

Figure A.8: Evolution of cell activity in seeded damage to W_0 in the 2D 100 unit network. Left: Cell activity. Right: Power spectra.

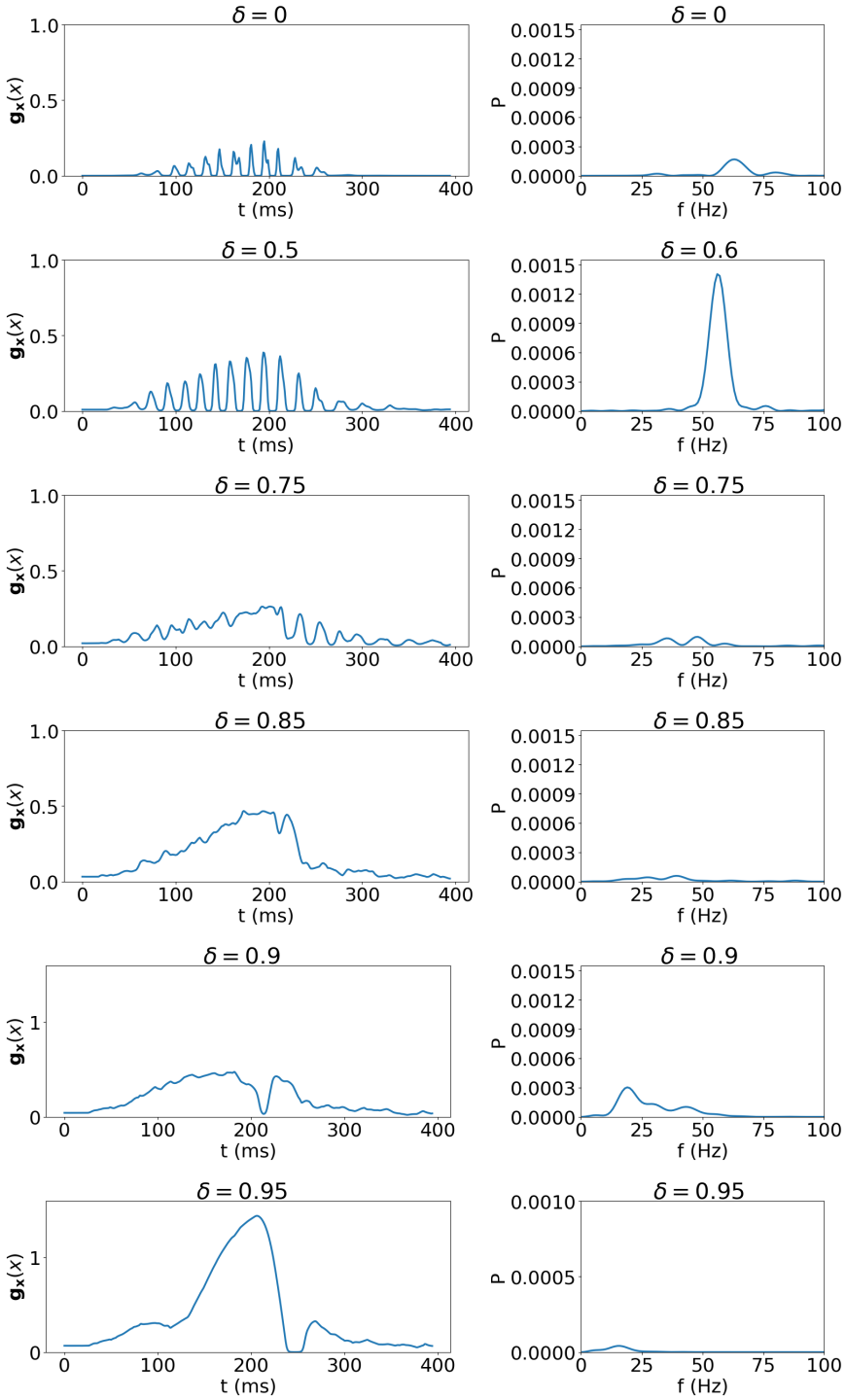

Figure A.9: Evolution of cell activity in flat damage to H_0 in the 2D 100 unit network. Left: Cell activity. Right: Power spectra.

Appendix B

Appendix To Chapter 3: Oscillatory Bands in Graded Inhibition Trials

B.1 Graded and Firing Inhibition

Graded and firing inhibition trials resulted in a dominant spectral peak in the 9-18 Hz range, with a second peak appearing in the 19-35 Hz range at higher tonic inhibition, higher MC GABA conductance, and lower input (Fig. 3.9). The frequency within these ranges depended mainly on the MC GABA conductance and MC input parameter μ_r (Fig. 3.9), and had little dependence on the tonic GC inhibition (Fig. B.1).

For trials with lower MC GABA conductance and higher input, a 2-8 Hz peak is often observed, likely from the "sniff" frequency of 6 Hz (eqn. 3.4). As MC GABA conductance increases and input decreases, it is usually absorbed into the 9-18 Hz peak (Fig. B.2).

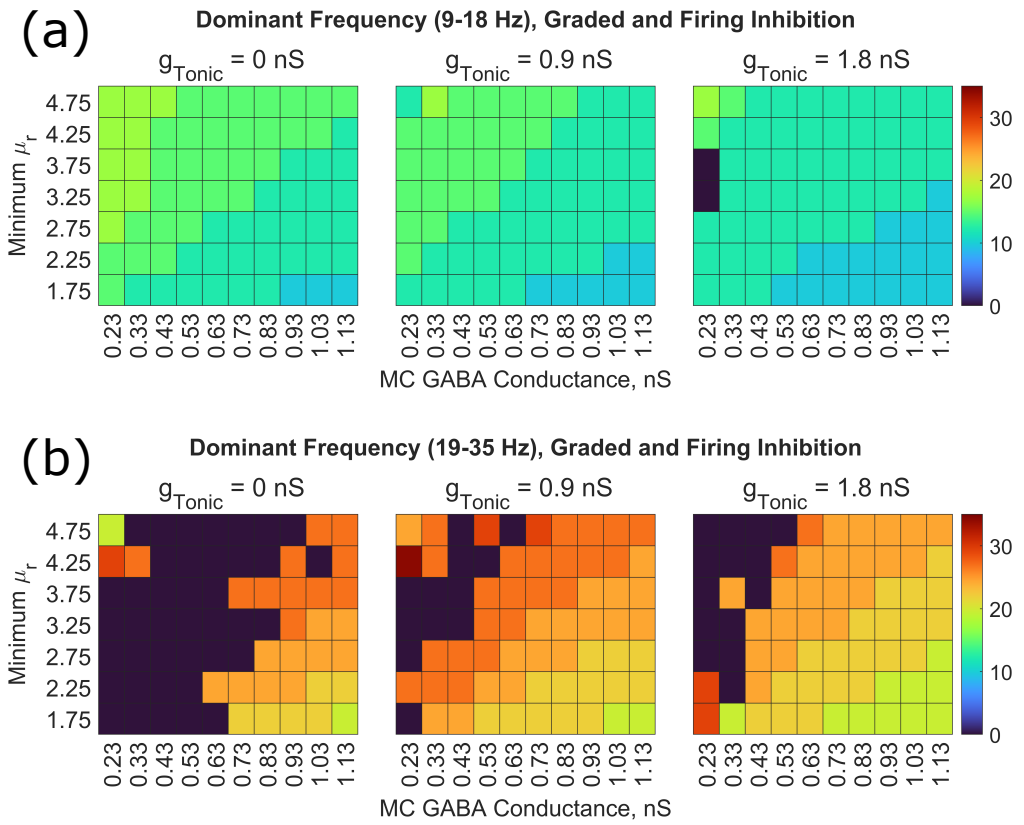

Figure B.1: **Oscillation Frequency for 9-18 Hz and 19-35 Hz Spectral Peaks with Graded and Firing Inhibition.** (a) Dominant frequency for the 9-18 Hz peak in the power spectrum. (b) Dominant frequency for the 19-35 Hz peak in the power spectrum. Black squares are parameter points where there was no significant peak in that frequency band.

B.2 Graded-Only Inhibition

With only graded MC inhibition, the most common dominant peak was between 2-8 Hz, usually around 5 Hz (Fig. B.3 (b)), which increased in power with increased MC GABA conductance and increased tonic GC inhibition (Fig. B.3 (a)).

Between 9-18 Hz, though there was a clear dominant peak for graded and firing inhibition, graded-only did not consistently have a peak in this range (Fig. B.4).

Graded-only inhibition did consistently have a peak between 19-35 Hz (Fig. B.5), though

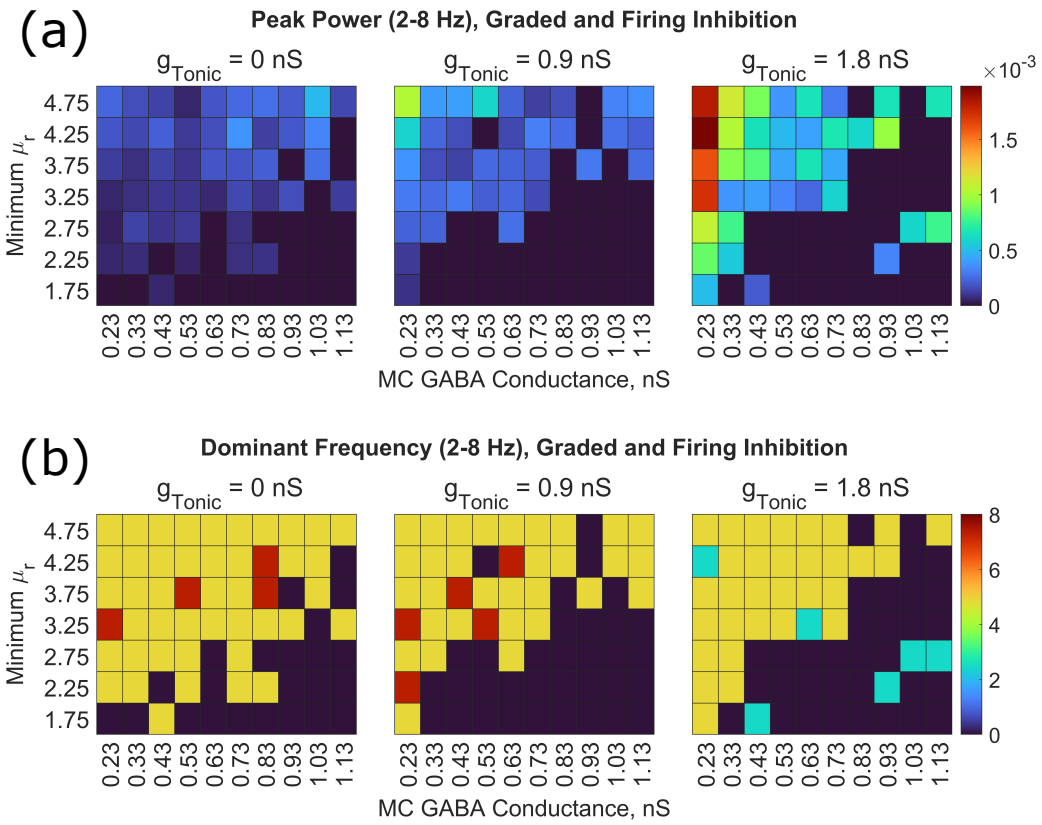

Figure B.2: **Oscillation Frequency and Power for 2-8 Hz Spectral Peak with Graded and Firing Inhibition.** (a) Peak power for the 2-8 Hz peak in the power spectrum (b) Dominant frequency for the 2-8 Hz peak in the power spectrum. Black squares are parameter points where there was no significant peak in the 2-8 Hz range.

a clear pattern is not easily discernible.

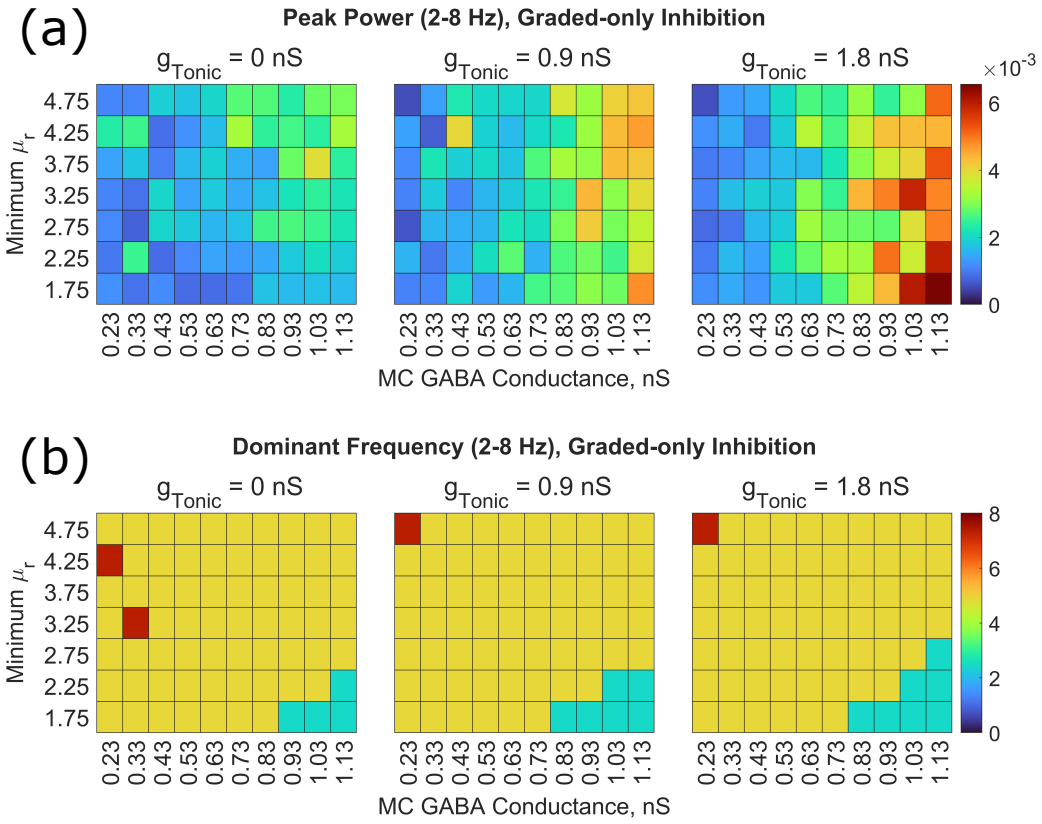

Figure B.3: **Oscillation Frequency and Power for 2-8 Hz Spectral Peak with Graded-Only Inhibition.** (a) Peak power for the 2-8 Hz peak in the power spectrum (b) Dominant frequency for the 2-8 Hz peak in the power spectrum.

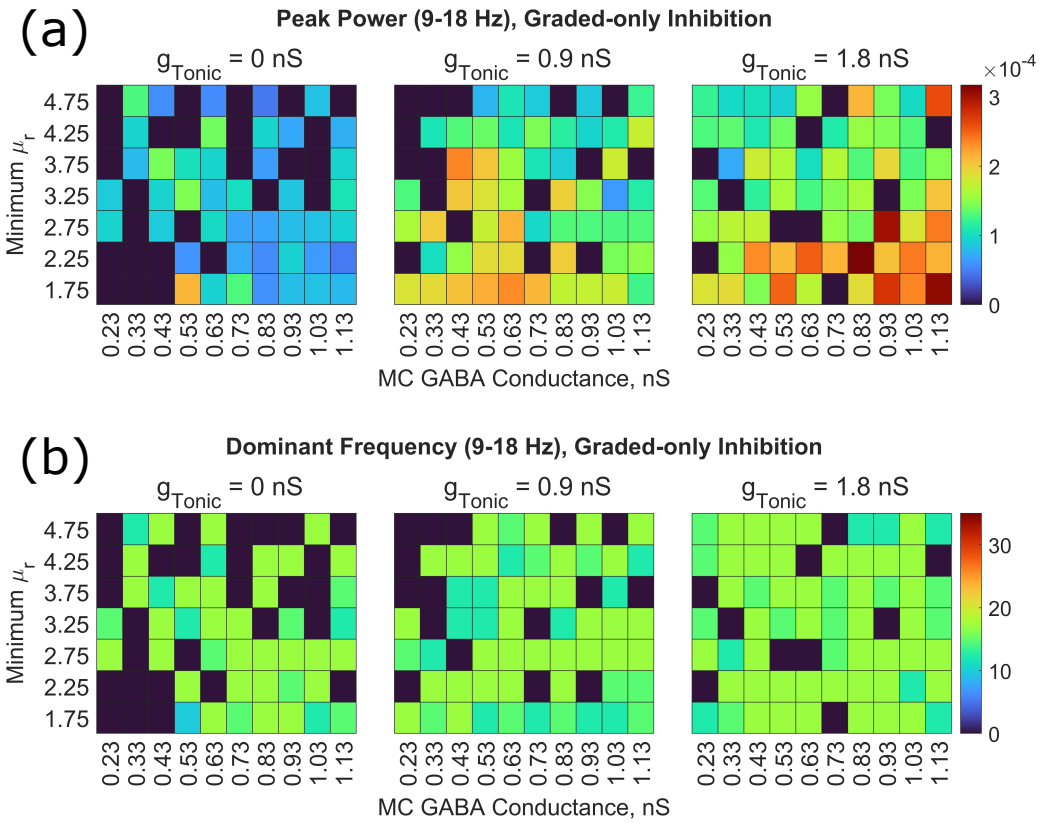

Figure B.4: **Oscillation Frequency and Power for 9-18 Hz Spectral Peak with Graded-Only Inhibition.** (a) Peak power for the 9-18 Hz peak in the power spectrum (b) Dominant frequency for the 9-18 Hz peak in the power spectrum. Black squares are parameter points where there was no significant peak in the 9-18 Hz range.

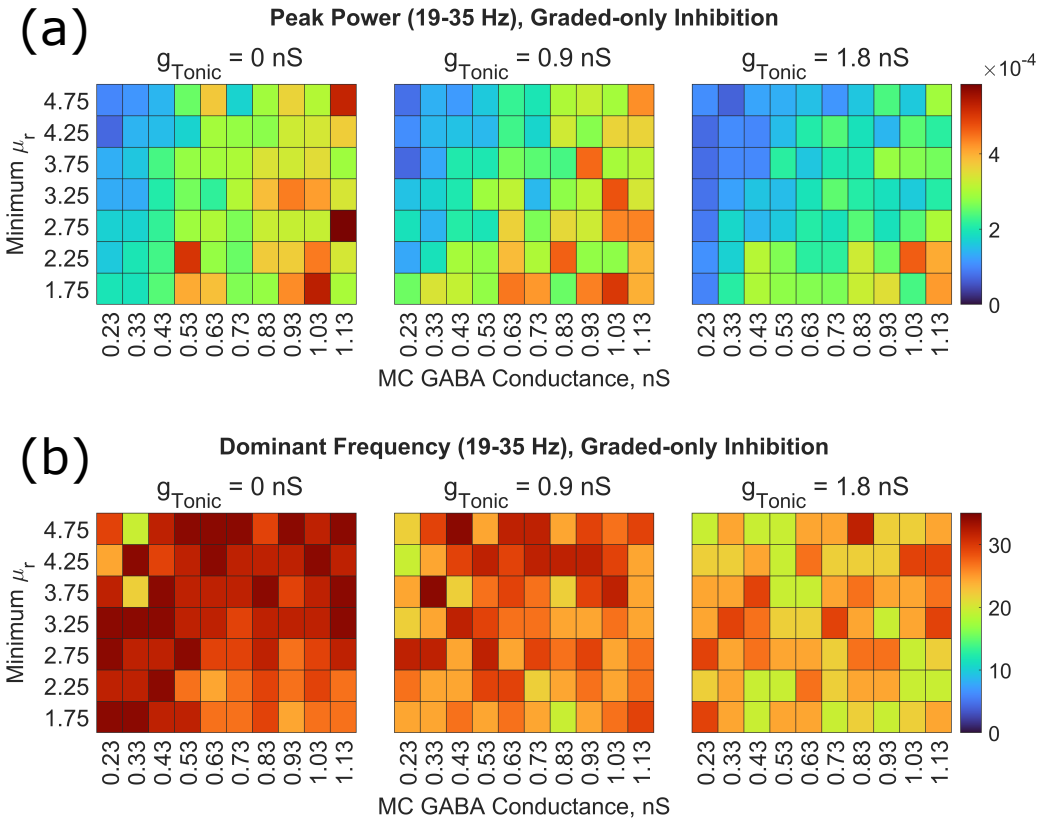

Figure B.5: **Oscillation Frequency and Power for 19-35 Hz Spectral Peak with Graded-Only Inhibition.** (a) Peak power for the 19-35 Hz peak in the power spectrum (b) Dominant frequency for the 19-35 Hz peak in the power spectrum.